Lehrstuhl für Nachrichtentechnik
Fakultät für Elektrotechnik und Informationstechnik
Technische Universität München

Applicability of Automotive Powerline Communication: A Theory- and Practice-based Study

Elisabeth Oberleithner

Vollständiger Abdruck der von der Fakultät für Elektrotechnik und Informationstechnik der Technischen Universität München zur Erlangung des akademischen Grades eines

Doktor–Ingenieurs

genehmigten Dissertation.

Vorsitzender:		Prof. Dr. Gerhard Rigoll
Prüfer der Dissertation:	1.	Prof. Dr.-Ing. Norbert Hanik
	2.	Prof. Dr.-Ing. Wolfgang Kellerer

Die Dissertation wurde am 01.04.2019 bei der Technischen Universität München eingereicht und durch die Fakultät für Elektrotechnik und Informationstechnik am 23.09.2019 angenommen.

Contents

Preface

This thesis was written during my time as a research assistance at the Institute for Communications Engineering, Line Transmission Technology Group at the Technical University of Munich.

In the first instance, I want to express my deepest gratitude to my supervisor Prof. Norbert Hanik for giving me the opportunity to dive into the thrilling world of electrical engineering and work towards a doctoral degree. I am deeply grateful for his ongoing support, guidance and believe throughout the years which were an enormous motivation day in, day out. I appreciate the wonderful and positive environment he provided and kept within the Wired Communications Group. I am also grateful to Prof. Wolfgang Kellerer for acting as co-supervisor.

I am very thankful to Dr. Helmut Kellermann from BMW Research and Technology for his constructive leadership of the FlexKab project and his commitment beyond the scope of the project. His productive feedback and ideas focused this work towards its success.

Many people have contributed to the success of this thesis. In particular, I am very grateful to Leonardo Coelho for his sustained support from the first steps of this work until the end, for giving me a profound knowledge basis and teaching me the finesse of simulation techniques. I thank Florian Breyer and Christian Morhart who taught me the first steps of VHDL programming. I also want to thank Yingkan Chen, Bernhard Geiger and Vladimir Sidorenko for the fruitful technical discussions and helpful comments. I am very grateful to Hannes Bartz, Roy Timo and Georg Zeitler for being close friends and making our skiing adventures possible. A special thanks goes to all my colleagues at the Institute for Communications Engineering for the great collaboration and enjoyable years we spent together. Many thanks also to my students Daniel Paulus, Arslan Faisal, Sadra Mostashar, Michael Hani and Tobit Klug for their passionate and collaborative work.

I am very grateful to Hans-Peter Huth, Joachim Sokol, Jochen Grimminger and Prof. Andreas Kirstädter for laying the foundation for my education in engineering. I owe my deep gratitude to Dominic Schupke for his steady support, advises and guidance

throughout many years.

Finally, I would like to thank my family and parents-in-law for their continuous support throughout the years. I owe my deepest gratitude to my grandmother Elisaveta, my parents Anelia and Johannes, and my brother Konstantin for their support, encouragement and being there for me when needed. Especially, the unconditioned love and support of my mom introduced new dimensions in my life and allowed me room for becoming who I am. My deep gratitude goes to my husband Tobias for his love, understanding, care and patience which helped me on the stony trail of this thesis. My special thanks goes to my dearly beloved son Gabriel for giving me a very special meaning of life and bringing sunshine to my heart — every day.

München, February 2019 Elisabeth Oberleithner

Zusammenfassung

Im-Fahrzeug Power Line Communication (PLC) ist eine viel versprechende Technologie, mit der die Datenübertragung ohne ein gesondertes, schweres und kostenspieliges Kommunikationsnetz ermöglicht wird. Somit kann das Gewicht und die Komplexität der Verkabelung im Fahrzeug reduziert werden. Diese Arbeit behandelt die Hauptaspekte, um die Anwendbarkeit und Leistungsfähigkeit eines inner-Fahrzeug PLC Transportnetzes unter Beweis zu stellen. Sie präsentiert und analysiert Messdaten, die im Testfahrzeug gesammelt wurden, zu dem Stromversorgungskanal und dem dazu gehörigen Rauschen. Basierend auf den Messdaten, werden Kanal und Rauschen charakterisiert und klassifiziert. Diese Arbeit schlägt Kanal- und Rauschmodelle vor, die später zur Überprüfung der Leistungsfähigkeit eines gesamten innter-Fahrzeug PLC Übertragungsystems eingesetzt werden. Modulationsverfahren und Codiertechniken mit niedriger Komplexität werden angewendet, um das Verbesserungspotenzial des Systems zu untersuchen. Die Arbeit wird mit der Vorstellung eines FPGA-basierten im-Fahrzeug PLC Demonstrators abgeschlossen. Es wird gezeigt, dass eine erfolgreiche PLC-Übertragung, auch bei dem Vorhandensein von impulsivem Rauschen, durchgeführt werden kann.

Abstract

Automotive Power Line Communication (PLC) is a promising technology that enables data transmission without the need of a dedicated, heavy and costly data communication network. This way, it allows for reducing the weight and wiring complexity of a vehicle. This thesis covers the main aspects of proving the applicability and performance of an in-vehicle PLC transport system. It presents and analyzes measurement results, performed on a test vehicle, on the car power line channel and the noise present on it. Based on the measurement data, a channel and noise characterization and classification is given. This work proposes automotive channel and noise models, which are later used for evaluating the performance of a complete in-vehicle PLC transmission system. Low complexity modulation formats and coding techniques are applied to investigate the improvement potential of the system. Finally, the thesis is completed by describing an FPGA-based in-car PLC transmission system demonstrator. It is shown, that a successful data transmission can be established with low complexity signal processing, even at the presence of impulsive noise.

1

Introduction

The fast development of communication technologies and always increasing data processing as well as generating application scenarios, shaped the evolution of the car over the past decades. Within only fifty years, the car transformed from a function-oriented transportation object to a high quality comfort offering, secure, driving supportive, entertaining life style item. All these additional features are realized by hardware and software, integrated into a huge in-vehicle communication network. The exchange of data within this network is performed by a communication system which consists of a transmitter, a channel and a receiver(s). Compared to other transport systems, the automotive one is characterized by its limited space and power resources, and high number of communication nodes with extremely different requirements. While some process critical data and rely on secure data transmission regardless of the data rate, other nodes fulfill tasks, enforcing high transmission speed and data volume with lower priority on data loss. To satisfy these diverse needs, the in-car communication system has evolved over decades into a high complexity, cost intensive system.

To meet the technical requirements of an in-vehicle transport system, different technologies have been developed. The in-car communication network is a heterogeneous network, consisting of multiple special-purpose subsystems different in underlying technology as well as application purposes. The single subsystems are optimized in their functional operation, cost and performance.

The automotive data transmission network is divided into different domains which include nodes with a similar functionality. Currently, there are five domains deployed: powertrain, body and comfort, chassis, safety and infotainment. One domain may in-

corporate several communication technologies. So called gateways enable data transmission throughout different technologies. The communication nodes in an in-vehicle network are called Electronic Control Units (ECUs). An ECU, depending on its technical and operational requirements, is connected to one communication technology. Some of the most popular in-vehicle data transmission technologies deployed nowadays are Local Interconnect Network (LIN), Controller Area Network (CAN), FlexRay, Ethernet and Media Oriented Systems Transport (MOST).

LIN is a low-cost serial network protocol with data rates below 20 Kbps (mostly 9.6 or 19.2 Kbps). It is mainly used in the body and comfort domain, where security non-critical data is processed, since it does not provide a reliable transmission. For a LIN bus, single-wire copper cables are used. A CAN-based bus can support data rates up to 1 and 2.5 Mbps with low-speed CAN (LS-CAN) and high-speed CAN (HS-CAN), respectively. The CAN transport protocol introduces message prioritization and the transmission is event triggered. It is mostly used in the body and comfort, powertrain and chassis domains. All nodes on a CAN bus are connected through double wire cooper cables. The next level of reliable communication is enabled by the FlexRay transport protocol. It is used for time critical applications with minimal delay requirement. It further implements a deterministic transmission control. Flexray uses two transport channels, each using a twisted pair copper cable, for redundancy. The maximum data rate per channel is 10 Mbps. The Flexray protocol can be deployed with a bus or star network topology or even a combination of both. MOST is a high-speed multimedia network technology which uses ring topology. It is mostly used to transport multimedia data, such as audio, video and voice, and uses plastic optical fiber (POF). The supported data rate is up to 25 Mbps. Another technology enabling high data rates and reliable data transmission is Ethernet. For the deployment in an automotive environment a new physical layer had to be defined to support transmission over unshielded twisted pair cables. The communication speed can reach up to 100 Mbps.

Besides the development of the automotive communication technology needs, the general increasing demand on Internet access and high data rate transmission trigger the emergence of new and cost effective technologies, and hence the development of Power Line Communication (PLC). Due to low implementation costs, easy deployment and clear structure, PLC is a promising solution for enabling data transmission without the need of deploying dedicated communication cabling infrastructure. Its distinct benefits make PLC to a popular and favored transmission technology in some areas, as e.g. in-building areas, the "last mile" to a residential area and industrial plants. Thus,

there has been many research done in this field. For example, the topic of modeling and characterization of an indoor PLC channel has been investigated in [1–4].

In recent years, the benefits of PLC make it also interesting to the automotive industry. The always increasing number of sensors, cameras and electronic devices require higher data rates and secure data transmission. Nowadays, car manufacturers fulfill these requirements by using coaxial or twisted pair cables and optical fibers. Due to high expenses for special equipment, additional weight and complex structure, optical fibers do not seem to be a good solution. Thus, automotive industry still sticks to the classical in-vehicle wiring architecture using coaxial and twisted pair cables for data transmission. The wiring harness as one of the most expensive components of a car weighs about 25-30 kg (depending on car's series and configuration) and has a total length of up to 4 km. As shown in [5], the number of electronic systems in vehicles grows dramatically. The increasing cabling complexity, weight and cost require rethinking of the in-vehicle wiring architecture and hence data transmission. Obviously, coaxial and twisted pair cables introduce compared to single wire, uninsulated power lines, additional weight, cost, volume and complexity. Here, PLC is a promising alternative solution for expanding or even replacing the existing wiring harness of a vehicle. Realizing data transmission over the car power line network and consequently omitting the heavy data communication lines would result in reduced weight and cost, and simplified cabling structure.

The maturing of the PLC technology and the benefits of reusing an existing wiring network are boosting the interest of both automobile industry and academics. In the past, research on different application fields of automotive PLC has been done as in [6–8]. Modeling and simulation of an automotive PLC channel was the scope of some works as e.g. [9–11]. Some of the efforts on measuring and characterizing the noise present on an automotive power line channel is captured by [12–15]. The performance of an in-vehicle PLC transmission system was subject to many research works as e.g. [16–18].

This thesis covers variety of aspects on the application of PLC as a transmission technology in an automotive communication system. It introduces a systematic composition and analysis of a car PLC network and gives an additional understanding of to what extent particular system components contribute to the specific automotive PLC channel characteristic. System parameters, such as varying distance of power lines to the carriage and wiring dimension, and their degree of impact on the channel behavior are investigated. Simulation results are compared with measurement data from a BMW 5 series. A generic model is applied, which can be easily adapted to any kind

of a vehicle and configuration. The presented consolidated analysis of an automotive PLC network allows for the study on the impact of specific network components on the transmission performance. In order to represent a realistic in-vehicle PLC system scenario, the noise present on the car power lines is extensively measured and analyzed. This work proposes a new in-car noise classification based on the obtained results. Following, some non-Gaussian noise models are presented and a new model is proposed, to better match the observed automotive power line noise characteristics. Based on the developed channel and noise models, the BER, as a system performance indicator, of a complete in-vehicle PLC communication system is evaluated. Different modulation formats, with focus on low cost and complexity, as well as coding techniques are applied to improve the results. This work is completed by the description of an FPGA-based implementation of an automotive PLC transmission system. To prove the concept and applicability of PLC in an in-vehicle environment, a basic demonstrator was developed and extensively tested. First, a laboratory environment emulating a car scenario was setup and used. Upon successful performance measurements, the demonstrator was deployed and tested in a car experimental setup. Performance measurements of the demonstrator are given and compared to theoretical results. A conclusion at the end, summarizes this thesis and discusses possible future topics on improving further the performance of an automotive PLC transmission system.

2

Channel Characterization

The maturing of the PLC technology and the benefits of reusing an existing wiring network are boosting the interest of both automobile industry and academics. In the past, research on different application fields of automotive PLC has been done as in [6–8]. Modeling and simulation of an automotive PLC channel was the scope of some recent works as e.g. [9–11]. This chapter summarizes the efforts of analyzing and modeling an automotive power line channel. This way, it gives a better understanding of the in-vehicle power line transmission characteristics. The discussed model allows for a systematic composition and analysis of the transmission channel. The first part of the chapter deals with the modeling of the automotive PLC transmission channel. It is shown that it is mainly characterized by the car battery, the number of branch (tap) lines and the loads introduced by the various electronic control units (ECUs). Following that, the results of some extensive measurements of the automotive PLC channel performed on a test vehicle are presented and discussed. It is observed, that particular transmission paths, such as the power line connecting the front and rear power distributions, FPD and RPD, feature a notably higher attenuation compared to other paths. Next, model results for selected car power line network components are compared to dedicated measurements and their impact on the overall system is analyzed. Finally, numerical results for the transmission loss over the frequency range of 0 - 600 MHz are presented for different wiring dimensions and load impedances. A brief conclusion of all results is given at the end of the chapter.

2.1. Modeling an Automotive PLC Channel

This section addresses the development of an in-vehicle PLC channel model. The presented model encompasses the essential characteristics of a PLC transmission line affecting the properties of the communication channel. It allows for a systematic composition and analysis of the car PLC transmission system and gives an additional understanding of to what extent particular system components contribute to the specific automotive PLC channel transmission characteristic. In this section first the model of a two-port circuit is presented as well as the computation of the chain and scattering parameters. Based on those, the calculation of the transfer function is summarized. Following, a characterization of some well known examples of a uniform transmission line is given. Based on these generic cases, a more sophisticated statistical model is derived, which takes the complicated structure of the car cabling system into account. System parameters, such as wiring dimensions, loading conditions, geometry and distance profile to the vehicle body, and their degree of impact on the channel behaviour are investigated. The outcome is a universal model, which can be easily adapted to any kind of a vehicle and configuration. The presented intensified analysis of an automotive PLC network allows for the study on the impact of specific network components on the transmission performance. Finally, in Section 2.3.3 the obtained theoretical results are compared with experimental measurement data from a BMW X5 (F15) to validate the simulation model. Part of the presented results were published in [19].

2.1.1. Power Line as a Two-Port Network

A two-port network model is used in circuit analysis techniques to isolate portions of larger circuits. This section covers the basics of the two-port network theory to model a power line transmission channel. More details on network theory and analysis can be found in [20].

A two-port is an electrical circuit with two pairs of terminals to connect an external circuit as depicted in Fig. 2.1. Each pair of terminals constitutes one port. It is common to call port 1 an input port and port 2 an output port. A two-port inside is regarded as a "black box" which connects the input and output ports by an arbitrary arrangement of components with its properties being specified by a matrix. This allows for an easier calculation of the response of the two-port to signals applied to its ports by isolating the complex inner network. This section focuses on passive, linear and time invariant two-port networks. These do not include an independent source, contain only linear components and satisfy the port condition. This signifies

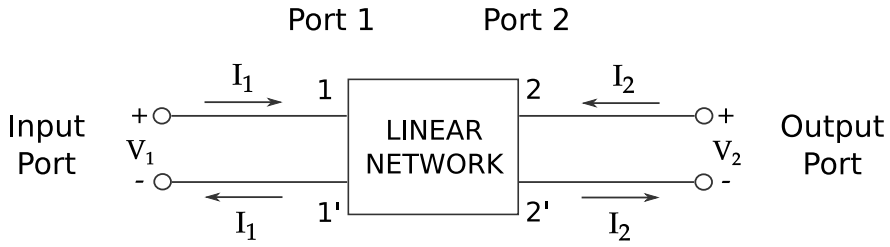

Figure 2.1.: A general two-port network

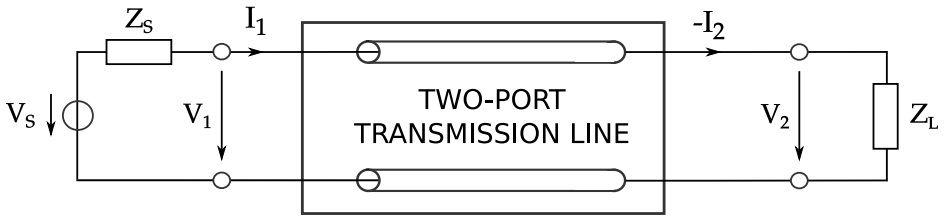

Figure 2.2.: Transmission line as a two-port network

that the current I_1 entering the two-port circuit at terminal 1 must equal the current emerging from terminal 1' (same port). The analog condition applies to the current at the terminals of the output port. The transmission properties of a time invariant two-port are independent of the time considered. Further, a passive linear two-port is reciprocal. That is, the voltage appearing at port 2 due to a current applied at port 1 is the same as the voltage appearing at port 1 when the same current is applied to port 2. Exchanging voltage and current results in an equivalent definition of reciprocity.

A single power line can generally be modeled as a two-port network as shown in Fig. 2.2 where the input port is connected to a generator with a source voltage V_S and an impedance Z_S while the output port is connected to a load impedance Z_L. The source and load voltages V_1 and V_2 are described as

$$V_1 = V_S - Z_S I_1 \tag{2.1}$$

$$V_2 = Z_L(-I_2) \tag{2.2}$$

with I_1 being the current entering at port 1 and I_2 the current appearing at port 2. The input impedance

$$Z_{in} = \frac{V_1}{I_1} \tag{2.3}$$

denotes the impedance between the terminals of port 1.

The input voltage V_1 and the output voltage V_2 are linear functions of the input

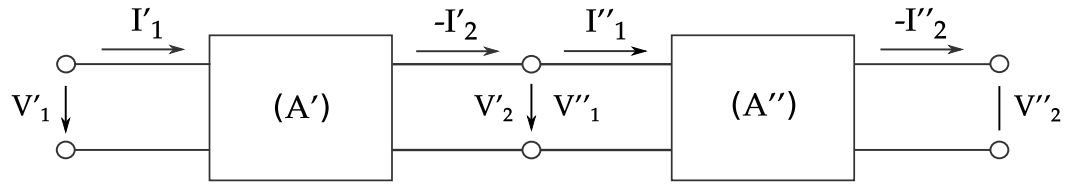

Figure 2.3.: A cascade of two-ports

current I_1 and the output current I_2. The chain matrix $\boldsymbol{A}$ (also called ABCD matrix) describes the dependency of V_1 and I_1 from V_2 and I_2 as

$$\begin{pmatrix} V_1 \\ I_1 \end{pmatrix} = \boldsymbol{A} \begin{pmatrix} V_2 \\ -I_2 \end{pmatrix} \tag{2.4}$$

with

$$\boldsymbol{A} = \begin{pmatrix} a_{11} & a_{12} \\ a_{21} & a_{22} \end{pmatrix} = \begin{pmatrix} A & B \\ C & D \end{pmatrix} \tag{2.5}$$

and

$$det(\boldsymbol{A}) = 1 \tag{2.6}$$

which holds at any frequency due to the reciprocity property of a two-port. Consequently we obtain the chain equations

$$\begin{aligned} V_1 &= AV_2 + B(-I_2) \\ I_1 &= CV_2 + D(-I_2). \end{aligned} \tag{2.7}$$

A cascade of two-port circuits as shown in Fig. 2.3 is of special interest when it comes to modeling transmission lines as discussed in Sec. 2.1.3. Here, the output ports of a two-port are connected to the input ports of the next one [20]. Using Eq. 2.4, the chain matrices of both circuits are

$$\begin{pmatrix} V_1' \\ I_1' \end{pmatrix} = \boldsymbol{A'} \begin{pmatrix} V_2' \\ -I_2' \end{pmatrix}, \begin{pmatrix} V_1'' \\ I_1'' \end{pmatrix} = \boldsymbol{A''} \begin{pmatrix} V_2'' \\ -I_2'' \end{pmatrix}$$

and because $V_2' = V_1''$ and $-I_2' = I_1''$

$$\begin{pmatrix} V_1' \\ I_1' \end{pmatrix} = \boldsymbol{A'A''} \begin{pmatrix} V_2'' \\ -I_2'' \end{pmatrix}.$$

This way, it is easy to show that the chain matrix of a cascade of two-ports is the

matrix multiplication of the chain matrices of the individual two-port networks

$$\boldsymbol{A} = \boldsymbol{A_1 A_2 A_3} \dots \tag{2.8}$$

Now, again considering the basic circuit of Fig. 2.2, by substituting Eq. 2.2, dissolved for I_2, and Eq. 2.7 in Eq. 2.1 and Eq. 2.3, following relations are obtained

$$\begin{aligned} Z_{in} = \frac{V_1}{I_1} &= \frac{AV_2 + B(-I_2)}{CV_2 + D(-I_2)} \\ &= \frac{AV_2 + BV_2 Z_L^{-1}}{CV_2 + DV_2 Z_L^{-1}} \\ &= \frac{A + BZ_L^{-1}}{C + DZ_L^{-1}} \end{aligned} \tag{2.9}$$

and

$$\begin{aligned} V_S = V_1 + Z_S I_1 &= AV_2 + B(-I_2) + Z_S(CV_2 + D(-I_2)) \\ &= AV_2 + BV_2 Z_L^{-1} + Z_S(CV_2 + DV_2 Z_L^{-1}) \\ &= V_2(A + BZ_L^{-1} + CZ_S + DZ_S Z_L^{-1}). \end{aligned} \tag{2.10}$$

Given above derivations, the transfer function can be expressed as the ratio of the output voltage V_2 to the source voltage V_S and determined using the chain parameters

$$\begin{aligned} H(f) = \frac{V_2}{V_S} &= \frac{1}{A + BZ_L^{-1} + CZ_S + DZ_S Z_L^{-1}} \\ &= \frac{Z_L}{AZ_L + B + CZ_L Z_S + DZ_S}. \end{aligned} \tag{2.11}$$

From substituting Eq. 2.3 in Eq. 2.1 follows that

$$V_S = V_1 + Z_S I_1 = Z_{in} I_1 + Z_S I_1 \quad = I_1(Z_{in} + Z_S).$$

By rewriting Eq. 2.3 for V_1, one obtains

$$V_1 = Z_{in} I_1 \quad = Z_{in} I_1 \frac{Z_{in} + Z_S}{Z_{in} + Z_S} = \frac{Z_{in} V_S}{Z_{in} + Z_S}$$

and for I_1

$$I_1 = \frac{V_1}{Z_{in}} \quad = \frac{Z_{in} V_S}{(Z_{in} + Z_S) Z_{in}} = \frac{V_S}{Z_{in} + Z_S}.$$

The actual power transfered into a power line is obtained by substituting above defi-

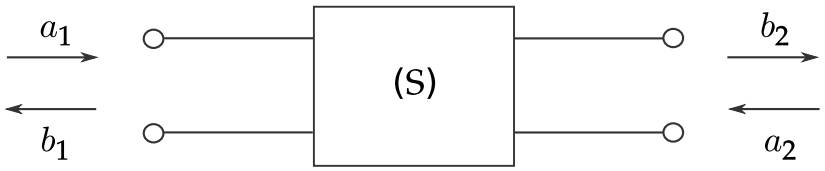

Figure 2.4.: A two-port with waves at the in- and output ports

nitions as follows

$$\begin{aligned} P_{in} = \mathrm{Re}\left\{V_1 I_1^*\right\} &= \mathrm{Re}\left\{I_1 Z_{in} \frac{Z_{in}+Z_S}{Z_{in}+Z_S} \frac{V_S^*}{Z_{in}^*+Z_S^*}\right\} \\ &= \frac{|V_S|^2}{|Z_{in}+Z_S|^2} \mathrm{Re}\left\{Z_{in}\right\}. \end{aligned} \tag{2.12}$$

In practice the chain matrix approach is often replaced by an approach based upon scattering parameters (S-parameters). Unlike the chain parameters, which are defined in terms of voltage and current at the two-port's terminals, the scattering parameters are defined in terms of incident and reflected waves at the terminals instead and consequently power variables are used. On the other hand, incident and reflected power are easy to measure using directional couplers [20]. The measurements can be performed by terminating a two-port with real impedances.

The S-parameters describe the relation between two new variables a and b representing the incident and reflected waves at the ports, respectively. The variables are regarded as normalized complex voltage waves, normalized with an arbitrary reference impedance Z_0, which is assumed to be real and positive [21]

$$\begin{aligned} a_k &= \frac{V_{h_k}}{\sqrt{Z_0}} = I_{h_k}\sqrt{Z_0} \\ b_k &= \frac{V_{r_k}}{\sqrt{Z_0}} = -I_{r_k}\sqrt{Z_0}, \text{ for } k = 1,2 \end{aligned} \tag{2.13}$$

with a_k being the incident and b_k the reflected waves at port k as illustrated in Fig. 2.4. V_{h_k}, I_{h_k} are the voltage and current of the incident wave at port k while V_{r_k}, $-I_{r_k}$ are the voltage and current of the reflected wave at port k. In practice, it is convenient to assume that the reference impedance Z_0 is real and positive, and identical for all

frequencies and ports. Following the transmission line theory it applies

$$\begin{aligned} V_{h_k} &= \frac{1}{2}\left(V_k + Z_{in} I_k\right) \\ V_{r_k} &= \frac{1}{2}\left(V_k - Z_{in} I_k\right) \end{aligned} \tag{2.14}$$

From Eq. 2.13 and Eq. 2.14 follows

$$\begin{aligned} a_k &= \frac{1}{2}\left(\frac{V_k}{\sqrt{Z_0}} + I_k\sqrt{Z_0}\right) \\ b_k &= \frac{1}{2}\left(\frac{V_k}{\sqrt{Z_0}} - I_k\sqrt{Z_0}\right). \end{aligned} \tag{2.15}$$

The reflected waves depend on the incident waves, i.e. both the reflected wave b_1 and b_2 are reliant on the incident waves a_1 and a_2. In the case of a linear two-port network this relationship is also linear and described by the scattering equations

$$\begin{aligned} b_1 &= s_{11}a_1 + s_{12}a_2 \\ b_2 &= s_{21}a_1 + s_{22}a_2 \end{aligned} \tag{2.16}$$

The parameters s_{ij} are the scattering parameters of a two-port. By introducing the scattering matrix (S-matrix)

$$\boldsymbol{S} = \begin{pmatrix} s_{11} & s_{12} \\ s_{21} & s_{22} \end{pmatrix}$$

the scattering equations describing a two-port obtain the form

$$\begin{aligned} \begin{pmatrix} b_1 \\ b_2 \end{pmatrix} &= \boldsymbol{S} \begin{pmatrix} a_1 \\ a_2 \end{pmatrix} \\ &= \begin{pmatrix} s_{11} & s_{12} \\ s_{21} & s_{22} \end{pmatrix} \begin{pmatrix} a_1 \\ a_2 \end{pmatrix}. \end{aligned} \tag{2.17}$$

Thus, the S-matrix is referenced to a single positive real impedance, Z_0 (often 50 Ω). Due to the reciprocity of a linear two-port

$$s_{12} = s_{21} \tag{2.18}$$

holds for any symmetric transmission line. In other words, a power line channel is symmetric and provides the same transmission quality in both directions.

The chain parameters can be obtained from the S-parameters by means of the following relations [[21], [22]]

$$A = \frac{(1+s_{11})(1-s_{22})+s_{12}s_{21}}{2s_{21}} \tag{2.19}$$

$$B = Z_0\frac{(1+s_{11})(1+s_{22})-s_{12}s_{21}}{2s_{21}} \tag{2.20}$$

$$C = \frac{(1-s_{11})(1-s_{22})-s_{12}s_{21}}{2Z_0 s_{21}} \tag{2.21}$$

$$D = \frac{(1-s_{11})(1+s_{22})+s_{12}s_{21}}{2s_{21}}. \tag{2.22}$$

The conversion from the chain parameters to the S-parameters takes the format

$$s_{11} = \frac{A+BZ_0^{-1}-CZ_0-D}{A+BZ_0^{-1}+CZ_0+D} \tag{2.23}$$

$$s_{12} = \frac{2(AD-BC)}{A+BZ_0^{-1}+CZ_0+D} \tag{2.24}$$

$$s_{21} = \frac{2}{A+BZ_0^{-1}+CZ_0+D} \tag{2.25}$$

$$s_{22} = \frac{-A+BZ_0^{-1}-CZ_0+D}{A+BZ_0^{-1}+CZ_0+D} \tag{2.26}$$

From Eq. 2.6

$$AD-BC = 1 \tag{2.27}$$

holds and hence $s_{12} = s_{21}$. For the case that the source and load impedances are equal to the reference impedance, i.e. $Z_S = Z_L = Z_0$, and given Eq. 2.11 and 2.25, the transfer function can be obtained from the s_{21} S-parameter as

$$H(f)|_{Z_S=Z_L=Z_0} = \frac{s_{21}}{2}. \tag{2.28}$$

Considering the relations from Eq. 2.11 and 2.28, the channel transfer function of a single power line can be completely characterized by the chain parameters and the terminating impedances. Thus, the modeling efforts are focused to the characterization of the chain matrix of the given transmission line. This will be discussed in the following sections for different setups and configurations.

2.1.2. Characterization of a Uniform Power Line

To analyze the effects that in-vehicle power lines have on the transmission properties of a PLC system, the electrical characteristics of the line must be evaluated. The basic electrical characteristics that define a transmission line are its characteristic impedance and its propagation constant. To specify and derive these terms, the fundamental properties of a transmission line are examined in this section.

A transmission line stores electric and magnetic energy distributed in space and alternating between the two fields in time. That is, at any position along the line the energy is stored in a combination of electric and magnetic forms and converted from one form to the other as time progresses. If it's assumed that there are no components of the electric or magnetic fields pointing to the length direction of the line, the electric and magnetic fields will be orthogonal. This is known as transverse electromagnetic mode (TEM). A segment of a lossy uniform (with regular cross section) transmission line, which mainly has a TEM or quasi-TEM mode of propagation [21], can be represented by a circuit model that combines inductors, L, capacitors, C, and resistors, R and $1/G$s, whose values are dependent on the geometry of the line and the properties of the materials comprising the line. The equivalent lumped-element circuit model is shown in Fig. 2.5. The series resistors, R, represent the losses due to the finite conductivity of the conductor. The shunt conductance, G, represent the losses due to the finite resistance of the dielectric separating the conductor and the ground plane. The inductors, L, represent the magnetic field and the capacitors, C, – the electric field between the conductor and the ground plane. The R', L', G' and C' constants are all specified per unit length. Herewith R' is the resistance in ohms per meter (Ω/m), L' is the inductance in henries per meter (H/m), G' is the conductance in siemens per meter (S/m) and C' is the capacitance in farads per meter (F/m). The values of R', L', G', and C' are affected by the geometry of the transmission line and by the electrical properties of the dielectrics and conductors. There are two cases of a single transmission line of interest: a single wire line and a double wire line as depicted in Fig. 2.6a and 2.6b, respectively. In the first case, the potential difference is given between a conducting wire and a ground plane [23].

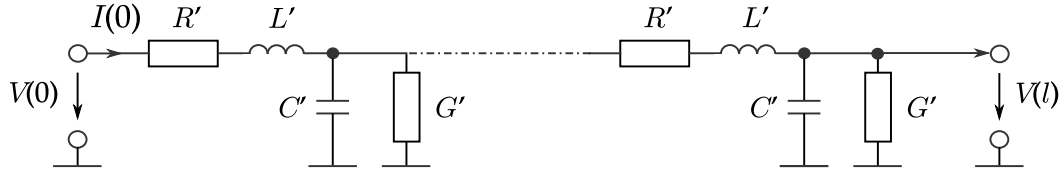

Figure 2.5.: Lumped-element circuit model of a transmission line

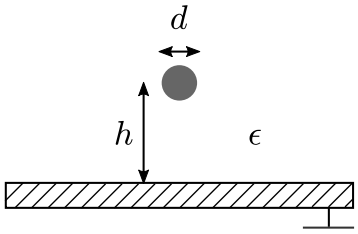

(a) Crosssection of a single wire line

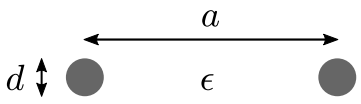

(b) Crosssection of a double wire line

Figure 2.6.: Crosssection of transmission lines

Single wire lines are used as power lines in vehicles and are hence, the transmission lines in automotive PLC systems. The per-unit line parameters are in this case given by

$$R' = \frac{2}{\pi d}\sqrt{\frac{\pi f \mu}{\sigma}} \tag{2.29}$$

$$L' = \frac{\varepsilon\mu}{C'} \tag{2.30}$$

$$G' \approx 0 \tag{2.31}$$

$$C' = \frac{2\pi\varepsilon}{\cosh^{-1}\left(\frac{2h}{d}\right)}, \tag{2.32}$$

where h is the distance of the wire to the ground plane, d is the conductor's diameter, σ is its specific conductance [S/m], ε and μ are the permittivity [F/m] and permeability [H/m] of the surrounding material, respectively. In contrast, a double wire consists of two parallel electrical wires, which are differentially excited. The differential mode of operation provides a more robust transmission against noise. Therefore, double wire cables are commonly used for in-vehicle data transmission. The per-unit parameters

of an unshielded double wire line are given by

$$R' = \frac{4}{\pi d}\sqrt{\frac{\pi f \mu}{\sigma}} \tag{2.33}$$

$$L' = \frac{\varepsilon \mu}{C} \tag{2.34}$$

$$G' \approx 0 \tag{2.35}$$

$$C' = \frac{\pi \varepsilon}{\cosh^{-1}\left(\frac{a}{d}\right)}, \tag{2.36}$$

where a is the distance between both conductors. By the use of above parameters the characteristic impedance for both types of cables takes the form

$$Z_c = \sqrt{\frac{R' + j\omega L'}{G' + j\omega C'}} \tag{2.37}$$

and the propagation constant results in

$$\gamma = \sqrt{(R' + j\omega L')(G' + j\omega C')} = \alpha + j\beta, \tag{2.38}$$

where $\omega = 2\pi f$ is the radian frequency and f is the frequency in hertz, α is called the attenuation coefficient and has units of Nepers per meter, and β is called the phase constant with units of radians per meter (expressed as rad/m). Using above two parameters, the chain matrix from Eq. 2.5 can be calculated for a uniform transmission line with length l as

$$\boldsymbol{A} = \begin{pmatrix} \cosh \gamma l & Z_c \sinh \gamma l \\ \frac{1}{Z_c} \sinh \gamma l & \cosh \gamma l \end{pmatrix}. \tag{2.39}$$

Additionally, a transmission line with length l, propagation constant γ and its characteristic impedance equal to the reference impedance, i.e. $Z_c = Z_0$, has a scattering matrix

$$\boldsymbol{S} = \begin{pmatrix} 0 & e^{-\gamma l} \\ e^{-\gamma l} & 0 \end{pmatrix}. \tag{2.40}$$

However, the characteristic impedance, Z_c, is in general different from the system reference impedance, Z_0. Following formula can be applied to convert the S-parameters referred to a reference impedance Z_0 to another reference impedance Z_0'

$$\boldsymbol{S'} = \frac{\boldsymbol{S} - \Gamma \boldsymbol{1}}{\boldsymbol{1} - \Gamma \boldsymbol{S}} \tag{2.41}$$

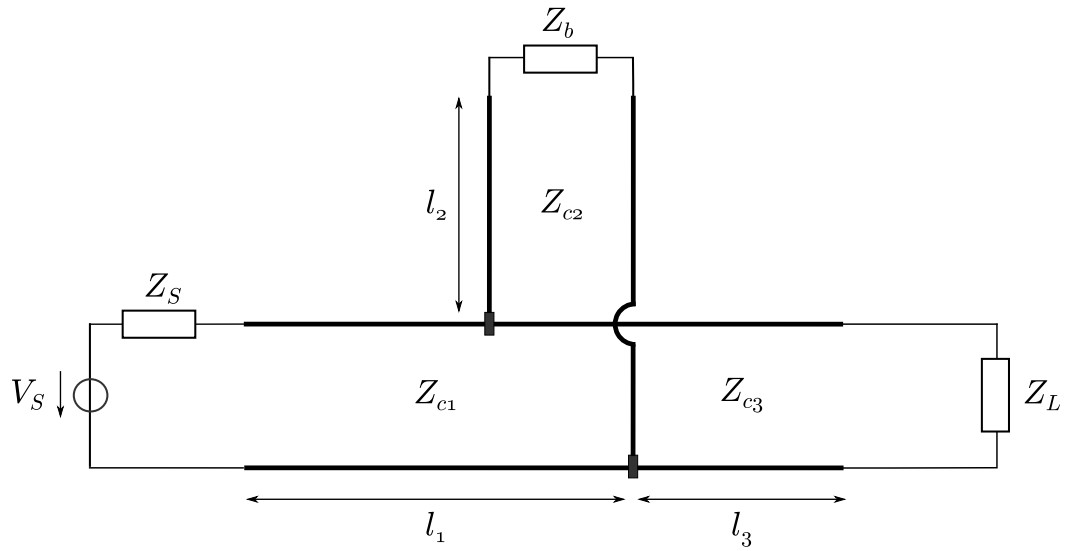

Figure 2.7.: Transmission line with one bridge tap

with

$$\Gamma = \frac{Z_0' - Z_0}{Z_0' + Z_0}.$$

2.1.3. Power Line with a Tap Line

In the context of an automotive PLC system, a transmission line is part of a car's power line network connecting a transmitter and a receiver node. When calculating the chain matrix for a PLC transmission line, a bridge tap line is distinguished from a main transmission line. While main transmission lines are considered to be on the shortest path between transmitter and receiver, tap lines are all lines that are coupled with the main transmission line at some point between the communication nodes. Tap lines can in turn branch out into further tap lines. In that sense, an automotive PLC transmission line comprises at least one main line and n ($n \in \mathbb{N}$) tap lines. This section describes a general modeling of an automotive PLC transmission line based on the two-port network and transmission line theory.

A simplified transmission line structure, as illustrated in Fig. 2.7, is first discussed to give a basic understanding of the new modeling approach. The setting represents a main transmission line, consisting of two lines with lengths l_1 and l_3, with one bridge tap terminated with an impedance Z_b. Z_{c1}, Z_{c2}, and Z_{c3} in Fig. 2.7 correspond to the characteristic impedance of the single transmission lines. For simplification of the calculations, it is assumed that $Z_{c1} = Z_{c2} = Z_{c3} = Z_c$. By replacing the bridge tap with its equivalent impedance Z_{eq}, the circuit from Fig. 2.7 can be depicted as in

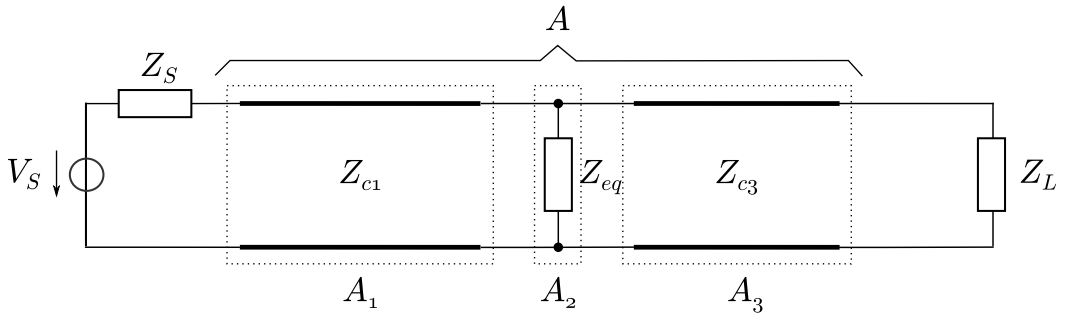

Figure 2.8.: Equivalent circuit to Fig. 2.7

Fig. 2.8. Based on the setting of the equivalent circuit, the transmission line can be analyzed element by element. Beginning with the source impedance Z_s, it represents a lengthwise impedance and the chain matrix describing it has the form [20]

$$\boldsymbol{A_0} = \begin{pmatrix} 1 & Z_s \\ 0 & 1 \end{pmatrix}. \tag{2.42}$$

The transmission line with length l_1 represents a main transmission line and its chain matrix can be computed by Eq. 2.39 giving

$$\boldsymbol{A_1} = \begin{pmatrix} \cosh(\gamma l_1) & Z_c \sinh(\gamma l_1) \\ \frac{1}{Z_c}\sinh(\gamma l_1) & \cosh(\gamma l_1) \end{pmatrix}.$$

Following, the equivalent impedance describing the bridge tap represents a transverse impedance along the line with a chain matrix

$$\boldsymbol{A_2} = \begin{pmatrix} 1 & 0 \\ \frac{1}{Z_{eq}} & 1 \end{pmatrix} \tag{2.43}$$

with

$$Z_{eq} = Z_c \left(\frac{Z_b + Z_c \tanh(\gamma l_2)}{Z_c + Z_b \tanh(\gamma l_2)} \right). \tag{2.44}$$

The transmission line with length l_3 again represents a main transmission line and Eq. 2.39 can be applied to obtain $\boldsymbol{A_3}$. Now that the chain matrices of all sub-circuits of the transmission line are given, the total chain matrix is provided by subsequently cascading the matrices $\boldsymbol{A_0}$, $\boldsymbol{A_1}$, $\boldsymbol{A_2}$ and $\boldsymbol{A_3}$ to produce the channel frequency response.

This results in a total chain matrix $\boldsymbol{A}_{total}$ representing the whole line

$$\boldsymbol{A}_{total} = \begin{pmatrix} A & B \\ C & D \end{pmatrix} = \prod_{i=0}^{3} \boldsymbol{A}_i. \tag{2.45}$$

Having $\boldsymbol{A}_{total}$, the transfer function $H(f)$ can be obtained by Eq. 2.11

$$H(f) = \frac{Z_L}{AZ_L + B + CZ_LZ_S + DZ_S}$$

where Z_L and Z_S are the load and source impedance, respectively.

The generalization to a transmission line with more than one bridge tap is straightforward by applying the chain rule.

2.1.4. Statistical Modeling of a Non-uniform Transmission Line

Considering an in-building PLC line, which is mostly installed in cable pipes within the walls, it has a reproducible and traceable placement. On the contrary, the automotive wiring is only loosely mounted to the car body and is constantly exposed to movements, e.g. when opening a door or the luggage trunk. Since the car body is used as a ground point, the distance between a power line (PL) and the vehicle body, parameter h in Fig. 2.6a, is a factor that affects the transmission properties of the channel. For investigating the impact of varying distance between a PL and the car body (ground plane), the modeled PL is being partitioned into small sections (e.g. 10 cm) and each section is applied a random distance to the car body. For the computation of the scattering and chain parameters, the small sections are treated as short uniform transmission lines which cascaded form the initial non-uniform line. The height of an automotive PL with respect to the ground plane can be considered as a random variable according to a certain distribution. Since height is non-negative, it cannot be modeled by the Gaussian distribution. However, a transformation method, called the normal score transformation, presented by [24] can be used which utilizes a generalized translation transformation from a Gaussian, Y, to a non-Gaussian, X, through

$$X = F^{-1}(\Phi(Y)) \tag{2.46}$$

with

$$\begin{aligned}\Phi(y) &= \frac{1}{2\pi}\int_{-\infty}^{y} e^{\frac{-t^2}{2}}dt \\ &= \frac{1}{2}\text{erfc}\left(\frac{-y}{\sqrt{2}}\right),\end{aligned} \tag{2.47}$$

where Φ and F are the cumulative distribution functions of the standard normal and target non-Gaussian processes, respectively. This way, starting with an ergodic Gaussian process Y can be transformed to the desired target cumulative distribution function (cdf) $F(U)$ of the cable height to the ground plane. The target cdf depends on the key features of the parameter height. Considering the height as a random variable U, the outcomes are non-negative real numbers where certain outcomes occur with a constant probability per unit (cable) length. Furthermore, the single outcomes occur in a memoryless manner, i.e. the probability of a certain height is not influenced by the history of the random process. Given above properties, the exponential distribution is a good match for the target cdf and is defined as

$$F(U) = \begin{cases} 0 & u < 0, \\ 1 - e^{-\lambda u} & u \geq 0 \end{cases} \tag{2.48}$$

with rate $\lambda > 0$ and $\mathbf{E}[U] = \frac{1}{\lambda}$. From data obtained from a test vehicle described in Chapter 6, it is known that due to the cable lay mechanism there is a minimum distance h_{min} present between the power lines and the car body. This additional condition can be implied by a shifted exponential distribution through

$$F(U) = \begin{cases} 0 & u < h_{min}, \\ 1 - e^{-\lambda(u-h_{min})} & u \geq h_{min}. \end{cases} \tag{2.49}$$

Hence, the target cdf can be described by the cdf of an exponential distribution that is shifted h_{min} units with $h_{min} > 0$ and $u \geq h_{min}$. To apply the normal score transformation, first the inverse function $F^{-1}(U)$ is solved

$$\begin{aligned} z &= 1 - e^{-\lambda(u-h_{min})} \\ e^{-\lambda(u-h_{min})} &= 1 - z \\ -\lambda(u - h_{min}) &= \ln(1 - z) \\ u &= h_{min} - \frac{1}{\lambda}\ln(1 - z). \end{aligned} \tag{2.50}$$

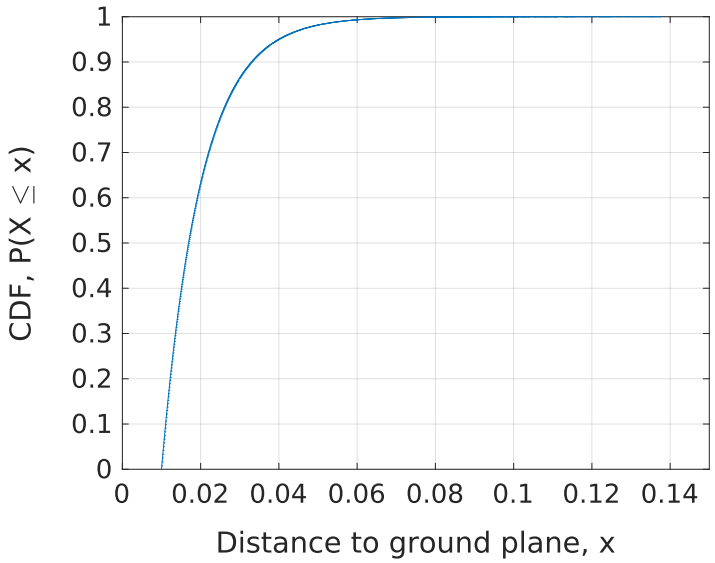

Figure 2.9.: Cumulative distribution function of the cable height to the car body

By applying Eq. 2.46 the transformation from the Gaussian process to the random geometry is obtained by

$$\begin{aligned} X &= h_{min} - \frac{1}{\lambda} \ln\left(1 - \Phi(Y)\right) \\ &= h_{min} - \frac{1}{\lambda} \ln\left(1 - \frac{\operatorname{erfc}(\frac{-y}{\sqrt{2}})}{2}\right). \end{aligned} \tag{2.51}$$

and the corresponding cdf is depicted in Fig. 2.9 for $h_{min} = 1$ cm and $\lambda = 1$ cm^{-1}.

The random cable distance to the vehicle body generated this way is applied to cable sections of 10 cm length. As Fig. 2.10a shows, the resulting cable geometry is stepped and does not match the smoothness of real lines. To obtain a more realistic representation, the output X is passed through a smoothing filter. Fig. 2.10b shows an example of a non-uniform transmission line of length 5 m with randomly generated cable height to ground plane, $h_{min} = 1$ cm and $\lambda = 1$ cm^{-1}, using a moving average (MA) filter. Applying a filter on X affects also its distribution characteristics. That is, the resulting filtered cable distance to vehicle body is no longer distributed according to the shifted exponential distribution described by Eq. 2.49. The filtering effect can be better recognized on the probability density function (PDF) of X. In Fig. 2.11b the typical sharp peak of the PDF of the shifted exponential distribution, Fig. 2.11a, is slightly rounded. However, the minor modification of the distribution characteristic is here negligible.

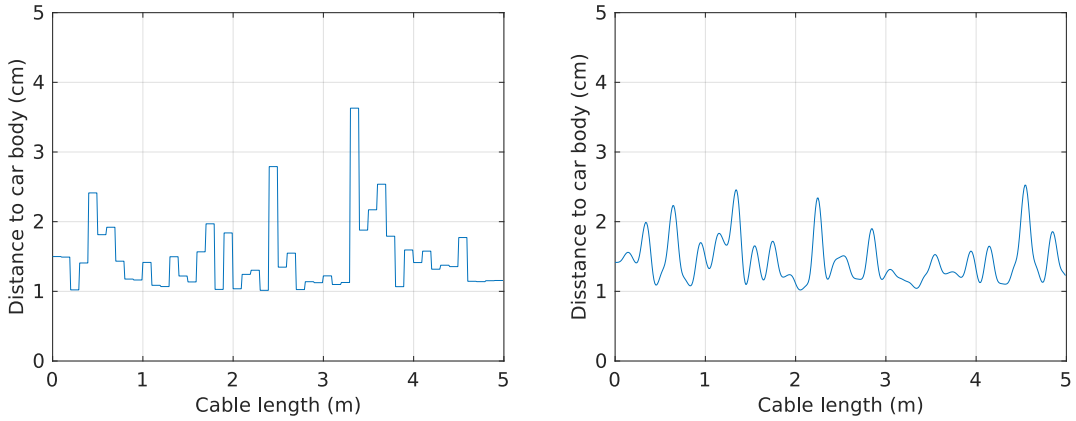

(a) Stepped distance between cable and car body

(b) Smoothed cable distance to car body

Figure 2.10.: Example of power line and its distance to the car body

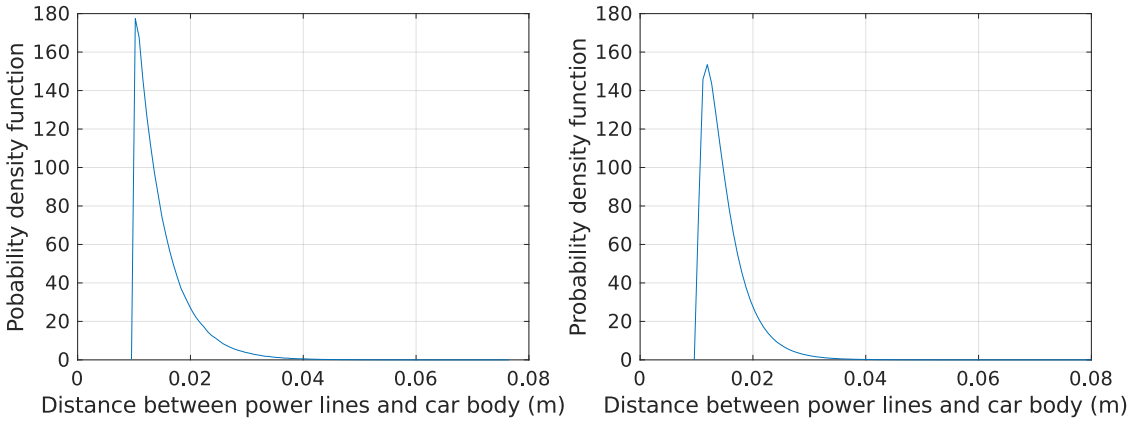

(a) PDF of X

(b) PDF of X smoothed by a MA filter

Figure 2.11.: Probability density function (PDF) of the distance between a power line and the car body obtained with Eq. 2.51

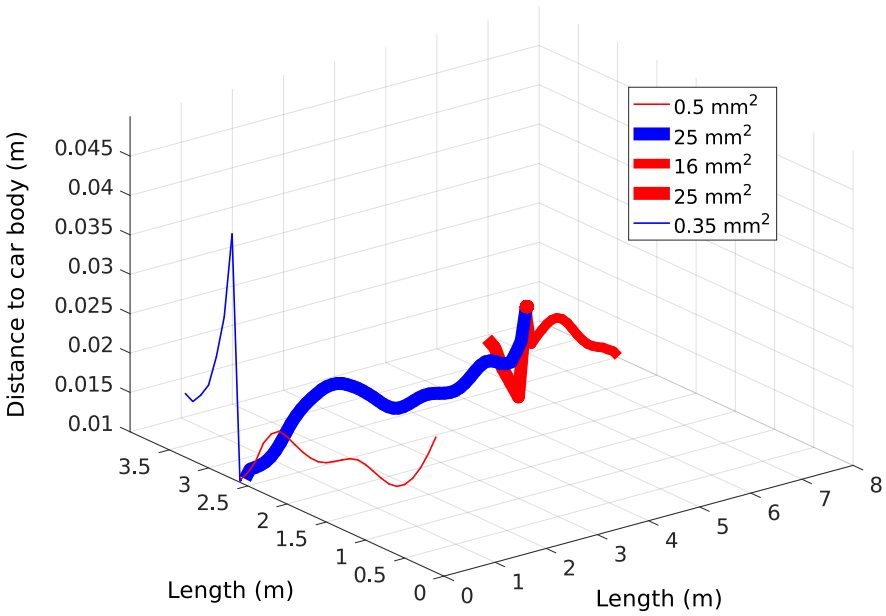

Figure 2.12.: Example of a non-uniform automotive transmission line

The above discussed scenario applies to a non-uniform transmission line consisting of a single line and without any bridge taps. By extending it to a more general case for non-uniform automotive power lines including bridge taps a further parameter needs to be taken into account. The cross sections of single car power lines strongly vary. While a PL connecting two power distributions may have a cross section of e.g. 25 mm^2 one connected to an electronic control unit accounts for only e.g. 0.35 mm^2 as illustrated by the example in Fig. 2.12. The varying cable cross section d is included by the characteristic impedance Z_c in the calculation of a chain matrix as described by Eq. 2.37.

2.2. Channel Attenuation Measurements

The measurements used to validate the theoretical results were performed on a BMW 5 series with full add-ons configuration, further described in Chapter 6. The scattering parameters are obtained by using a 2-port vector network analyzer with reference impedance $Z_0 = 50\ \Omega$. Having the S-parameters, it is straightforward to compute the transmission loss as shown in [10]. The measurements were performed in the frequency range (logarithmic spacing) from 1 MHz to 600 MHz. In total 10 access points on

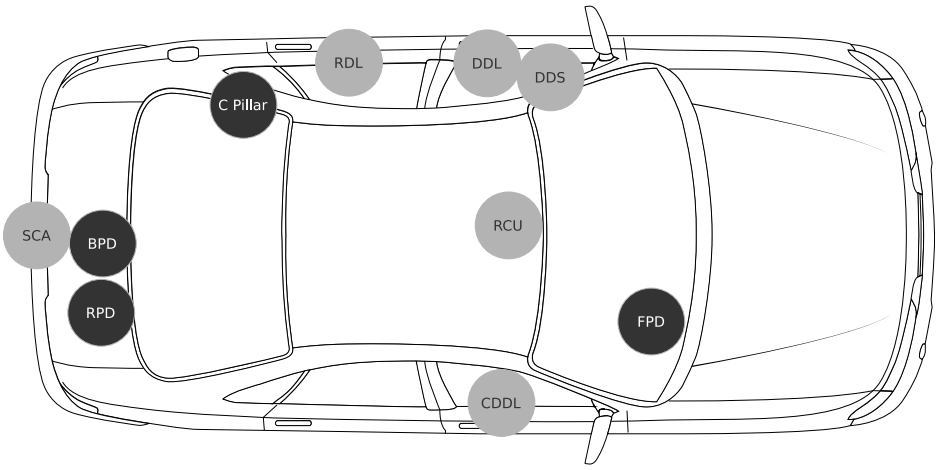

Figure 2.13.: Access points for transmission loss measurements: Front Power Distribution (FPD), Rear PD (RPD), Battery PD (BPD), Co-Driver's Door Left (CDDL), Roof Control Unit (RCU), Driver's Door Short Line (DDS), DD Long Line (DDL), Rear Door Left (RDL), Soft Close Automatic (SCA)

different power lines were used. Four of them were defined as primary (master) nodes and the other six as secondary (slaves). That is, measurements were made from every master to any other (i.e. slaves and masters) node. An overview of the location of all 10 access points is given in Fig. 2.13. Master and slave nodes are marked with dark gray and light gray circles, respectively. It is important to mention that all nodes are spread in different parts of the car, so that as much as possible diverse connections are obtained, which ensure a statistically relevant study.

The measured connections are of length between 1.5 m and 18 m and have a cross section between 0.35 mm^2 and 25 mm^2. Due to the BMW car architecture, the battery is located in the rear part of the vehicle. The measurement results from each master (FPD, RPD, BPD and C-pillar) to any other node are shown in Fig. 2.14. At first sight, it can be seen that all connections follow more or less the same trend and hence form the very specific automotive PLC channel characteristic which could also be observed by measurements done in previous works as [9, 25]. In-vehicle PLC channels act as a band pass filter with seemingly best transmission properties, motivated by lower attenuation, between 10 MHz and approx. 80 MHz. In this frequency range still a high variation of channel transmission loss magnitudes is measured. For further simulations and hardware tests a conservative loss-value of 40 dB is assumed which covers most of the observed scenarios.

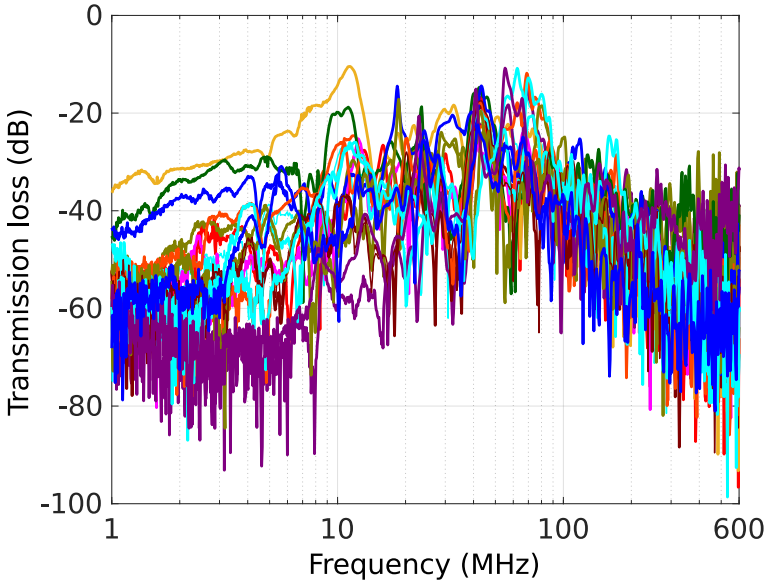

Figure 2.14.: Transmission loss measured from master nodes

2.3. Simulation Results and Discussion

An automotive PLC a transmission line is considered to comprise a transmitter and a receiver node, connected by the car's power line network. This section aims at analyzing the impact single system components have on an automotive PLC transmission channel. An in-vehicle PL transmission line is systematically composed and key parameters are studied.

2.3.1. Impact of the distance between power lines and car body

To estimate the impact of the varying distance between power lines and the vehicle body, numerical results were obtained for a transmission path with up to 98 tap lines. The used line setup is illustrated in Fig. 2.15. The main transmission path consists of two power lines with length l_1 and l_2, respectively. Up to 98 tap power lines are connected to the point of intersection between both main lines. In this setup, all lines are terminated by a real impedance $R_A = 50\ \Omega$. The lengths l_i, $1 \leq i \leq 100$, are logarithmically distributed between 0.5 and 10 m. The cross section of all power lines equals 0.35 mm^2. While Fig. 2.16a shows the channel transmission loss over the frequency range 1 - 600 MHz for a setup with up to 34 tap lines with the distance between all power lines and the car body being kept constant to 1.5 cm, in the simulation results depicted by Fig. 2.16b the distance is varying and distributed according

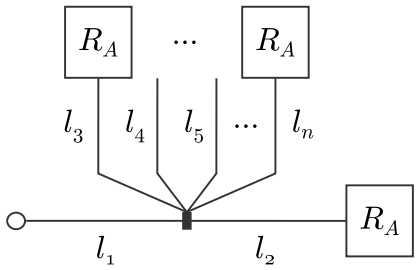

Figure 2.15.: Line setup used for evaluating the impact of varying distance between power lines and car body

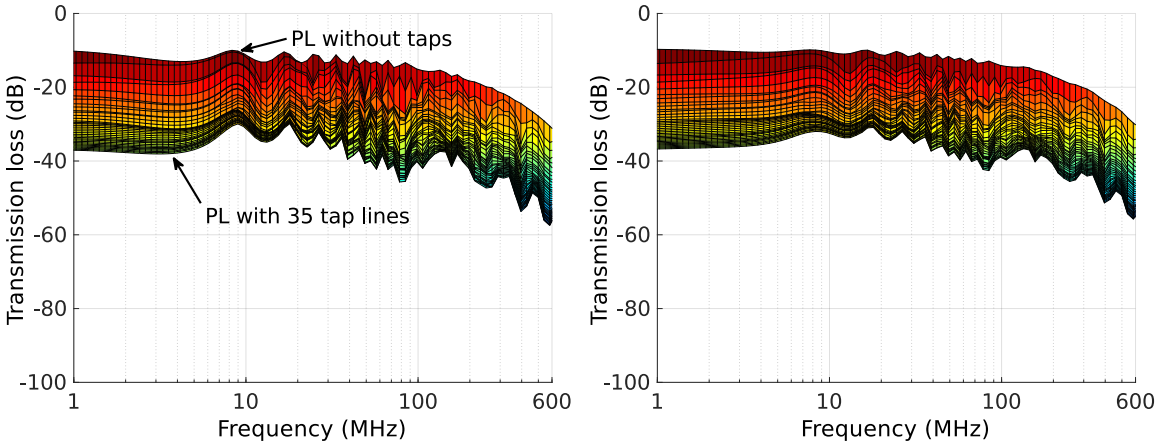

(a) Constant distance 1.5 cm

(b) Varying distance 1 - 5 cm

Figure 2.16.: Impact of varying distance to the car body

Eq. 2.51 between 1 cm and 5 cm. The topmost line in each figure represents a single main transmission PL without taps and the lowermost - with 34 taps. By observing the results of both simulations, it follows that a varying distance between cables and car body has only a minor impact on the channel transmission characteristic. Comparing Figs. 2.16a and 2.16b shows that by keeping the distance constant, increasing the number of taps results in a steady increase of transmission loss, plus an increasing oscillatory behavior at frequencies above 5 MHz. This oscillatory behavior is reduced due to averaging effects of the random distance variations in Fig. 2.16b. To validate these results, simulations with up to 98 taps were performed which feature a saturation on transmission loss (see also Section 2.3.3) for high number of taps and are for visualization reason not included in this figure.

2.3.2. Systematic composition of an automotive PLC channel

A direct comparison of the results from Fig. 2.14 and Fig. 2.16 does not give a good match. While Fig. 2.16 represents a generic in-vehicle PL, Fig. 2.14 illustrates the real performance of a complete automotive PLC system including ECUs, car battery, power distributions and power lines. Fig. 2.16 makes further clear that the high transmission loss at low frequencies is not an effect of power lines alone. Further, the overall attenuation level is much higher in a complete system. To reproduce the measured transmission system properties, specific PLC system components are systematically added to the simulation model. For the following presented results, discrete measurements in the frequency range (linearly spaced) of 1-40 MHz were conducted.

Fig. 2.17a depicts the channel transmission loss for a simulated and measured power line between the front and rear power distributions. It can be derived that the power line itself contributes on average less than 20 dB of transmission loss to the system. Considering a wiring harness built by hundreds of linked cables would obviously account for higher attenuation, as demonstrated in Fig. 2.16. However, the typical steep slope of the insertion loss at low frequencies up to 10 MHz seems not to be caused by the cables.

A battery supplies conventional vehicles with power and is consequently an essential part of an automotive PLC system. Many research is done on modelling different types of vehicle batteries as [26–28]. As a result, it can be concluded that a car battery features nearly no impedance (only some few mΩ) when used as a DC source [26, 27]. The presented simulation model is extended by a modified battery model by [26] for which a resistance $R_{bat} = 10$ mΩ and an inductance $L_{bat} = 100$ nH are connected in series. In most of the commercial vehicles a power distribution is connected to the car battery and is here modeled as a resistance $R_{PD} = 500\ \Omega$. Appending a car battery to the simulation model produces a transmission loss as illustrated in Fig. 2.17b. As confirmed by the measurements, the battery adds notable insertion loss. Further, the obtained results feature the specific high attenuation at low frequencies.

To complete the in-vehicle PLC system, the model is expanded by terminating the power line with an ECU. The input impedance of an ECU Z_{Load_ECU}, which acts as a load impedance in the PL system, differs depending on integrated non-linear components, e.g. voltage regulators. Based on measurements, an ECU is modelled by a capacity of 10 nF. Fig. 2.17c depicts the results for a power line with attached ECU. The results make it clear that the appended ECU provides further transmission loss.

The reasonable match of measured and theoretic data supports the accuracy of the simulation model.

2.3.3. Impact of Wiring Dimension and Load Impedance

In this section, the impact of the dimension of a wiring harness on the transmission characteristic is investigated. The conceptual cable configuration used for the simulations is illustrated in Fig. 2.18 and follows the general cabling structure of a BMW. This requires two power distributions (PDs), one in the front (FPD) and one in the rear part of the car (RPD). The car battery is connected to a separate PD unit - the battery PD (BPD). All ECUs installed in a vehicle are consequently connected to either FPD or RPD. RPD and BPD are modeled as discussed in Section 2.3.2 by a resistance of 500 Ω. The FPD features a specific characteristic and is modeled by a resistance of 5 Ω, 25 nH inductance and 5 nF capacity connected in parallel. The model and values were provided by BMW. The power lines connecting FPD and BPD as well as the battery and BPD have a cross section of 25 mm^2 and a length of 6 m and 0.5 m, respectively. The cross section of the power line between RPD and BPD accounts for 16 mm^2 and has a length of 2 m. The cross section of a power line connecting an ECU is 0.35 mm^2. This data corresponds to a general power line cabling of a BMW vehicle independent of its specific configuration and is summarized in Tab. 2.1.

Following procedure was used for evaluating the impact of the wiring dimension. First, a main transmission line from TX to RX with a given load impedance Z_{Load} and without any tap lines, i.e. k = 0 in Fig. 2.18, is assumed in the initial simulation scenario. TX and RX could be both an ECU or any other unit connected to the car power line network transmitting or receiving control data. In the next simulation steps, subsequently, up to k = 34 tap lines with the same load impedance Z_{Load} are attached. Although, load impedances introduced by different ECUs are not equal in real systems, the proposed ECU modeling in Section 2.3.2 is a good average representation as confirmed by measurements (Fig. 2.17c). The wiring harness of most conventional cars includes two main power distributions – a front and a rear one (FPD and RPD). Both power distributions as well as the car battery and the BPD are considered in every simulation scenario. Car wiring lengths are not subject to any particular distribution and are defined on demand. However, it is known that shorter cables with a length of up to 3 m are more frequently used than e.g. 10 m long lines. Thus, all lines, except for the power lines between RPD-BPD, BPD-Bat and BPD-FPD, in the simulation model have random lengths which are logarithmically distributed between

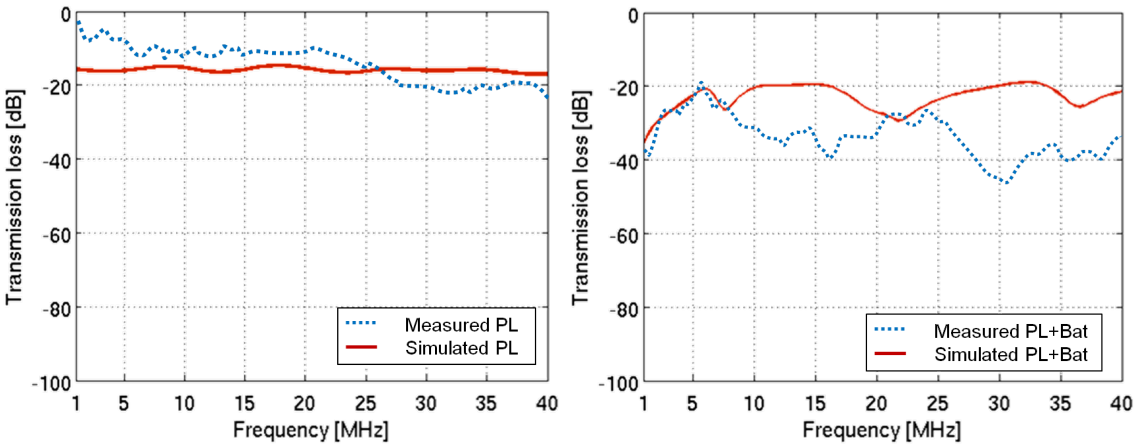

(a) Transmission characteristic of a PL

(b) Transmission characteristic of a PL and car battery

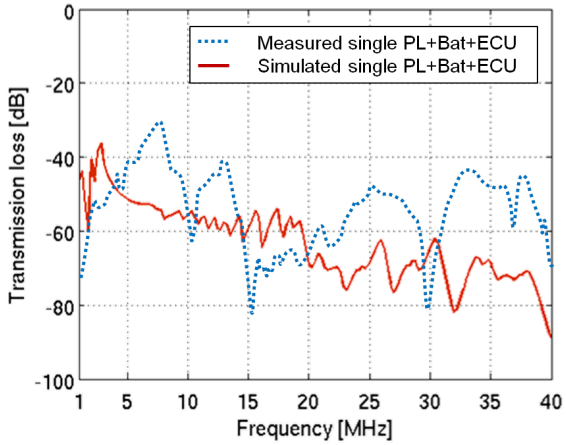

(c) Transmission characteristic of a PL, car battery and an ECU

Figure 2.17.: Transmission characteristics

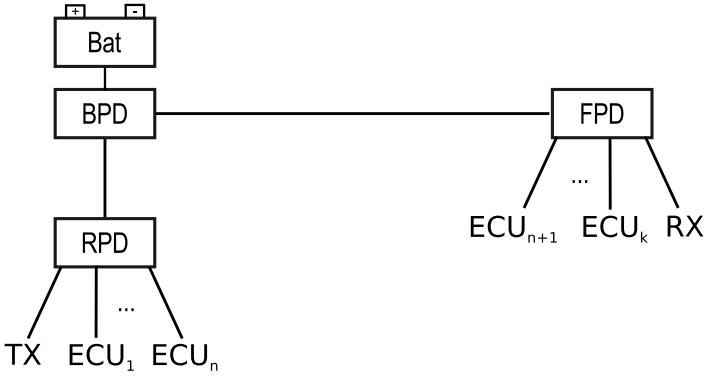

Figure 2.18.: Conceptual automotive PLC wiring

Power line	Cross section (mm^2)	Length (m)
BPD - FPD	25	6
BPD - RPD	16	2
BPD - Battery	25	0.5
ECU - FPD/RPD	0.35	0.5 - 10

Table 2.1.: Cross section and lengths of used car power lines

0.5 m and 10 m.

Three cases for three different load impedances Z_{Load} are studied and the obtained results are presented in Fig. 2.19, 2.20 and 2.21, respectively. The first, state of the art scenario, is for $Z_{Load} = 10$ nF as explained in Section 2.3.2. Second, by a slight modification of the ECUs by attaching an inductance of some μH in series before the capacity, a inductive PLC coupling can be realized. Thus, in the second scenario Z_{Load} equals 10 μH - 10 nF connected in series. In the third scenario, the impact of a theoretical pure resistive line termination of 50 Ω is analyzed. In each figure two perspectives of each numerical result are given. The first one represents the transmission loss over frequency. As in Fig. 2.16, the topmost curve in the graphic depicts a single main PL without tap lines and the lowermost - with 34 taps. The second perspective illustrates the transmission loss distribution for different number of tap lines over frequency. The transmission loss is color coded and the equivalent color legend is given at the bottom of Fig. 2.19. The same color code is used in all three figures.

It can be seen that the state of the art realization for $Z_{Load} = 10$ nF features a high number of notches, thus providing only small continuous frequency bands with low transmission loss. Including an inductance, helps improving the channel characteristic by introducing some additional low attenuation areas for lower frequencies below

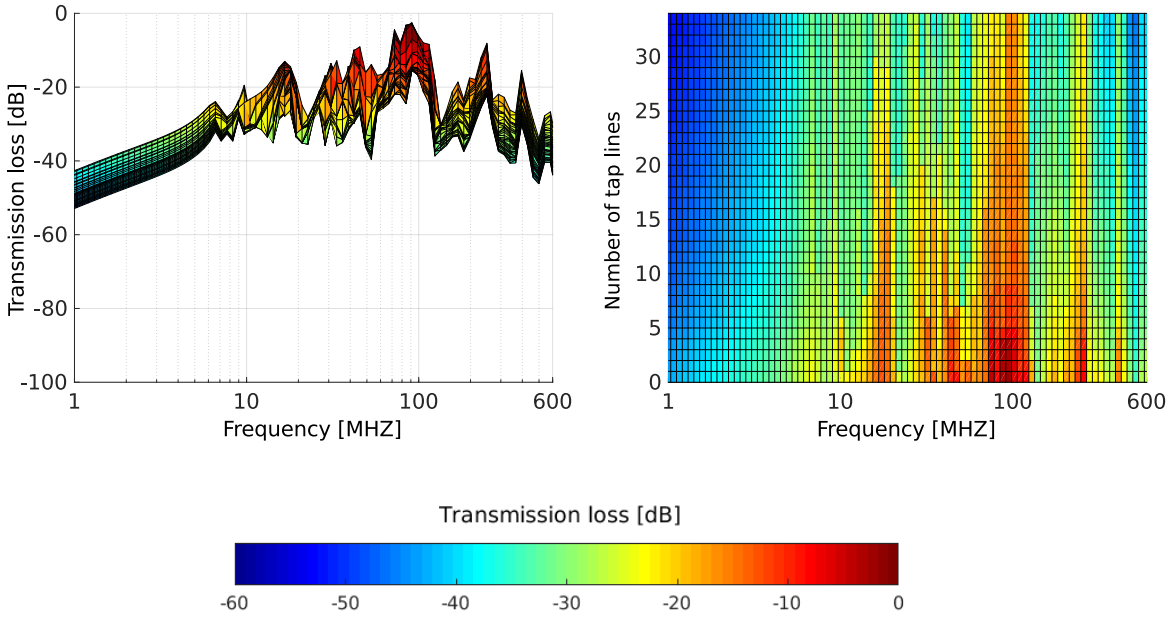

Figure 2.19.: Impact of wiring dimension and load impedances for $Z_{Load} = 10$ nF

10 MHz. By using 50 Ω as a line termination, the overall transmission loss level is slightly higher. However, a continuous and smoother attenuation range producing less distortion is now available. This allows for the allocation and usage of a broader transmission frequency band characterized by a less frequency selective behavior. Therefore, it can be concluded that a pure resistance as a line termination would improve the transmission performance. Further, a saturation on transmission loss can be observed in all three cases for 10 to 15 tap lines which was verified by simulations for up to 98 taps.

2.4. Summary

This chapter summarizes the efforts on characterizing the transmission properties of an automotive PLC channel. The introduced channel model, based on the two-port network theory, allows for a systematic and component-wise assembling, and analysis of the channel. S-parameters are used to represent a single two-port and calculating the channel transfer function. Additionally, a statistical modeling of the random distance between a power line and the car body is given. The impact of this distance on the channel transmission loss was evaluated and it could be shown that a varying distance of the power lines to the car body has a rather positive effect of providing a smoother

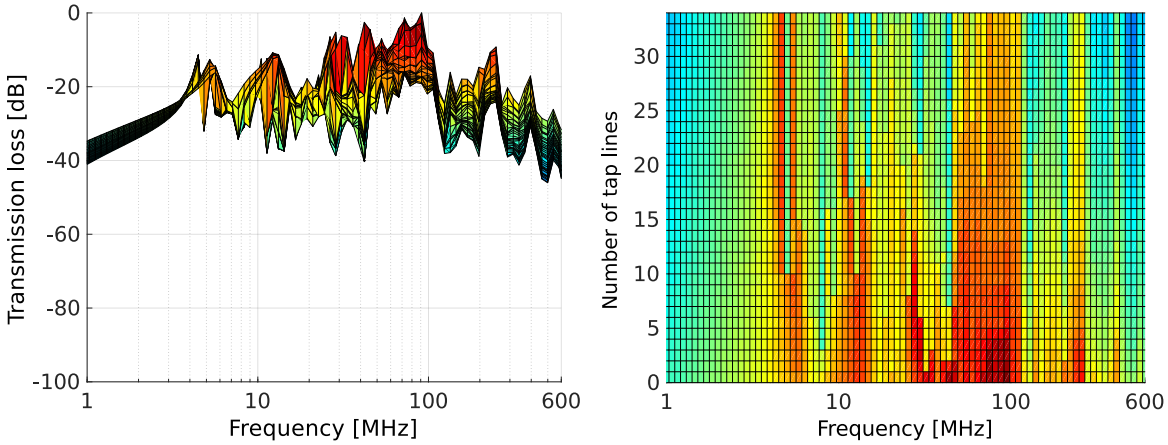

Figure 2.20.: Impact of wiring dimension and load impedances for Z_{Load} = 10 μH - 10 nF

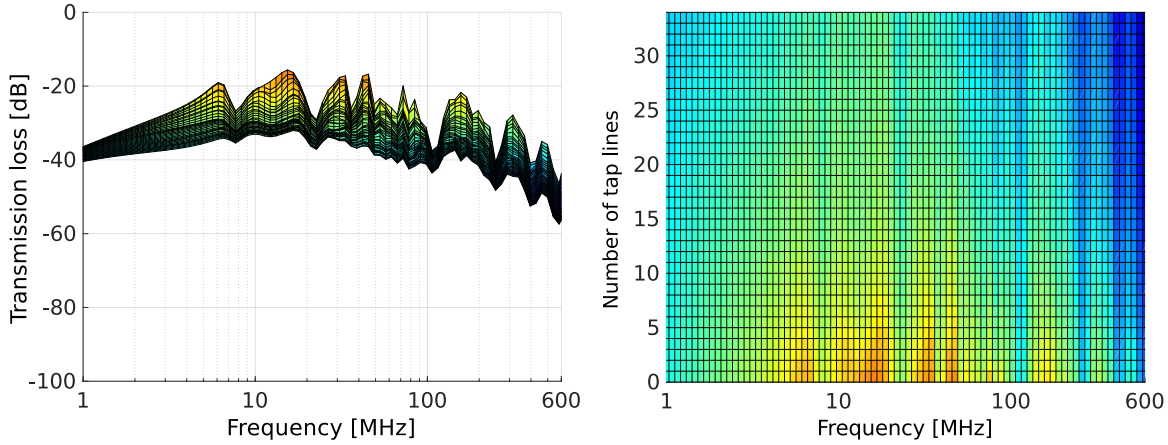

Figure 2.21.: Impact of wiring dimension and load impedances for $Z_{Load} = 50\ \Omega$

transmission characteristic with less notches in the frequency domain. Extensive measurements in a test vehicle provided data for comparison and investigation of the car power line network. It is observed, that some transmission paths, such as from RPD to FPD, experience a very poor transmission quality compared to others, the reason being that the power distributions present in the test vehicle (FPD, BPD and RPD) introduce a high attenuation. For performance evaluation purposes, discussed later in Chapter 5, a conservative average channel attenuation value of 40 dB is assumed. By a systematic composition and analysis of the main components of a car power line network, it could be observed that car power lines themselves have only a negligible impact on the overall PLC channel transmission characteristics. Though, the vehicle battery introduces additional attenuation over the whole analyzed frequency range 0 - 40 MHz, the load impedances introduced by the internal termination of the ECUs are strongly impacting the channel characteristic. Finally, an extensive study on the impact of the wiring dimension and load impedance on the PLC channel characteristics was performed. For this purpose, the performance of a complete automotive power line network was evaluated. In each simulation scenario the car battery, all three power distributions (FPD, RPD and BPD) as well as the power lines connecting them are considered. Subsequently, up to 34 tap lines terminated by an ECU, represented by the load impedance Z_{Load}, are added to either FPD or RPD. The transmission loss was evaluated for three different Z_{Load} values namely 10 nF, 10 μH - 10 nF and 50 Ω. It can be observed, that while a pure resistive termination introduces additional overall attenuation, it allows for a smoother transmission loss over the observed frequency range of 0 - 600 MHz and hence, less frequency selective behavior of the channel.

3

Channel Noise

This chapter summarizes the efforts put on analyzing and modeling the noise present on an automotive power line channel. This way, it gives a better understanding of the in-vehicle noise characteristics. Several models are discussed for the superimposed impulsive noise. The second part of the chapter is dedicated to the channel noise. First, the noise measurement results from the test vehicle are introduced and evaluated. The observed noise types are then classified into four categories based on different parameters. Following, several models for modelling impulsive noise are presented. Their application in the automotive PLC system evaluation is discussed in Chapter 5.

When describing the transmission characteristics of an automotive PLC system, it is important to recall that the car power lines are a shared medium. The in-vehicle power network connects all devices which rely on energy supply and account for hundreds nowadays. The normal operation of these devices or switching them on and off, results in distortion and energy peaks on the commonly used power lines. Historically, the automotive power line network was growing by only scaling its size and number of attached devices. In addition, the per vehicle deployed electrical devices are mostly delivered by different producers and no interface standards are available. This leads to an impedance mismatch at each network termination point which in turn results in frequency notches in the frequency response of the power line channels as shown in Fig. 2.14. The underlying cabling concept was not adapted to the emerging needs for a heterogeneous and flexible communication network. Hence, in the efforts to characterize the automotive PLC channel, this section describes the performed in-vehicle noise measurements and discusses the obtained results. Especially, the observed

impulsive noise can have a great impact on the performance of an automotive PLC system which requires its in depth investigation.

This chapter begins with a study of the characteristics of an impulsive noise present on an in-vehicle PLC channel. Systematic measurements were performed in an automotive environment. The obtained data was analyzed to extract relevant parameter values such as impulse duration and amplitude. This chapter then proceeds to present several statistical models for modeling an impulsive noise.

3.1. Measurements

PLC has been used as an indoor communication technique and as a solution for the last-mile in Smart Metering for many years. Accordingly, a lot of investigations on the channel characteristics including the present noise have been done. From measurement results, e.g. in [29–34] and [35], it is known that PLC channels are subject to high interference and impulsive noise. Due to the increasing interest of the automobile industry on PLC, some recent works as [12–14] and [15] have published their measurement results of the noise present on an in-vehicle power line channel. The presented results exhibit partly great difference. Pulses with duration from 50 ns [14] up to 55 µs [12, 13] and with amplitudes ranging from 100 mV [12, 15] to more than 10 V [14] were experienced.

This section presents the results obtained by intensive measurements carried out on a BMW X5 (F15) with all power consumers being active which are connected to an electrical terminal contact 30 (battery powered, also called clamp 30) or 15 (ignition powered). For capturing the noise sequences in the time domain a LeCroy waverunner 6100A 1 GHz oscilloscope was used. Sequences with 1 MS/s and 100 MS/s sampling rate were captured. A balancer as described in Section 6.1 was installed between the car and the oscilloscope to isolate the DC voltage between those. The measurements were performed at six predefined access points (AP) and 9 different actions were executed at each measuring point while capturing. The position and labels of the access points are given in Fig. 3.1. The performed actions were operating the breaks, window lifter, wipers and seat adjustment, switching on and off the fan, radio, turn signals and seat heater. The noise was also measured at each access point without undertaking any action. For each (AP, action) pair, several noise sequences were captured. While the measurement results from [12–14] and [15] have captured noise sequences of up to 95 ms duration, the data presented in this section contains noise sequences up to 8 sec long. The very long captures allow for the recognition of e.g. long term periodicity. In

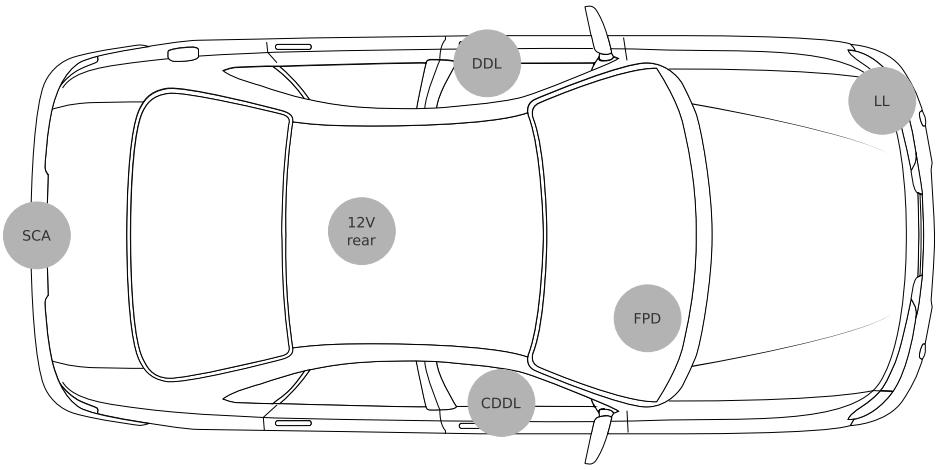

Figure 3.1.: Access points for noise measurements: Front Power Distribution (FPD), Light Left (LL), Driver's Door Long (DDL), Co-Driver's Door Long (CDDL), 12 Volt Access at Rear Seats (12V rear), Soft-Close-Automatic for the trunk (SCA)

total 670.4 sec of noise present on the automotive PL channel were captured - 616 sec with a sampling rate of 1 MS/s and 54.4 sec with a sampling rate of 100 MS/s. A continuous noise sequence is 8 sec and 0.8 sec long for the 1 MS/s and 100 MS/s measuring scenario, respectively.

3.2. Characterization and Classification

By analyzing the measurement results in time and frequency domain, some specific noise characteristics can be observed. Fig. 3.2a illustrates the cumulative distribution of the power of the three highest peaks in the power spectrum of a noise sequence. That is, the power spectrum of each measured noise sequence was calculated and the power of the three most significant peaks was recorded and the cumulative distribution computed. The noise sequences could be of any type, e.g. background noise, highly impulsive noise or a mixture. The graph further includes two data markers, one representing the 50th percentile and another, the 90th percentile. The power of half of these most distinct peaks lies below -81.8 dBm and already 90 % of them do not exceed a power level of -57.9 dBm. These results are of a great importance for setting up a lab environment to emulate an in-vehicle power line transmission, discussed in Ch. 6, Sec. 6.3. By taking a closer look at the power distribution of those same peaks over the frequency, shown in Fig. 3.2b, three distinct clusters can be identified. These are at 16.7 MHz, 25 MHz and 33.33 MHz, respectively. In total 82.6 % of all analyzed

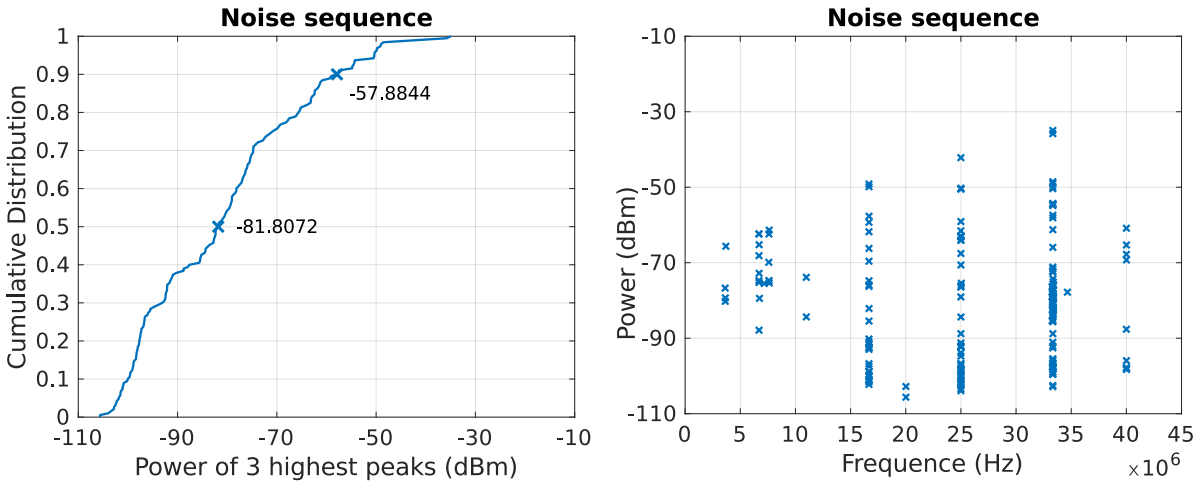

(a) CDF of peak powers in power spectrum (b) Power distribution over frequency

Figure 3.2.: Power distribution of the three highest peaks in the power spectrum of a noise sequence

peaks are located in the clusters: 43.1 % in the cluster at 33 MHz, 23.2 % in the cluster at 25 MHz and 16.3 % in the one at 16.7 MHz. For building an FPGA-based automotive PLC demonstrator, presented in Ch. 6, a carrier frequency of 25 MHz is used due to the low channel attenuation observed in the surrounding frequency range (see Ch. 2). Though, the chosen carrier frequency overlaps with one of the noise peak power clusters, its power level barely exceeds −60 dBm, which is already considered noise power level.

Similar analysis was performed on a single impulse basis. Fig. 3.3a depicts the cumulative distribution of the peak power in the power spectrum of isolated impulses. As expected, single impulses introduce higher noise power than general, mixed noise. The 50th and 90th percentile are again marked at the graph and correspond to −50.26 dBm and −39.36 dBm, respectively. The peak power distribution over frequency is given in Fig. 3.3b. Comparing it to the results in Fig. 3.2b, it can be noted that the power peak cluster at 33 MHz occurs in both graphs. The peak clusters at 25 MHz and 16 MHz are on the contrary only for the complete noise sequences given. Due to the linearity of the Fourier transform, it can be concluded that with high probability the power peaks at 33 MHz in Fig. 3.2b are caused by impulsive noise, while those at 25 MHz and 16 MHz, are most likely to be originated by the background noise. In the case of single impulses, the power peaks around 33 MHz include 39.3 % of the total analyzed impulses and their peak power is concentrated between −40 dBm and −80 dBm. The majority of the remaining peaks are below 10 MHz. Hence, the trans-

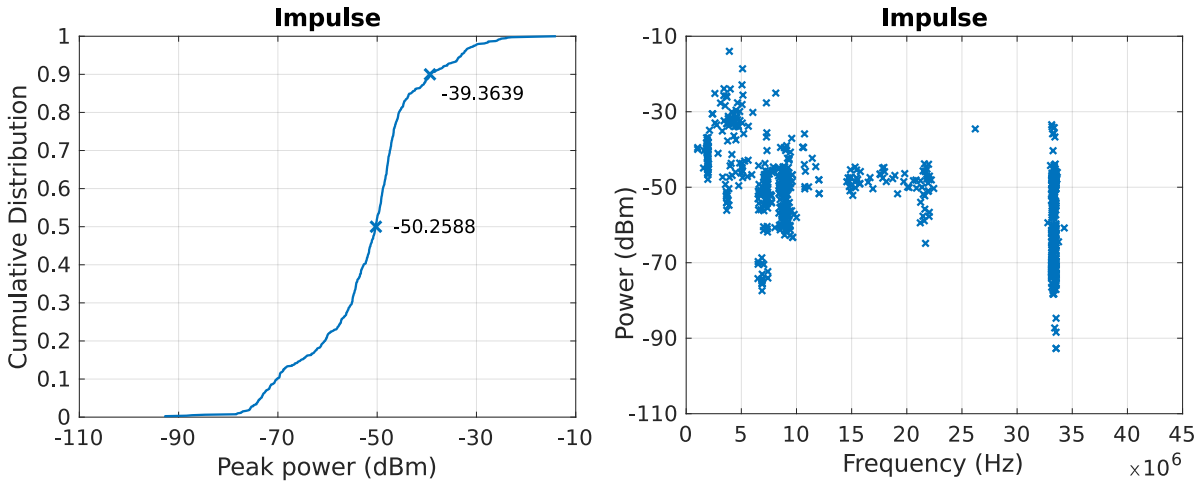

(a) CDF of the peak power in power spectrum (b) Power distribution over frequency

Figure 3.3.: Peak power distribution of an impulse

mission band around 25 MHz, chosen for building a demonstrator, is to a great extent free of interruptive sources.

The results of a time domain analysis on the impulse peak amplitude is depicted in Fig. 3.4. It can be seen, that impulses can reach an amplitude up to 1.3 V. However, already 90 % of them do not exceed an amplitude of 96 mV. Again, the 50th and 90th percentile are marked on the graph.

By observing the complete obtained measuring results, the noise present on an automotive PLC channel can be classified in several categories regarding its peak amplitude, impulse duration, time development and the time between successive pulses (interarrival time, IAT).

The most trivial noise is the background noise. It is always present on the PL channel regardless of the monitored AP. Based on the analysis of the performed measurements, its amplitude follows a Gaussian distribution as shown on the example of Fig. 3.5. It has a maximum peak amplitude (V_p) of 309.36 mV. However, in 50 % of the cases it is below 22.09 mV and already the 90th percentile is at 123.76 mV, as illustrated by Fig. 3.6a. As a comparison, [13] treats pulses with an amplitude greater than 70 mV as impulsive noise. Consequentially, the background noise is considered to be below this level. 70 mV corresponds to the 82th percentile of the measured data discussed in this chapter. By further evaluating the captured data, it can be observed that the variance in the amplitude does neither correlate with the AP location nor with a single operated action. The cumulative distribution function (cdf) of the measured V_p and standard deviation of the background noise (σ) is depicted in Fig. 3.6a and 3.6b,

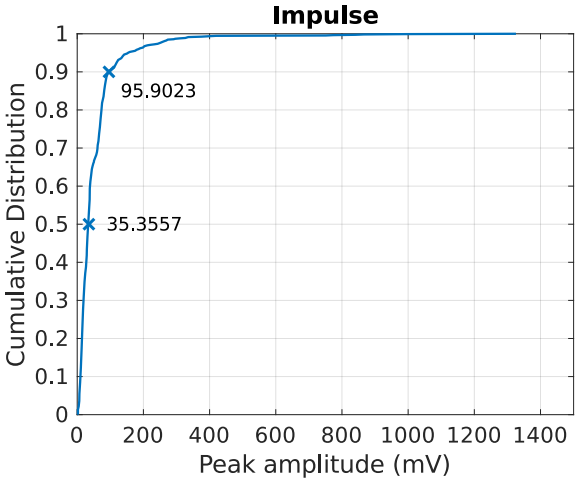

Figure 3.4.: Peak power distribution of single impulses

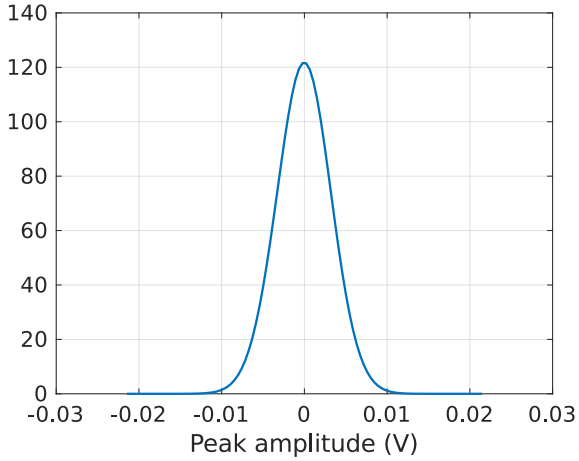

Figure 3.5.: Amplitude PDF of the noise captured at DDL with turned on radio

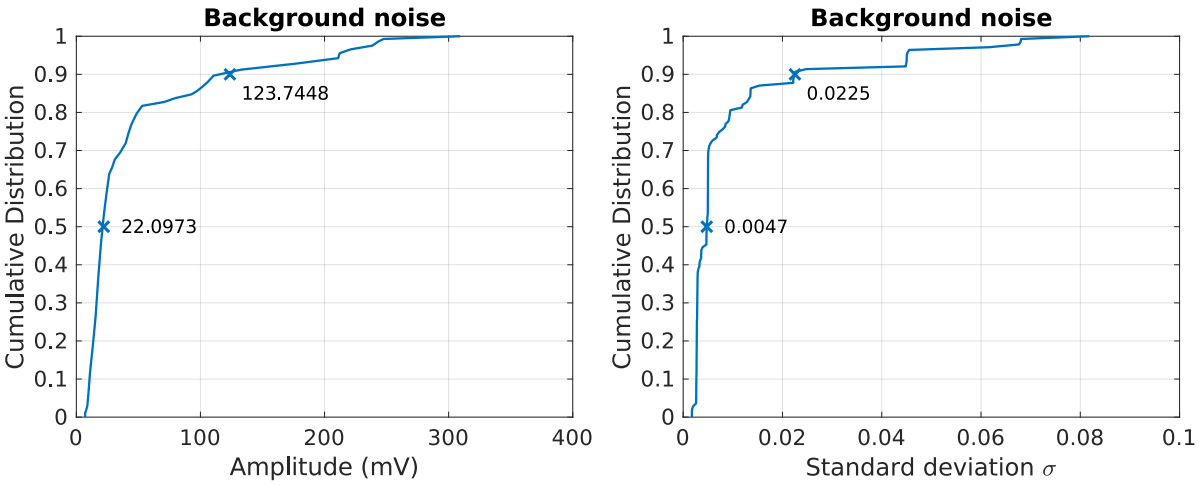

(a) CDF of background noise V_p

(b) CDF of background noise σ

Figure 3.6.: Distribution of the peak amplitude and standard deviation of measured background noise

respectively. A typical representation of the background noise is shown in Fig. 3.7a.

Besides the background noise, another dominant interference source is the superimposed impulsive noise. Regarding the non-Gaussian noise with impulsive nature, it can be classified in different categories. [13] classifies the impulsive noise in single pulse and bursts while differentiating between long and short duration single pulses with a low and high frequency content, respectively, and bursts having a low ($<$ 500 kHz), medium ($>$ 500 kHz and $<$ 3 MHz) and high ($>$ 3 MHz) frequency content. In [14], the detected noise is classified in two groups: damped sine waves and bursty waves. This work proposes a new categorization of the non-Gaussian impulsive noise observed on an in-vehicle PLC channel by introducing three main classes of periodic, random and predictable impulse noise. Exemplary representatives are shown in Fig. 3.7b, 3.7c and 3.7d, respectively. The classification is done based on the distinct noise characteristics identified in time domain. A detailed description of each proposed noise class follows in this section.

Periodic impulsive noise is characterized by multiple pulses arriving with a more or less constant interarrival time (IAT). The single pulses feature only a small difference in amplitude and duration. In the example of Fig. 3.7b, 12 pulses arrive within 8 s with an IAT of 640 ms and an amplitude span between 207.7 mV and 214.3 mV, which accounts for a maximum amplitude difference of 6.6 mV. This noise sequence was captured at the 12_V rear AP while operating the left turn signal. Based on the obtained measurements, periodic impulsive noise in general does not reach high

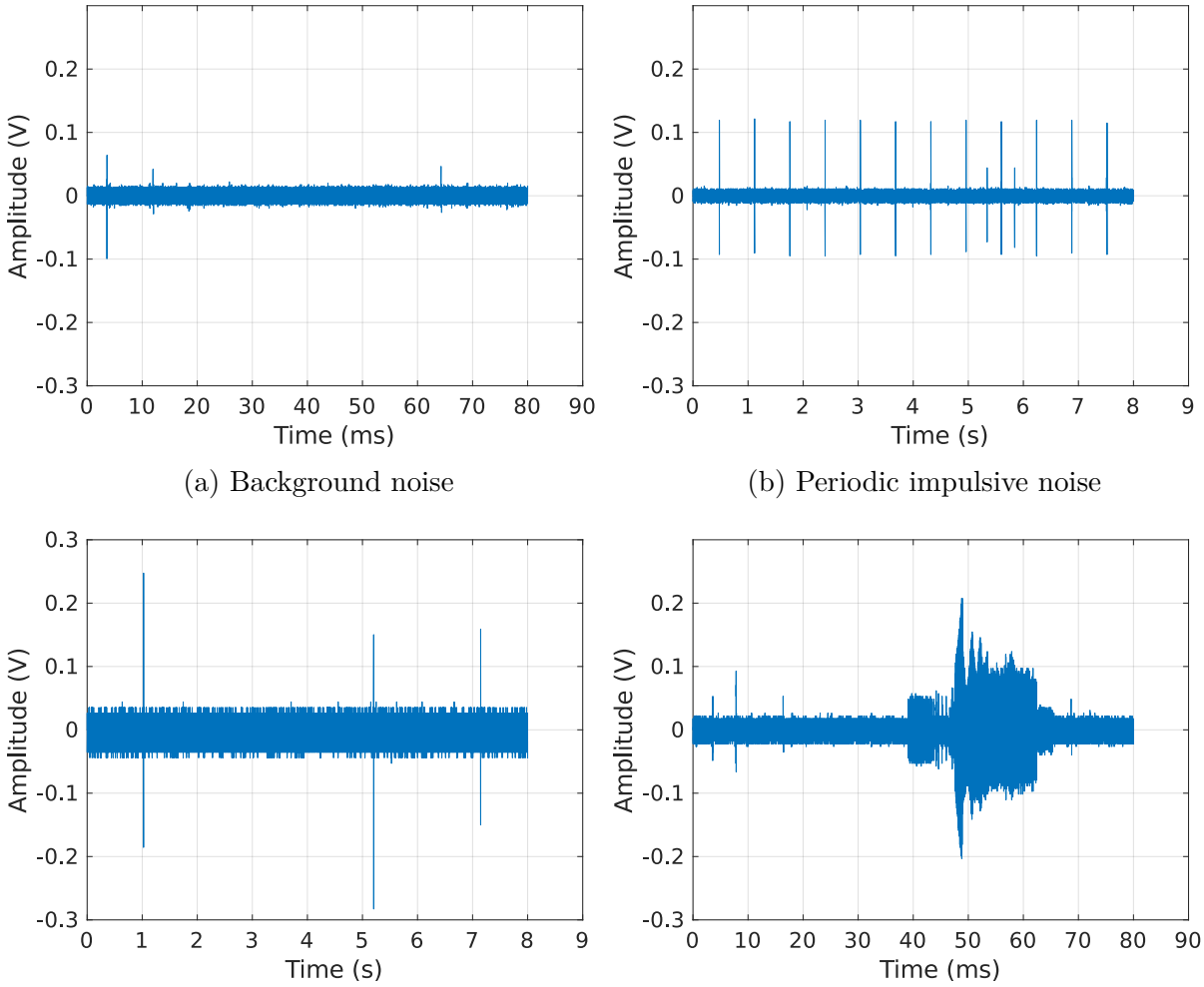

(a) Background noise

(b) Periodic impulsive noise

(c) Random impulsive noise

(d) Predictable impulsive noise

Figure 3.7.: Different noise types measured on the automotive PLC channel

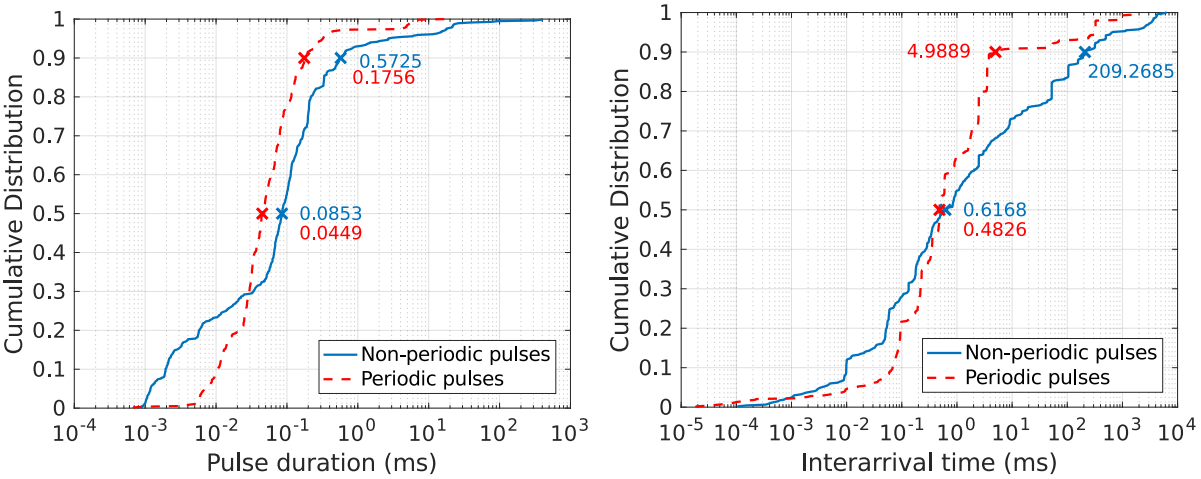

(a) CDF of pulse duration

(b) CDF of interarrival time

Figure 3.8.: Distribution of the duration and IAT of periodic and non-periodic pulses

amplitudes beyond 220 mV and is of a rather short duration with mostly up to 175 µs. Fig. 3.8a shows the cumulative distribution of the pulse duration observed within the measured data. The blue solid line represents the duration distribution of non-periodic pulses, while the red dashed line shows the periodic ones. It can be seen, that the periodic pulses do not reach as long durations as pulses of other noise classes. The longest observed duration of a periodic pulse accounts for 17.27 ms and of non-periodic pulses 400 ms. Further, the values of the 50th and 90th percentile for periodic and non-periodic pulses are given in red and blue color, respectively. As the duration of 50 % of the periodic pulses is within 44.9 µs, the one of non-periodic pulses is nearly double with 85.3 µs. The variance is getting bigger when considering a higher percentage of the observed pulses. Similar behavior shows the cumulative distribution of the IAT, illustrated in Fig. 3.8b. Again, the red dashed line represents the IAT for periodic pulses, while the solid blue one, for non-periodic. Half of the periodic and non-periodic pulses arrive within 482.6 µs and 616.8 µs, respectively. However, the 90th percentile of the periodic pulses is only at 4.9 ms and of non-periodic pulses, already at 209.2 ms. The longest experienced IAT of periodic pulses is 1.5 sec, while for non-periodic it reaches 6.3 sec. Table 3.1 summarizes the measured noise parameters and some of the evaluated quantities.

The two smaller amplitude pulses, occurring between pulse 8 and 10 in Fig. 3.7b, are to be categorized as randomly occurring pulses and are not treated as part ot the periodic sequence.

	min	max	50th percentile	90th percentile
Sequence power peaks (dBm)	-105.6	-35	-81.8	-57.9
Impulse power peak (dBm)	-92.7	-14	-50.2	-39.4
Impulse peak amplitude (mV)	2.2	$1.3 \cdot 10^3$	35.6	96
Gaussian peak amplitude (mV)	7	309.4	22	123.7
Pulse duration, periodic (µs)	0.68	$17.3 \cdot 10^3$	45	175.6
Pulse duration, non-periodic (µs)	0.8	$400 \cdot 10^3$	85.3	572
IAT, periodic (ms)	$18.6 \cdot 10^{-6}$	$1.5 \cdot 10^3$	0.5	5
IAT, non-periodic (ms)	$108 \cdot 10^{-6}$	$6.3 \cdot 10^3$	0.6	209.3

Table 3.1.: Summary of the measured noise parameters and evaluated statistical quantities

Random impulsive noise represents pulses which occur randomly in time and irrespective of past events. In all figures of Fig. 3.7 there are occurrences of random pulses. Their amplitude is also random and ranges within the obtained measurements from a few µV above the background noise level up to 1.3 V. The pulse duration varies between 50 µs and 2.5 ms. However, the majority of the pulses are lasting for less than 100 µs.

By analyzing the measurement results, a fourth category of predictable impulsive noise can be clearly distinguished. An example of predictable impulsive noise, measured at the DDL AP while operating the seat readjustment on the driver's seat, is given in Fig. 3.7d. This type of noise is embossed by its predictable behavior. Whenever a certain action is performed in a vehicle, e.g. operating the window regulator, a designated consumer is activated which introduces in most of the obtained measurements a very specific and predictable noise figure to the car power line network. Certainly, the intensity of the produced pulse(s) varies at different points of the network. Also the pulse(s) shape(s) might slightly change. However, the main characteristic remains for all measured points. Most of the observed representatives of the predictable impulsive noise captured by the measurement data are pulse sequences with a complex pattern. That is, the impulsive noise is compound by multiple pulses each with a predefined amplitude and arriving at a specific instant of time. Hence,

predictable impulsive noise has foreseeable start and end points in time. As an example, Fig. 3.9 shows the impulsive noise caused by operating the seat adjustment on the driver's seat, captured at four different access points in the car. As previously mentioned in Section 2.2, the highest channel attenuation is present on the path between the front and the rear power distribution of the car. The measuring points of Fig. 3.9a and 3.9b are both located in the front part of the car, i.e. they are directly or indirectly connected to the FPD, close to the activated consumer. Thus, the noise signal present at these metering points does not pass the critical path between FPD and BPD (cf. Chapter 2), which explains the relatively high amplitude of the noise with a maximum of 0.4 V. On the contrary, the capturing point of Fig. 3.9c is located in the back of the car, which implies that the noise signal travels the high attenuation path between the front and battery power distributions. This justifies the low signal amplitude of just above 0.1 V. The lowest amplitude is measured directly at the FPD, Fig. 3.9d, which adds additional attenuation. Despite the varying amplitudes, the overall characteristic of the introduced noise sequence is recognizable in all four figures. First, two short pulses (marked within a red box) announce the arrival of a burst with a duration of 26 ms around 30 ms later. It is characterizing for the pulses comprising a predictable noise signal that their duration is much longer than periodic or random noise pulses. A predictable impulsive noise behavior is observed for multiple consumers and at all measuring points. The knowledge of their pattern and frequency of occurrence, e.g. operating the window regulator is a more frequent action than adjusting a seat position, may be used to optimize the PLC transmission system and its performance.

An algorithm was developed and applied for the impulse recognition. A description in form of pseudocode is given in Appendix C.

3.3. Modeling

In this section, first the mathematical description of an analog and a sampled impulse are presented, and then several statistical models for the modeling of real impulsive noise in an automotive PLC transmission environment are considered. First, a more basic filter-based model is presented which only offers a few parameters to adjust the generated impulsive noise. In addition, the Middleton's class A model is presented as a complex but accurate model followed by the symmetric alpha stable model which is suggested as a simplified alternative to Middleton's class A model. Finally, the Gaussian mixture model as an approximation of the Middleton's class A model is

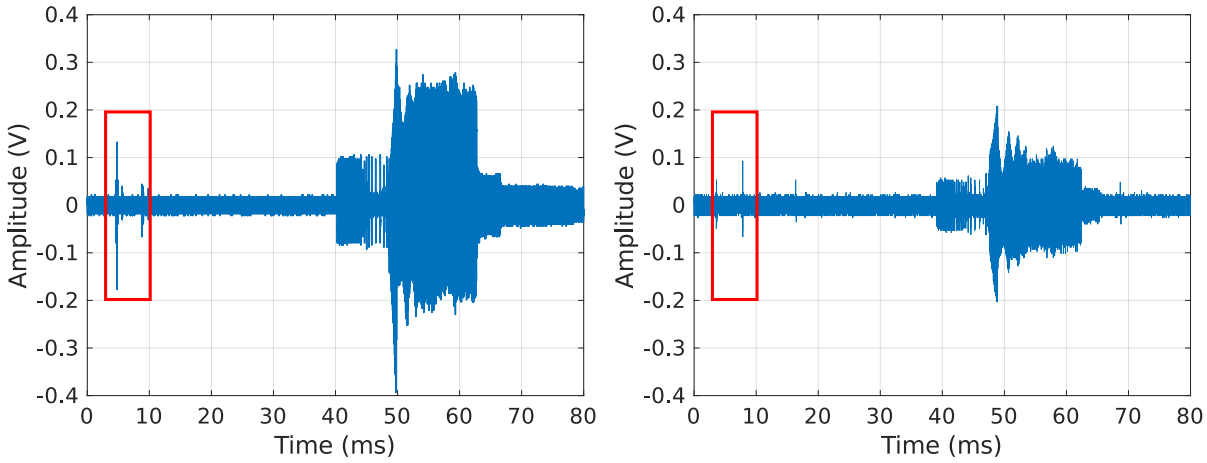

(a) Measured at 12V rear

(b) Measured at DDL

(c) Measured at SCA

(d) Measured at FPD

Figure 3.9.: Predictable impulsive noise introduced by adjusting the driver's seat

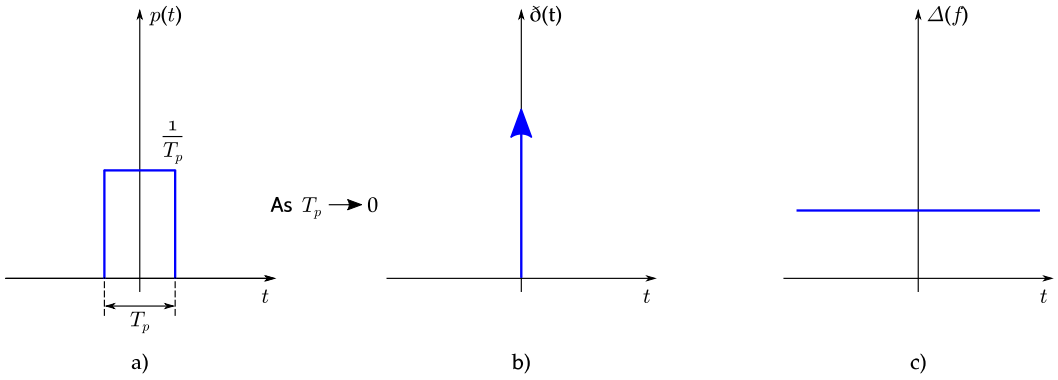

Figure 3.10.: a) A unit-area pulse; b) Dirac; c) The spectrum of a Dirac impulse

discussed. The introduced models are later used for evaluating the performance of an in-vehicle PLC system as discussed in Chapter 5.

3.3.1. Mathematical fundamentals of an impulse

A unit-area analog pulse is shown in Fig. 3.10a). As the pulse width T_p tends to zero, the pulse tends to a dirac impulse as depicted in Fig. 3.10b). A dirac impulse is defined as a pulse with an infinitesimal width and can be described by

$$\delta(t) = \lim_{T_p \to 0} p(t) = \begin{cases} \frac{1}{T_p}, & |t| \leq \frac{T_p}{2} \\ 0, & |t| > \frac{T_p}{2} \end{cases} \tag{3.1}$$

with its integral function given by

$$\int_{-\infty}^{\infty} \delta(t)dt = T_p \cdot \frac{1}{T_p} = 1. \tag{3.2}$$

The spectrum of a dirac is obtained by

$$\Phi(f) = \int_{-\infty}^{\infty} \delta(t)e^{-j2\pi ft}dt = e^0 = 1. \tag{3.3}$$

As shown in Fig. 3.10c) the spectrum of a dirac impulse contains all frequencies in equal amounts.

A digital impulse $\delta(m)$ is a signal with an "on" duration of one sample [36], which is expressed as

$$\delta(m) = \begin{cases} 1 & m = 0 \\ 0 & m \neq 0 \end{cases} \tag{3.4}$$

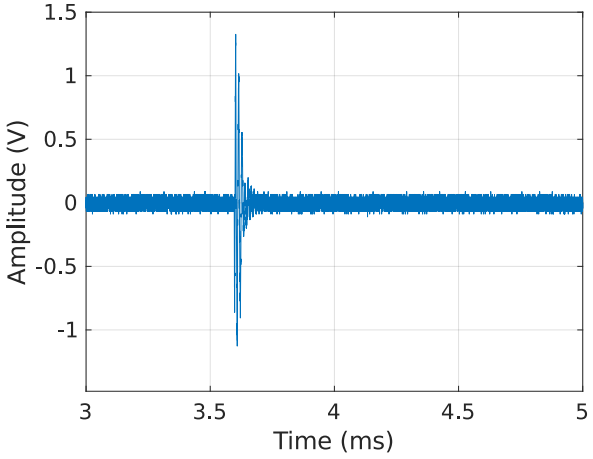

Figure 3.11.: A random impulse measured at point DDL

with m being the discrete-time index of occurrence, and its frequency spectrum is given by

$$\Phi(i) = \sum_{m=-\infty}^{\infty} \delta(m) e^{-j2\pi \frac{im}{N}} = 1, \text{ for all } i. \tag{3.5}$$

In real communication systems, impulsive noise has normally a duration longer than one sample. For example, Fig. 3.11 shows a measured impulse with duration 0.118 ms which at a sampling rate of 500 MHz results in a digital impulse composed of 59,000 samples.

3.3.2. Filter-Based Model

A very intuitive way of modeling impulsive noise is described in [36]. An impulsive noise $n_I(m)$ is described as a sequence of short duration pulses of random amplitude, duration and time of occurrence which can be modelled as the output of a filter excited by an amplitude-modulated random binary sequence as

$$n_I(m) = \sum_{k=0}^{P-1} h_k n(m-k) q(m-k), \tag{3.6}$$

where $q(m)$ is a binary-valued random sequence model of the time of occurrence of impulsive noise, $n(m)$ is a continuous-valued random process model of an impulse amplitude, and h_k is the impulse response of a filter that models the duration and shape of each impulse. The impulsive noise model of Eq. 3.6 is illustrated in Fig. 3.12. There are two popular statistical processes for modeling impulsive noise as an amplitude-

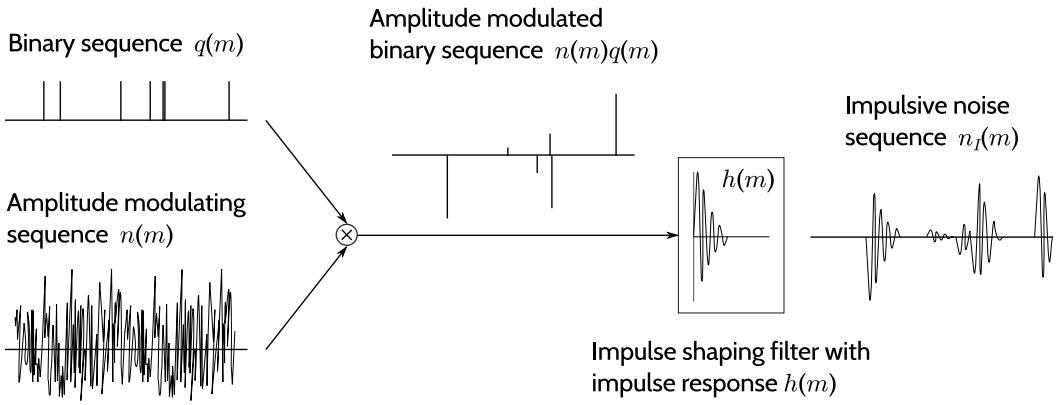

Figure 3.12.: Impulsive noise model as the output of a filter

modulated random binary sequence, $n(m)q(m)$, which are discussed next.

Bernoulli-Gaussian Model

In this model, the random time of occurrence of impulses is modeled by a binary Bernoulli process $q(m)$ [36]. That is, an impulse occurs when $q(m)$ takes a value of "1" which happens with probability α. Consequentially, $q(m)$ takes a value of "0" with probability $1-\alpha$. The probability mass function of a Bernoulli process is defined as

$$P(q(m)) = \begin{cases} \alpha, & q(m) = 1 \\ 1-\alpha, & q(m) = 0. \end{cases} \tag{3.7}$$

The process has a mean

$$\mu_b = \mathbb{E}[(q(m))] = \alpha \tag{3.8}$$

and a variance

$$\sigma_b^2 = \mathbb{E}[(q(m) - \mu_b)^2] = \alpha(1-\alpha). \tag{3.9}$$

By using a Bernoulli-Gaussian model, the amplitude of the impulses is modeled by a Gaussian process $n(m)$ and follows a Gaussian distribution $\mathcal{N}(x|0,\sigma_n^2)$ with PDF

$$f_N(n(m)) = \frac{1}{\sigma_n\sqrt{2\pi}} e^{-\frac{n^2(m)}{2\sigma_n^2}}, \tag{3.10}$$

where σ_n^2 is the variance of the noise amplitude. In a Bernoulli-Gaussian model the PDF of an impulsive noise $n_I(m)$ is given by

$$f_N^{BG}(n_I(m)) = (1-\alpha)\delta(n_I(m)) + \alpha f_N(n_I(m)) \tag{3.11}$$

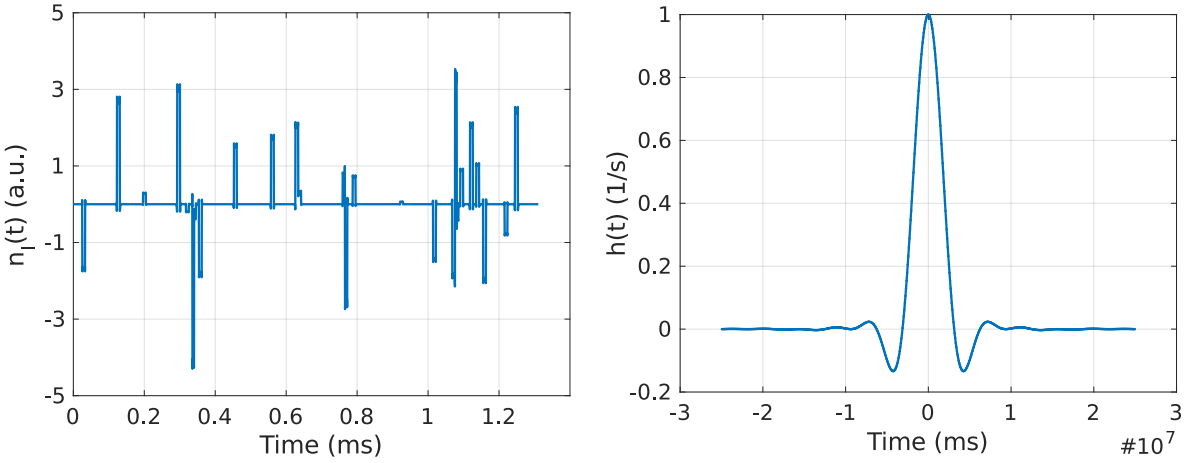

(a) Example of a time sequence (b) Impulse response $h(t)$ of the applied filter

Figure 3.13.: Bernoulli-Gaussian impulsive noise

with $\delta(n_I(m))$ being the Kronecker delta function. When $n_I(m) = 0$, i.e. no impulse is present, then $\delta(n_I(m)) = 1$ and the probability $P(q(m)) = (1 - \alpha)$ holds. From the result in Eq. 3.11 follows that $f_N^{BG}(n_I(m))$ is a mixture of a discrete probability mass function $\delta(n_I(m))$ and a continuous probability density function $f_N(n_I(m))$. An exemplary Bernoulli-Gaussian impulsive noise by applying a root raised cosine filter with a roll-off factor 0.5 is shown in Fig. 3.13a. The impulse response $h(t)$ of the filter is depicted in Fig. 3.13b.

Poisson-Gaussion Model

In the Poisson-Gaussian model, the random time of occurrence of an impulse is modeled by a Poisson process. The Poisson process is a discrete probability distribution model. It expresses the probability of a given number of events occurring in a fixed interval of time when these events occur with a known average rate and independent of the time since the last event. Let $X(t)$ be an event-counting process. Then, $X(t)$ follows a Poisson distribution $Pois(\lambda)$ with parameter $\lambda > 0$ if the probability mass function of X is given by

$$P(X = k) = \frac{(\lambda)^k}{k!} e^{-\lambda}, k > 0. \tag{3.12}$$

$P(k)$ expresses the probability of occurrence of k events in a unit interval. The Poisson process parameter λ, called the rate function, describes the average number of events

per unit interval. It further holds

$$\mathbb{E}[X(t)] = Var[X(t)] = \lambda. \tag{3.13}$$

Then, the probability that an event occurs in a small interval of time Δt is given by [36]

$$\begin{aligned} &\text{Prob(1 impulse in a small intervall } \Delta t) = \lambda \Delta t \\ &\text{Prob(0 impulse in a small intervall } \Delta t) = 1 - \lambda \Delta t. \end{aligned} \tag{3.14}$$

and the probability of k event occurrences in a time interval t can be expressed as

$$P(k,t) = \frac{(\lambda t)^k}{k!} e^{-\lambda t}. \tag{3.15}$$

The mean and variance of $X(t)$ is then

$$\mathbb{E}[X(t)] = Var[X(t)] = \lambda t. \tag{3.16}$$

In a Poisson-Gaussian model it is assumed that no more than one impulsive noise event can occur in a time interval Δt and the PDF of an impulsive noise $n_I(m)$ in this interval is given by

$$f_N^{PG}(n_I(m)) = (1 - \lambda \Delta t)\delta(n_I(m)) + \lambda \Delta t f_N(n_I(m)) \tag{3.17}$$

where $f_N(n_I(m))$ is the Gaussian PDF from Eq. 3.10. Consequently, the Poisson-Gaussian model differs from the Bernoulli-Gaussian model only in modeling the time occurrences of an event and its output is similar to that shown in Fig. 3.13a.

3.3.3. Poisson-Gaussian Burst Model

Comparing the sequences from Fig. 3.13a and 3.11 does not give an optimal match. By applying a different filter impulse response, the impulses could be shaped to better match the measured results. This section proposes another Poisson-based model. To better represent the measured noise characteristic, a Poisson process is used to model the random time of occurrence r of impulsive burst noise. The amplitude of each occurring burst b_i follows a Gaussian distribution. The corresponding standard deviations σ_i are uniformly distributed over a range $[a, b]$, while the burst durations d_i are logarithmically distributed within a range $[\hat{a}, \hat{b}]$ since shorter impulses occur more frequently than long pulses as discussed in Sec. 3.2.

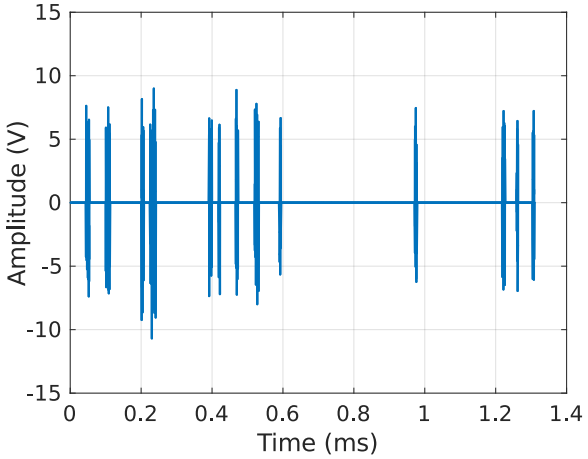

Figure 3.14.: Example of a Poisson-Gaussian Burst impulsive noise

Consequently, the Poisson-Gaussian Burst impulsive noise model resembles the Middleton's class A model. However, the resulting impulsive noise can be better adapted to a more complex noise behavior as observed in the measurements presented in Sec. 3.1. The duration of the impulses and their amplitude can be easily adapted by adjusting the span defined by $a, b, \hat{a}$ and $\hat{b}$, and the distributions d_i and σ_i obey. Fig. 3.14 depicts an impulsive noise sequence generated by the Poisson-Gaussian Burst model.

3.3.4. Middleton's Class-A Model

The Middleton's class A model is a more complex model that additionally characterizes the pulse durations and IAT [37–39]. It is a statistical physical model which includes the non-Gaussian components of natural and man-made noise. Due to the canonical nature of this model, i.e. its mathematical form is independent of the physical environment and thus the model is invariant of the noise source, noise waveform and propagation environment, it has become popular in many fields. Hence, there are extensive studies and utilizations in the literature, such as [40–46].

In [40] it is stated that the class A model does not apply for some physical conditions. That is, the canonical class A probability density function (PDF) cannot fit measured data unless 80-90 % of the values of non-Gaussian noise power are within a span of 30 dB. Thus, the quasi-canonical model with an additional correction has been proposed in [47]. However, in most cases it can be expected that the correction series has only minor effects on the results when working with the class A model [42]. For that reason, only the original canonical class A model is presented here and used later

in the simulation environment in Chapter 5.

According to [39], the amplitude PDF of the class A noise is derived as shown

$$f_X(x) = e^{-A} \sum_{m=0}^{\infty} \frac{A^m}{m!\sqrt{2\pi\sigma_m^2}} e^{-\frac{x^2}{2\sigma_m^2}}, \tag{3.18}$$

where m are the different impulsive sources and σ_m^2 is the noise variance written as

$$\sigma_m^2 = \frac{\frac{m}{A} + \Gamma'}{1 + \Gamma'}. \tag{3.19}$$

with A being the overlap index or impulsive index, defined as

$$A = v_t T_s. \tag{3.20}$$

v_t is the average number of impulsive "events" impinging on the receiver per second (mean impulse rate) and T_s is the mean impulse duration. Decreasing A means that the probability of pulses overlapping in time is small. That is, the number of impulses and/or their duration is small so that the (instantaneous) noise properties are dominated by the waveform characteristics of individual events. This way, the noise becomes more impulsive, Fig. 3.15b, and can be made arbitrarily close to a conventional Poisson process, since the model assumes that the individual impulses are Poisson distributed in time [48]. As A grows, the probability of overlapping pulses becomes larger and the noise becomes less structured, i.e. the statistics of the instantaneous amplitude approach Gaussian distribution asymptotically as $A \to \infty$, although already $A \cong 1$ is considered as a large value for A, Fig. 3.15a.

The Gaussian factor Γ' is the ratio of powers between the Gaussian and impulsive (non-Gaussian) noise components. Γ' lays between 0.001 and 1, and the closer Γ' is to 1 the more Gaussian is the noise, as it can be seen in Fig. 3.15a and 3.15d. It is defined as

$$\Gamma' = \frac{X_G^2}{X_p^2}, \tag{3.21}$$

where X_G^2 and X_p^2 is the power of the Gaussian and impulsive noise component, respectively. It further holds

$$X_X^2 = X_G^2 + X_p^2. \tag{3.22}$$

Considering above definitions, the Middleton's class A model's PDF from Eq. 3.18 can

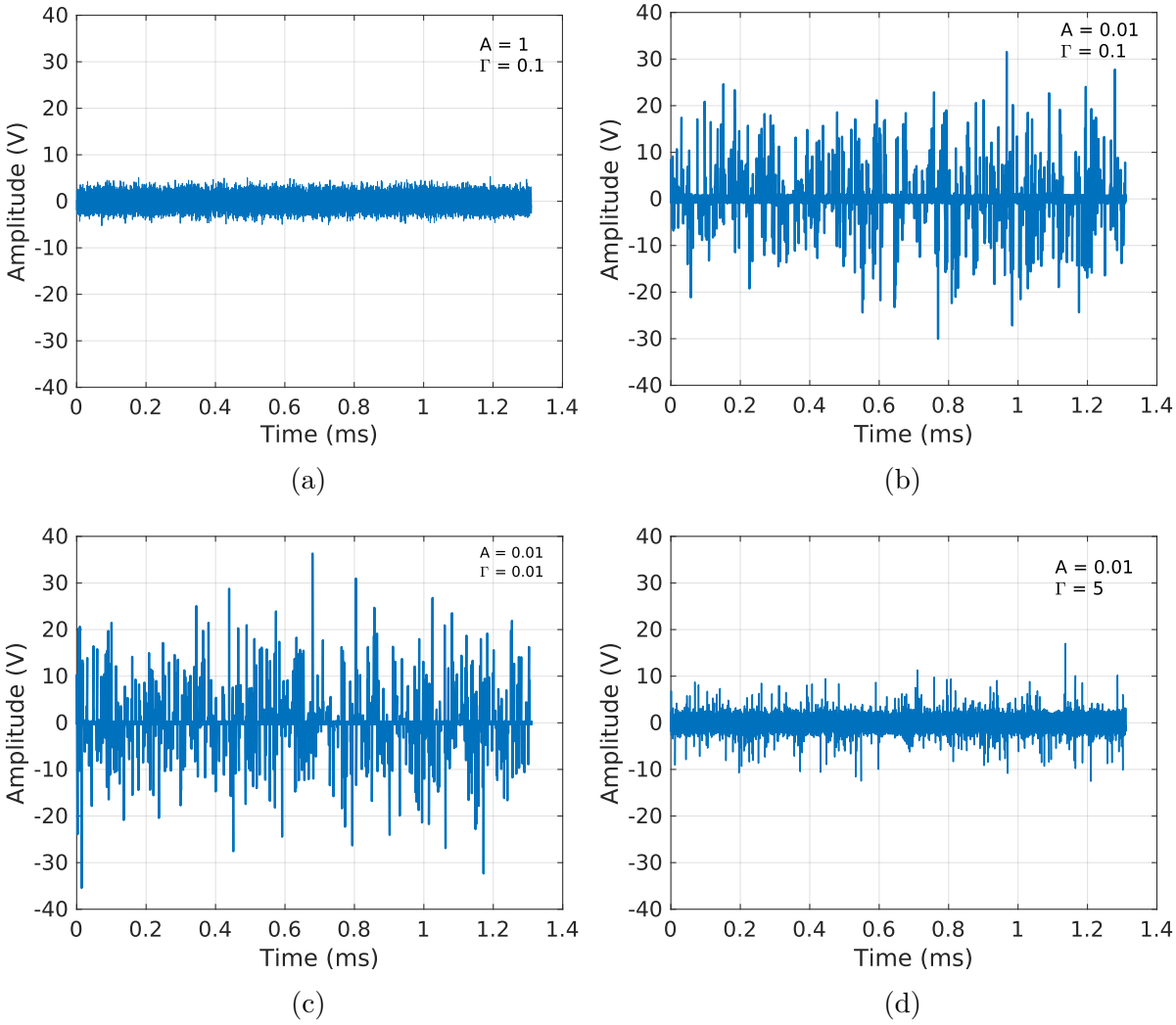

Figure 3.15.: Middleton class-A noise samples for different A and Γ'

be rewritten as

$$f_X(x) = \sum_{m=0}^{\infty} P_m \mathcal{N}(x|0, \sigma_m^2) \tag{3.23}$$

with

$$P_m = \frac{A^m e^{-A}}{m!}. \tag{3.24}$$

This way, it is easy to recognize that the PDF of a class A model is a weighted sum of Gaussian distributions with mean equal to zero and a variance σ_m^2. The factor P_m makes the terms decrease quickly as m increases. Terms beyond $m = 3$ do not contribute to the total PDF in most cases. In fact, more terms are necessary as A increases, so the series should be summed until $A^m/m!$ is smaller than the tolerable error. By a close reflection of Eq. 3.15 and 3.24, it can be recognized that both event occurrences are Poisson PDFs. In Eq. 3.15 λt is replaced by the impulsive index A. This feature reasons the assumption made earlier that for small A the class A is close to a Poisson process.

3.3.5. Symmetric Alpha Stable Model

The symmetric alpha stable (SαS) model is a generalization of a Gaussian distribution which can model phenomena of impulsive nature. In contrast to Middleton's class A model, it does not consider details like the structure of the noise waveform and source distribution. Therefore, SαS is a simpler model. The SαS amplitude distribution is described by its characteristic function

$$\phi(s) = e^{j\delta s - \gamma|s|^\alpha}, \tag{3.25}$$

where α is the characteristic exponent satisfying $0 < \alpha \leq 2$. It controls the heaviness of the tails of the density function. The tails are heavier and thus, the noise is more impulsive for low α while for a large α the distribution has a less impulsive character. δ is the location parameter and γ is the scale parameter, also known as the dispersion. The amplitude PDF $f_X(x)$ of the SαS can be expressed using the characteristic function as

$$f_X(x) = \frac{1}{2\pi} \int_{-\infty}^{\infty} \phi(s) e^{-jxs} ds. \tag{3.26}$$

The noise sequence depicted in Fig. 3.16 is an example of an impulsive noise constructed with the SαS model.

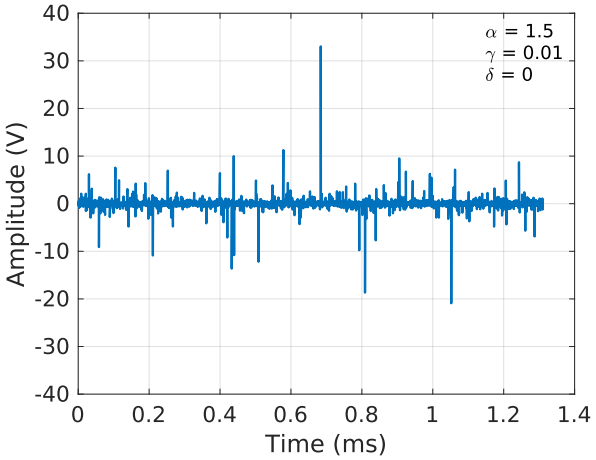

Figure 3.16.: Example of a SαS impulsive noise

3.3.6. Gaussian Mixture Model

A Gaussian mixture model (GMM) is a probabilistic model that assumes all data points are generated from a mixture of a finite number of Gaussian distributions (components) with unknown parameters. Hence, it is used to represent normally distributed subpopulations within an overall population. For that, Vastola proposed in [41] to approximate the Middleton's class A model through a mixture of Gaussian noises. This way, the GMM provides a close approximation to Middleton's class A model while being computationally more efficient.

A GMM is parameterized by the mixture component weights and the component means and variances. Its PDF is given by

$$f_X(x) = \sum_{i=1}^{k} \psi_i \mathcal{N}(x|\mu_i, \sigma_i) \tag{3.27}$$

where k is the total number of Gaussian components, μ_i and σ_i is the mean and variance of the ith component, respectively. The mixture component weights are defined as ψ_i with the constraint

$$\sum_{i=1}^{k} \psi_i = 1. \tag{3.28}$$

By observing Eq. 3.27, it stands out that the PDF is a weighted average of the PDFs of the components distributions.

Fig. 3.17a and 3.17b visualize a noise sequence generated by the Gaussian mixture model and its corresponding PDF as well as the PDFs of the contained components,

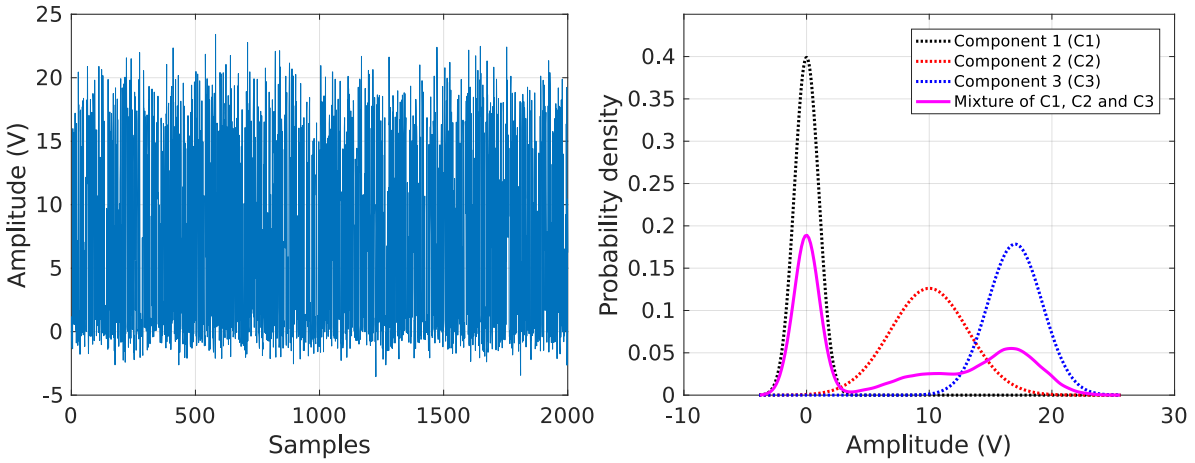

(a) Sample sequence

(b) PDF of the sample sequence

Figure 3.17.: Sample sequence and its PDF. Constructed of three Gaussian components with means $\mu_1 = 0, \mu_2 = 10, \mu_3 = 17$, variances $\sigma_1^2 = 1, \sigma_2^2 = 10, \sigma_3^2 = 5$ and occurrence probabilities of $\psi_1 = 0.5, \psi_2 = 0.2, \psi_3 = 0.3$

respectively. The depicted noise sequence is composed of three Gaussian components with means $\mu_1 = 0$, $\mu_2 = 10$ and $\mu_3 = 17$, respectively. The corresponding variances equal $\sigma_1^2 = 1$, $\sigma_2^2 = 10$ and $\sigma_3^2 = 5$. By observing the mixture PDF in Fig. 3.17b, it can be recognized that share of the single components in the mixture PDF is unequal. This is reflected by the weight parameters $\psi_1 = 0.5$, $\psi_2 = 0.2$ and $\psi_3 = 0.3$. By examining Fig. 3.17a and 3.17b, it can be concluded that due to the relativley similar weight ψ_i there is no dominant component characterizing the noise sequence. Another exemplary impulsive noise and its PDF are shown in Fig. 3.18a and 3.18b. The noise is composed by three Gaussian components with means $\mu_1 = \mu_2 = \mu_3 = 0$ and variances $\sigma_1^2 = 0.002, \sigma_2^2 = 0.7, \sigma_3^2 = 1.5$, respectively. Here, the first component is used to represent a background noise, while the second and third components indicate superimposed impulsive noise. The first component appears with the highest probability $\psi_1 = 0.998$ whereas $\psi_2 = 0.001$ and $\psi_3 = 0.001$. It can be recognized in Fig. 3.18a and 3.18b that the first component is relatively dominant. In contrast, due to the low weights of components 2 and 3, their impact on the total PDF is almost negligible as can be seen in Fig. 3.18c which shows a zoomed in area of the PDFs.

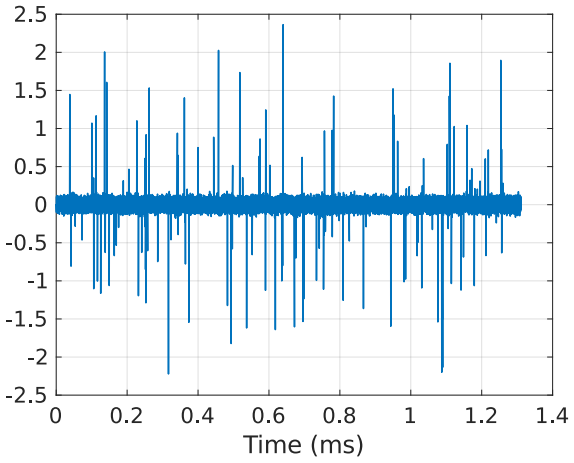

(a) Exemplary impulsive noise

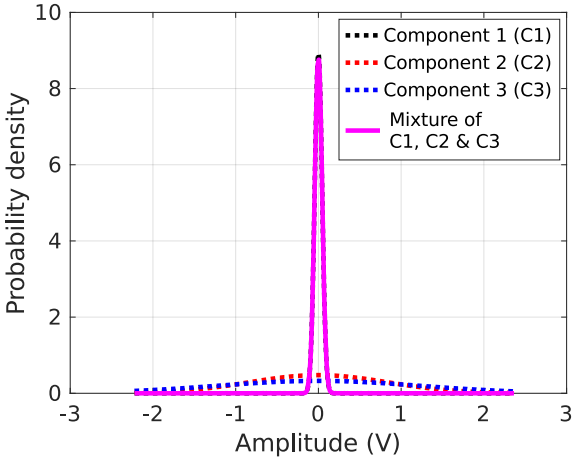

(b) PDF of the exemplary impulsive noise

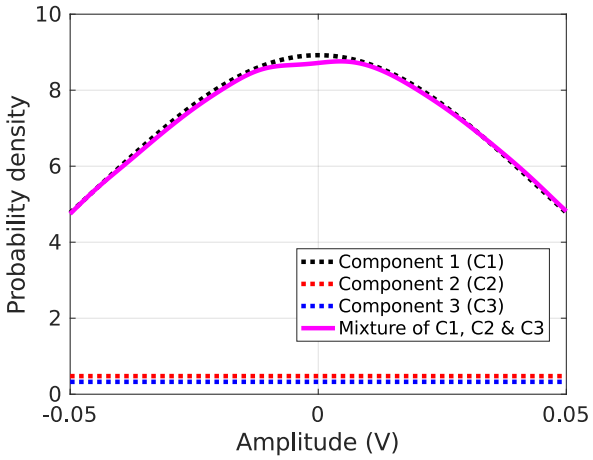

(c) Zoom of the PDFs from Fig. 3.18b

Figure 3.18.: Exemplary impulsive noise and its PDF. Built of three Gaussian components with means $\mu_1 = \mu_2 = \mu_3 = 0$, variances $\sigma_1^2 = 0.002, \sigma_2^2 = 0.7, \sigma_3^2 = 1.5$ and occurrence probabilities of $\psi_1 = 0.998, \psi_2 = 0.001, \psi_3 = 0.001$

3.4. Summary

This chapter describes the efforts put on measuring, analyzing and modeling the noise present on an automotive PLC transmission channel and presents the obtained results. Amongst all, comprehensive noise captures were performed and the obtained data was systematically analyzed. The noise was measured at six predefined access points in the test vehicle while executing 9 different actions. The impulsive and partly bursty noise behavior already observed by previous works was confirmed by the measurement results. However, due to optimized and broadband measurements, new noise characteristics could be recognized and estimated. A notable observation is, that by analyzing the power spectrum of the captured noise sequences, three obvious peak clusters, at the frequencies 33 MHz, 25 MHz and 16.7 MHz, can be clearly distinguished. Further analysis allows to conclude that the power peaks experienced at 33 MHz are most likely to be caused by impulses. Power peaks at the frequencies of 25 and 16.7 MHz could be hardly encountered within the power spectrum of the isolated impulses. Thus, it can be concluded that with high probability those are originated by the background noise. Impulses with amplitudes up to 1.3 V were experienced on the power lines, however already 90% of the impulses keep an amplitude below 96 mV.

Based on the measurement results and their evaluation, this work proposes a new classification of the non-Gaussian noise present on an automotive PLC channel. Four classes of background, periodic, random and predictable impulsive noise are suggested. The amplitude of the background noise follows a Gaussian distribution and is determined with a maximum peak amplitude of 309.4 mV. However, the 90th percentile is at already 123.8 mV and the 50th, at 22 mV. The periodic impulsive noise class is characterized by multiple pulses which arrive with a more or less constant IAT. Based on the data evaluation, it can be concluded that periodic pulses have rather short duration and IAT compared to non-periodic pulses. Random impulsive noise is defined by pulses randomly occurring in time and irrespective of past occurrences. Their amplitude spans within the measured range. While periodic and random impulsive noise is characterized by rather short duration pulses, predictable impulsive noise has a more complex structure, compound by multiple pulses and bursts. Predictable impulsive noise pulses have a much longer duration and predictable start and end points in time. It is assumed, that the knowledge of their pattern and frequency of occurrence may be used to optimize an in-vehicle PLC system performance.

The chapter is finalized by the introduction of several statistical models for modeling noise of impulsive nature. While some of the models are widely used and give

a good representation of an impulsive, non-Gaussian noise, they don't give a very good match to the noise captured by the presented measurements. Therefor, a new Poisson-Gaussian Burst model is introduced and proposed. The model allows for the specific adjustment of some of the key characteristics of the automotive non-Gaussian noise, such as the number of impulses occurring per unit time, impulse amplitude distribution as well as the impulse duration.The Poisson-Gaussian Burst model is used in simulations to evaluate the performance of an automotive PLC system, the results being presented in Chapter 5.

4

Modulation Formats

Until nowadays, Orthogonal Frequency Division Multiplexing (OFDM) was the dominating scheme used in PLC systems such as power metering or indoor networks. Also some recent works on automotive PLC architecture like [17,18] continue relying on the well-tried and established performance of OFDM. Nevertheless, OFDM is a relatively complex and power consuming technique what does not raise an issue in a conventional PLC network, as an indoor PLC, which is power unlimited with an extensive structure. On the contrary, vehicles provide a power limited environment aiming at reducing the architectural complexity. These key features are defining the driving factors of in-vehicle PLC transmission networks. In addition, the automobile industry requests for a cost effective solution which paired with efficiency in power consumption requires rethinking of the applied methods. For these reasons, the main focus in this work is on single carrier Phase Shift Keying (PSK) and Quadrature Amplitude Modulation (QAM) as relatively simple and well investigated modulation schemes. This chapter gives a basic description of the above mentioned modulation techniques and a theoretical representation of the digitally modulated signals as discussed in [49]. Additionally, a mathematical estimation of the BER is given which is used in later numerical calculations. For later performance comparison, OFDM is regarded as well.

4.1. Phase Shift Keying

Phase Shift Keying (PSK) is a well investigated and relatively straightforward modulation method which conveys data by changing the phase of a reference signal, a

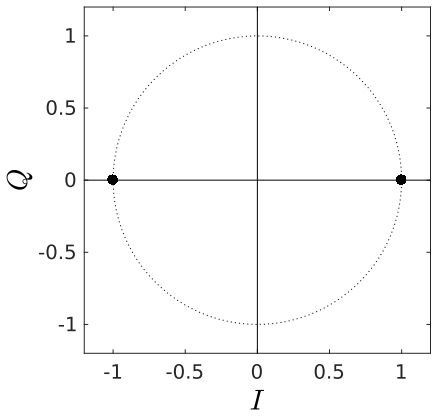

Figure 4.1.: BPSK Signal constellation diagram

so called carrier signal. This feature is of a great benefit when applying PSK in an automotive PLC system since data is encoded by the phase of the carrier signal and hence, is not sensitive to heavy amplitude fluctuations. An M-ary PSK (M-PSK) uses M phases of the carrier signal as symbols. Each of the phases encodes $\log_2(M)$ data bits. A PSK demodulator determines the phase of the received signal by comparing it to the reference signal. This work assumes that unmodulated, reference phase can be restored by the receiver, which is easy to achieve, e.g. by transmission of training symbols. This way, bit errors are caused by the interfering noise only. The numerical results for the system performance discussed in Chapter 5 are obtained for three PSK schemes, which are described in this section, namely 2-PSK or Binary Phase Shift Keying (BPSK), 4-PSK or Quadrature Phase Shift Keying (QPSK), and 8-PSK.

4.1.1. Binary Phase Shift Keying

Binary Phase Shift Keying (BPSK) is the simplest form of PSK and uses two phases, separated by 180°, to convey data. The simplicity of this scheme, resulting in low implementation costs matches well with the requirements on an in-vehicle PLC system. It can be observed from the signal constellation diagram in Fig. 4.1, that the distance between logical zeros and ones is the greatest compared to other higher order PSK schemes. This feature provides the scheme with a strong robust performance to channel impairments. The main drawback of BPSK is its large bandwidth occupation since it only modulates one bit per symbol.

A general block diagram of a BPSK transmitter is illustrated in Fig. 4.2. In BPSK, the binary input data b_n, with $b_n \in \{0; 1\}$, is encoded to a transmission sequence of

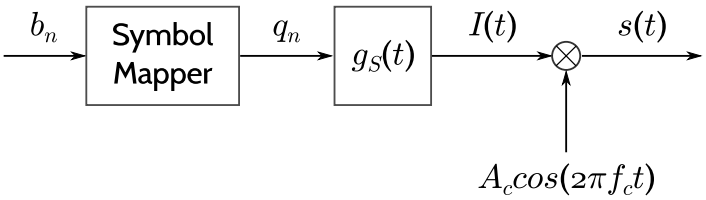

Figure 4.2.: Block diagram of a BPSK transmitter

symbols $q_n \in \{-1; 1\}$. $g_s(t)$ describes an arbitrary pulse function with pulse duration T and $I(t)$ denotes the data waveform consisting of an infinite sequence of pulses

$$I(t) = \sum_{n=-\infty}^{\infty} q_n g_s(t - nT). \tag{4.1}$$

The transmitted signal $s(t)$ is then given by

$$\begin{aligned} s(t) &= I(t) A_c \cos(2\pi f_c t) \\ &= A_c \sum_{n=-\infty}^{\infty} q_n g_s(t - nT) \cos(2\pi f_c t). \end{aligned} \tag{4.2}$$

By applying above definition, $s(t)$ can be expressed as follows

$$s(t) = \begin{cases} A_c \cos(2\pi f_c t) & \text{for } b_n = 0 \\ A_c \cos(2\pi f_c t + \pi) = -A_c \cos(2\pi f_c t) & \text{for } b_n = 1. \end{cases} \tag{4.3}$$

Bit Error Rate

The Bit error rate (BER) P_b of BPSK in an AWGN channel can be calculated as [49]

$$\begin{aligned} P_b &= Q\left(\sqrt{\frac{2E_b}{N_0}}\right) \\ &= \frac{1}{2}\text{erfc}\left(\sqrt{\frac{E_b}{N_0}}\right) \\ &= \frac{1}{2}\text{erfc}\sqrt{10^{\frac{\text{SNR [dB]}}{10}}}, \text{ with } \frac{E_b}{N_0} = SNR \end{aligned} \tag{4.4}$$

with $Q(x)$ being the probability that a single sample taken from a random process with zero-mean and unit-variance Gaussian probability density function will be greater or

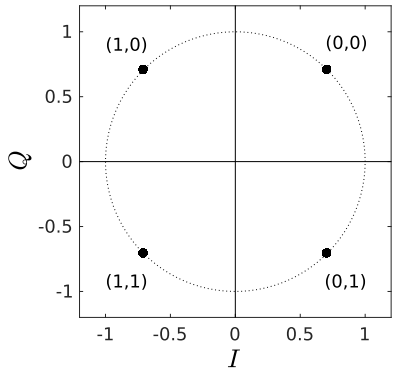

Figure 4.3.: QPSK Signal constellation diagram

equal to x and is defined as

$$Q(x) = \frac{1}{2\pi} \int_x^\infty e^{-\frac{-t^2}{2}} dt. \tag{4.5}$$

E_b is the energy per bit, $N_0/2$ is the noise power spectral density and SNR is the signal-to-noise power ratio. The complementary error function of x is defined as

$$\text{erfc}(x) = \frac{2}{\pi} \int_x^\infty e^{-t^2} dt. \tag{4.6}$$

Since only one bit is encoded per symbol, the BER corresponds to the symbol error rate (SER).

4.1.2. Quadrature Phase Shift Keying

Compared to BPSK, Quadrature Phase Shift Keying (QPSK) uses four phase shifts of $\pi/4$, $3\pi/4$, $5\pi/4$, or $7\pi/4$. This way, this modulation technique utilizes two carriers, called the in-phase and quadrature carrier, offset in phase by 90 degrees. Each of these carriers is then modulated using BPSK. As a result, in total 2 bits per symbol can be transmitted. It follows, by applying QPSK the data rate over the same channel bandwidth can be doubled. It can be observed from the constellation diagram in Fig. 4.3 that the distance between the single constellation points is smaller compared to BPSK. The QPSK modulation scheme is hence more vulnerable against noise and channel impairments.

A QPSK transmitter is depicted in Fig. 4.2. The binary data $b(t)$ arriving at rate R_b is split by a serial to parallel converter into two data streams, $b_I(t)$ and $b_Q(t)$. The following symbol mapping modules encode the bit streams into orthogonal trans-

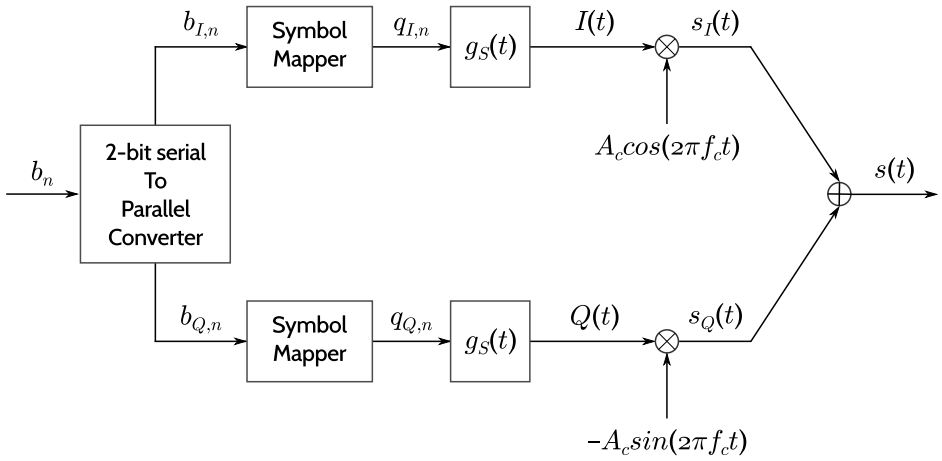

Figure 4.4.: Block diagram of a QPSK transmitter

mission symbols $q_I(t)$ and $q_Q(t)$, respectively. The mapping is based on the Gray coding to minimize the bit errors that can occur. Let $g_s(t)$ again be an arbitrary pulse function with a pulse duration T_s equal to the symbol duration. The in-phase and quadrature components $I(t)$ and $Q(t)$ represent pulse trains which modulate the carriers $A_c \cos(2\pi f_c t)$ and $-A_c \sin(2\pi f_c t)$, respectively. With

$$\begin{aligned} I(t) &= \sum_{n=-\infty}^{\infty} q_{I,n} g_s(t - nT_s) \\ Q(t) &= \sum_{n=-\infty}^{\infty} q_{Q,n} g_s(t - nT_s), \end{aligned} \tag{4.7}$$

the QPSK transmission signal $s(t)$ is defined as

$$\begin{aligned} s(t) &= I(t) A_c \cos(2\pi f_c t) - Q(t) A_c \sin(2\pi f_c t) \\ &= A_c (I(t) \cos(2\pi f_c t) - Q(t) \sin(2\pi f_c t)) \\ &= A_c \cos(2\pi f_c t + \Phi(t)). \end{aligned} \tag{4.8}$$

The phase $\Phi(t)$, of the transmitted signal is related to the data waveform as

$$\Phi(t) = \sum_{n=-\infty}^{\infty} \phi_n g_s(t - nT_s), \text{ with } \phi_n \in \{\pi/4, 3\pi/4, 5\pi/4, 7\pi/4\}. \tag{4.9}$$

The mapping of $b_{I,n}$ and $b_{Q,n}$ to ϕ_n is given in Tab. 4.1.

$b_{I,n}$	$b_{Q,n}$	ϕ_n
+1	+1	$\pi/4$
-1	+1	$3\pi/4$
-1	-1	$5\pi/4$
+1	-1	$7\pi/4$

Table 4.1.: QPSK symbol mapping

Bit Error Rate

As mentioned above, QPSK can be viewed as a modulation scheme using two orthogonal carriers on which the BPSK technique is applied. Hence, both in-phase and quadrature carriers can be independently demodulated. As a result, the BER for QPSK is the same as for BPSK, namely [49]

$$P_b = Q\left(\sqrt{\frac{2E_b}{N_0}}\right). \tag{4.10}$$

However, for achieving the same BER, QPSK utilizes twice the power as BPSK, since it transmits two bits per symbol.

The probability of a symbol error is given by

$$\begin{aligned} P_s &= 1 - (1 - P_b)^2 \\ &= 2P_b - P_b^2 \\ &= 2Q\left(\sqrt{\frac{2E_b}{N_0}}\right) - \left[Q\left(\sqrt{\frac{2E_b}{N_0}}\right)\right]^2. \end{aligned} \tag{4.11}$$

4.1.3. M-ary Phase Shift Keying

The motivation of using higher order PSK modulation is to increase the spectral efficiency by using multiple phase levels. In M-ary PSK (M-PSK), M different phase shifts of the carrier are used to convey data. The $M = 2^b$ signal waveforms, each representing b data bits, are represented as

$$s_k(t) = A_c g_s(t)\cos(2\pi f_c t + \psi_k + \phi_{off}), \quad 0 \le t \le T_s, \quad k = 1, ..., M, \tag{4.12}$$

where

$$\psi_k = \frac{2\pi(k-1)}{M} \tag{4.13}$$

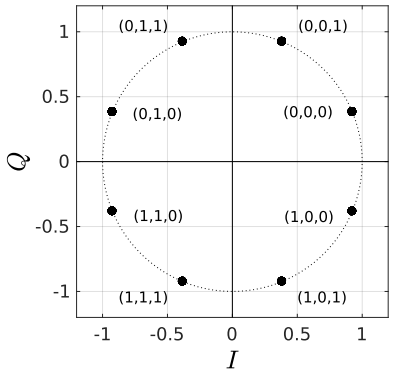

Figure 4.5.: Constellation diagram for 8-PSK with $\phi_{off} = \frac{\pi}{8}$

and indicates the M possible phase levels of the carrier, and ϕ_{off} is an arbitrary initial phase which rotates the signal constellation. Having this, the M-PSK symbols can be expressed as

$$\begin{aligned} q_{I,n} &= \cos\left(\psi_k + \phi_{off}\right) \\ q_{Q,n} &= \sin\left(\psi_k + \phi_{off}\right). \end{aligned} \tag{4.14}$$

The highest order PSK modulation scheme used for the numerical results of the system performance evaluation discussed in Chapter 5 is a 8-PSK, i.e. three information bits per symbol are transmitted. The corresponding constellation diagram and symbol mapping is shown in Fig. 4.5.

Bit Error Rate

With increasing M, the distance between neighboring constellation points decreases and hence, the BER becomes higher. Fig. 4.6 illustrates the error probability as a function of the SNR for $M = 2, 4, 8, 16$ and coherent detection on an AWGN channel. It can be observed, that the penalty in SNR increases as M takes values beyond $M = 4$. For instance, for BER $= 10^{-5}$ the difference for $M = 4$ and $M = 8$ is approximately 4 dB, while the difference between $M = 8$ and $M = 16$ accounts for 5 dB. As a rule of thumb, it can be assumed that for large $M > 16$, doubling the number of phases requires additional 6 dB to achieve the same performance [49]. An estimate of the SER for M-PSK and SNR $>> 1$ is given by

$$P_{s,M\text{-PSK}} \approx \operatorname{erfc}\left(\sqrt{k\ \mathrm{SNR}}\sin\left(\frac{\pi}{M}\right)\right) \tag{4.15}$$

with $k = \log_2 M$.

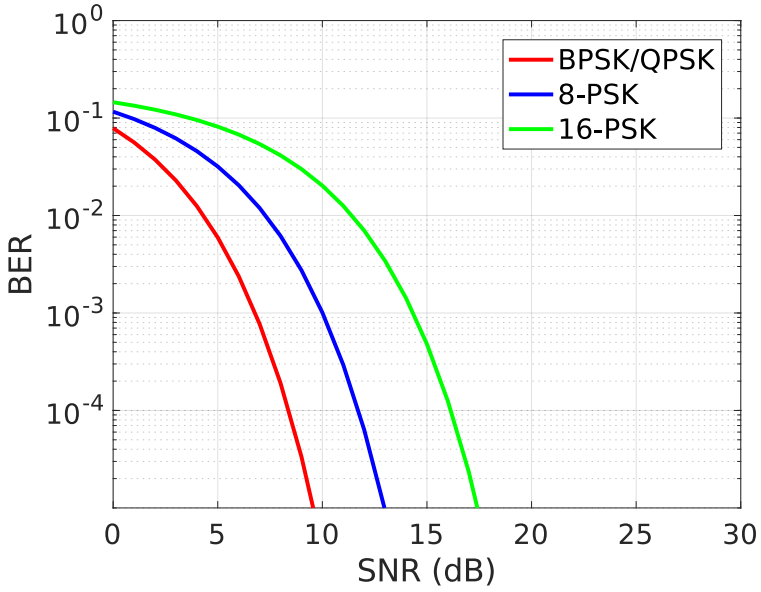

Figure 4.6.: Bit error rate for M-PSK with $M = 2, 4, 8, 16$

Assuming a Gray coded bit assignment, two k-bit symbols corresponding to neighboring signal phases differ in only one bit. As a result by the effect of noise, the erroneous selection of an adjacent phase would lead to a single bit error. Hence, the equivalent BER for an M-PSK can be well approximated by

$$P_{b,M\text{-PSK}} \approx \frac{1}{k} P_{s,M\text{-PSK}}. \tag{4.16}$$

4.2. Quadrature Amplitude Modulation

QAM offers another technique to increase the spectral efficiency by modulating the amplitude as well as the phase. Hence, it can be seen as a combination of Amplitude Shift Keying (ASK) and PSK. As a result, a more complex demodulator is needed which can correctly detect both phase and amplitude, rather than only the phase as by using a PSK scheme. This in turn, is in conflict with the simplicity goal to be complied with in the concept of an automotive PLC transmission system followed in this thesis. However, for achieving higher data rates than those offered by 8-PSK, for the same transmitted power and in a given bandwidth, it is a logical step to move to M-ary QAM (M-QAM), with $M > 8$, as it gains on distance between adjacent symbols by distributing the constellation points more evenly as shown in Fig. 4.7 on

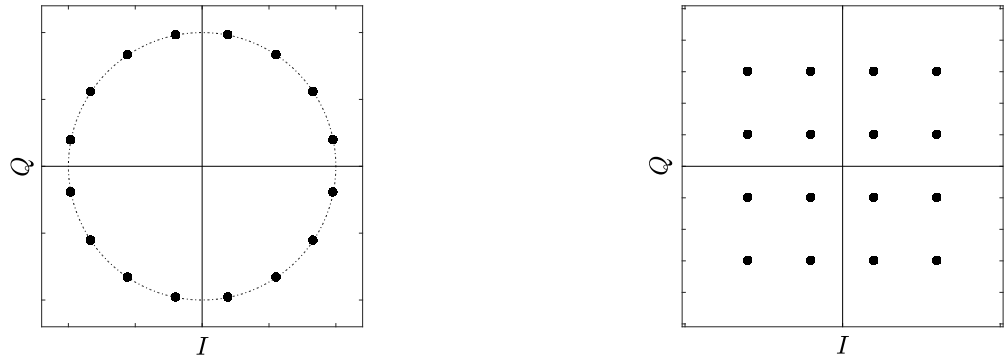

(a) 16-PSK Constellation diagram (b) 16-QAM Constellation diagram

Figure 4.7.: Phase diagrams of 16-PSK and 16-QAM

the example of 16-PSK and 16-QAM. Fig. 4.7b illustrates the constellation diagram of a 16-QAM used for obtaining part of the numerical results in Chapter 5. In this thesis only a rectangular 16-QAM is considered.

The corresponding QAM signal waveforms are expressed by

$$\begin{aligned} s(t) &= I(t)A_c\cos(2\pi f_c t) - Q(t)A_c\sin(2\pi f_c t) \\ &= q_I(t)g_s(t)A_c\cos(2\pi f_c t) - q_Q(t)g_s(t)A_c\sin(2\pi f_c t), \end{aligned} \tag{4.17}$$

where $q_I(t)$ is the information conveyed by the cosine of the carrier (in-phase), $q_Q(t)$ is the information conveyed by the sine of the carrier (quadrature) and $g_s(t)$ is a pulse function, shaping the spectrum of the transmitted signal.

Bit Error Rate

The BER of QAM very much depends on the bits to symbol mapping. The SER $P_{s,M\text{-QAM}}$ for a rectangular signal constellation can be approximated as [49]

$$\begin{aligned} P_{s,M\text{-QAM}} \approx & 2\left(1-\frac{1}{\sqrt{M}}\right)\operatorname{erfc}\left(\sqrt{\frac{3}{2(M-1)}}k\ \mathrm{SNR}\right) \\ & \times\left[1-\frac{1}{2}\left(1-\frac{1}{\sqrt{M}}\right)\operatorname{erfc}\left(\sqrt{\frac{3}{2(M-1)}}k\ \mathrm{SNR}\right)\right] \end{aligned} \tag{4.18}$$

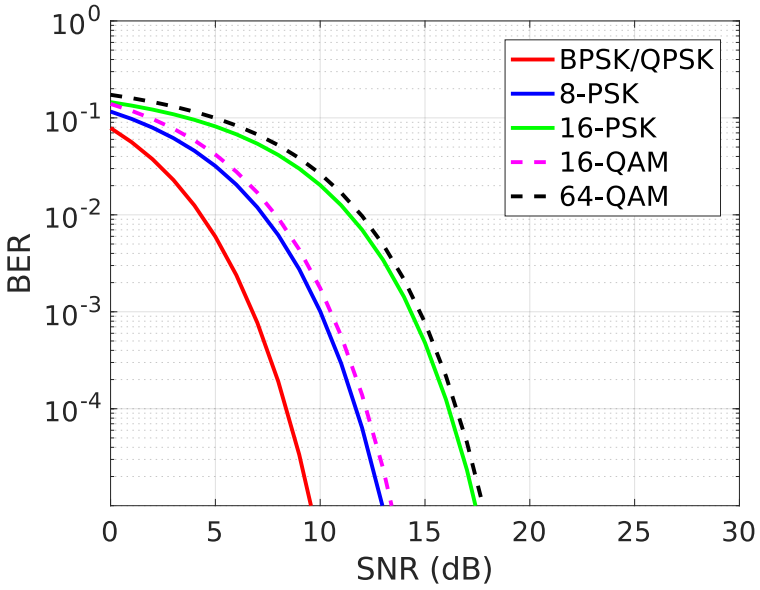

Figure 4.8.: Probability of a bit error for M-PSK and M-QAM

with $k = \log_2 M$. In this case a rectangular decision region can be employed around each constellation point and hence, a tight upper bound for the SER can be given by

$$P_{s,M\text{-QAM}} \leq 2\text{erfc}\left(\sqrt{\frac{3}{2(M-1)}k\ \text{SNR}}\right). \tag{4.19}$$

Again, by assuming Gray encoding and that errors are only caused by confusion with nearest neighbors (which is a good assumption at moderate to high SNR values), a symbol error causes only one bit error and the bit error probability $P_{b,M\text{-QAM}}$ can be approximated by [50]

$$P_{b,M\text{-QAM}} \approx \frac{1}{\log_2 M} P_{s,M\text{-QAM}}. \tag{4.20}$$

Fig. 4.8 depicts the bit error probability performance of M- QAM for $M = 16$ and 64 in an AWGN channel. For a comparison purpose, the BER performance of M-PSK for $M = 8$ and 16 is illustrated as well. It can be observed that the larger distance between neighboring symbols obtained with QAM has a great impact on the BER performance. For the probability of a bit error of 10^{-5} 16-PSK shows 4 dB of penalty on SNR compared to 16-QAM. It further can be noticed that the performance of 64-QAM is very close to the one of 16-PSK, however it is able of transmitting 6 bits per symbol instead of 4.

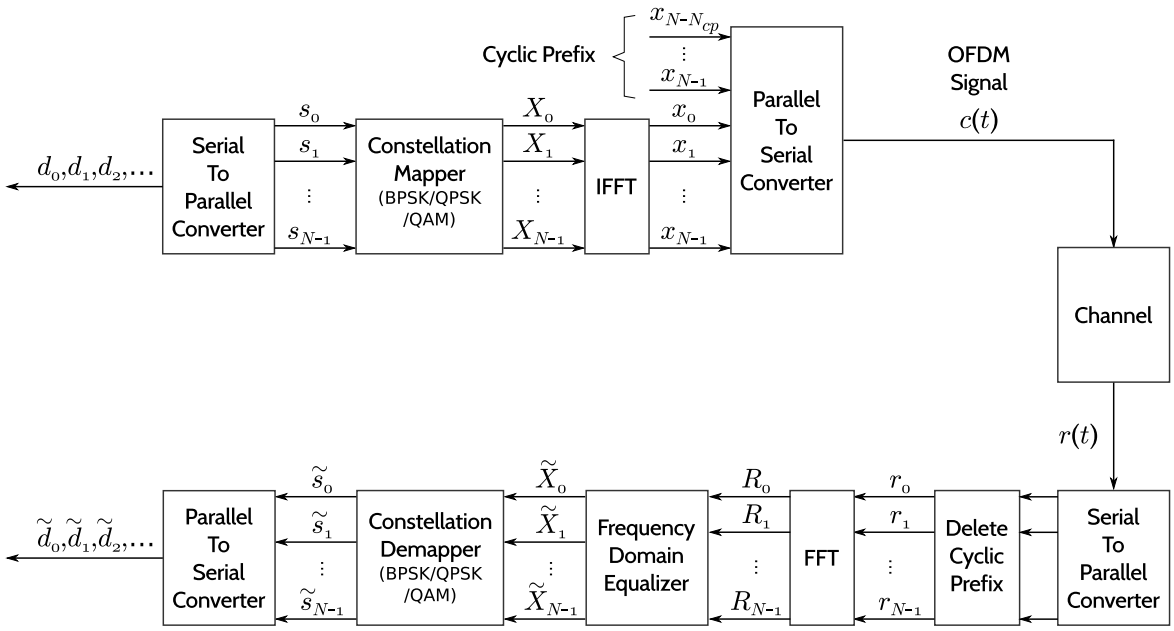

Figure 4.9.: OFDM communication system basic architecture

4.3. Orthogonal Frequency Division Multiplexing

OFDM is a multi-carrier multiplexing scheme, which modulates the source information onto several carriers, called subcarriers, within the allocated bandwidth. Splitting the source data into multiple data streams, mapped to the different carriers, results in multiple lower rate data streams which may have different bit rates. The subcarriers are centered at frequencies that are orthogonal to each other and each of them employs a single carrier modulation technique like BPSK, QPSK, QAM, etc. It needs to be noted, that subcarriers may carry different modulation schemes. By doing so, OFDM transforms the entire allocated channel bandwidth into small channels as used by the individual subcarriers. This way, by introducing small flat fading channels, which are more easier to handle with, it overcomes the effect of frequency selective fading. As a result, OFDM has a good performance on communication channels with frequency selective fading and has become a standard system applied in PLC systems as defined in the standards HomePlug AV2 [51] and HomePlug Green PHY [52]. The major disadvantage of OFDM, when it comes to its applicability in an automotive PLC system which is a power and resource limited system, is its implementation complexity and higher computational resource usage.

A basic OFDM system architecture is depicted in Fig. 4.9. First, a serial-to-parallel converter is fed with the digital input data stream and outputs parallel sequences

$s_0, ..., s_{N-1}$, where N is the number of orthogonal subcarriers. Not all subcarriers need to convey data and some can be left unused to act as guard bands or another can be reserved for pilot carriers used e.g. for channel estimation. The parallel streams $s_n, n = 0, ..., N-1$ in turn are individually translated into the corresponding modulation format applied on the single subcarriers (BPSK, QPSK, etc.). The resulting sequences $X_0, ..., X_{N-1}$ are input to an IFFT process (Inverse Fast Fourier Transform) which outputs

$$x_k = \sum_{n=0}^{N-1} X_n cos(\frac{2\pi kn}{N}) + j \sum_{n=0}^{N-1} X_n sin(\frac{2\pi kn}{N}), \quad k = 0, ..., N-1. \tag{4.21}$$

In this step, the IFFT is computed on each set of symbols, producing an output of complex time-domain samples.

Additionally, a cyclic prefix can be implemented to mitigate the problem of Inter Symbol Interference (ISI) and Inter Carrier Interference (ICI) on a non-ideal channel that causes delay dispersion. Following above example, a single OFDM symbol consists of the values

$$x_0, x_1, x_2, ..., x_{N-1}. \tag{4.22}$$

A cyclic prefix of length N_{cp} with $N_{cp} < N$ is generated by copying the last N_{cp} values from the OFDM symbol and adding them at the beginning of the same symbol. This process is illustrated in Fig. 4.10. The number of samples allocated for a cyclic prefix can be calculated as

$$N_{cp} = \frac{T_{cp} N}{T}, \tag{4.23}$$

where N is the FFT/IFFT size, T is the FFT/IFFT period or the duration of an OFDM symbol and T_{cp} is the duration of the cyclic prefix. Hence, the total duration of an OFDM symbol becomes $T + T_{cp}$. Using a cyclic prefix, the received signal $r(t)$ is given by

$$r(t) = h(t) \circledast x(t) \tag{4.24}$$

with $h(t)$ and $x(t)$ being the channel impulse response and the OFDM symbol, respectively. The circular convolution in time domain corresponds to multiplication in frequency domain

$$R = HX \tag{4.25}$$

which is used at the receiver in the Frequency Domain Equalizer (FDE) module. Since the output of the FFT is in the frequency domain, the FDE equalizes the transmitted

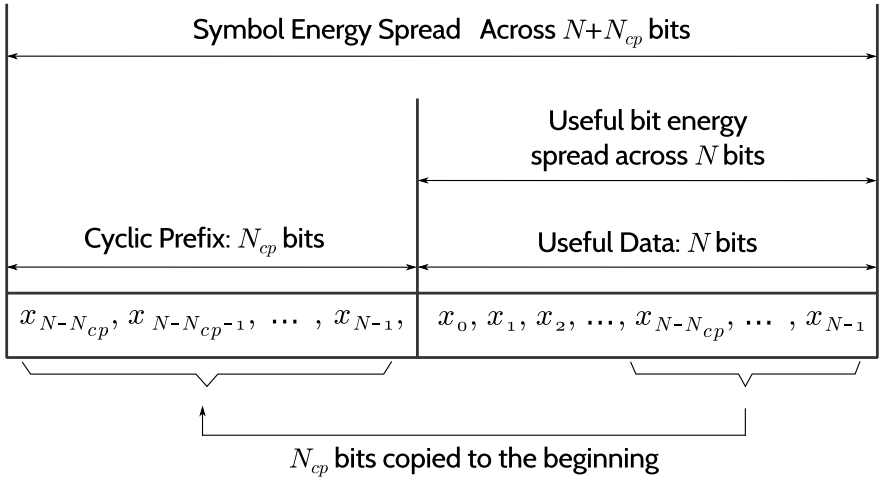

Figure 4.10.: OFDM communication system basic architecture

signal by performing the simple equalization equation

$$\hat{X} = \frac{R}{H}. \tag{4.26}$$

Bit error rate

In an AWGN channel the BER performance of OFDM is approximately equal to the performance of the underlying modulation scheme applied on the subcarriers, since the effect of the cyclic prefix on the performance in an AWGN can be neglected.

4.4. Summary

In this chapter, the single carrier modulation formats M-PSK and M-QAM as well as the multi-carrier system OFDM are described. An analytical signal definition is given and the signal constellation is illustrated by phase diagrams. Further, the applicability of the different techniques in an automotive PLC transmission system is discussed. Certainly, BPSK is the simplest scheme and is most robust to noise and channel impairments, but at the cost of large bandwidth occupation. With increasing number of points in signal space M the channel bandwidth usage becomes more efficient however, the distance between adjacent symbols decreases, which results in a higher BER. In order to illustrate the effect of M on the BER, the performance of M-PSK and M-QAM with respect to the bit error probability in an AWGN channel is depicted.

5

Performance Evaluation of an Automotive PLC Transmission System

The main limitations of an automotive PLC transmission system are the specific channel behavior featuring high attenuation and a frequency-selective transfer function caused by multipath propagation due to reflection signals, and the impulsive noise induced by numerous electronic sources. Indoor PLC is also experiencing these limitations, although with a different characteristic and intensity, the majority of which is solved in the HomePlug AV2 standard [51] by applying OFDM multiplexing scheme using 4096-QAM and turbo convolutional encoding, supporting code rates up to 16/18. The overall requirements of an in-vehicle PLC system heavily differ from those of an indoor system architecture and hence, demand for a specific and customized solution. To handle the challenges of automotive PLC transmission, [16] proposes to use redundant transmission channels with a three-level redundancy targeting the Local Interconnect Network (LIN) protocol which is used to support low rate data transmission. The redundant channels are chosen such that the deep notches in the electromagnetic compatibility (EMC) emission requirements, in the frequency range of 2-30 MHz, are avoided. As a result, the identified frequency band of 22-30 MHz is divided into two groups of 30 100 KHz narrowband channels with adjacent channel separation of 100 KHz. Four out of the 60 channels are assigned to a single transmission link. Gaussian-Minimum-Shift-Keying (GMSK) is used as a modulation scheme which uses Gaussian pulse shaping at the baseband. This way, the sudden frequency variations over time are smoothed and subsequently the spectral side-lobe level is reduced. In

the results, it is shown that redundancy serves its purpose of utilizing the available spectrum efficiently and avoiding deep notches in the EMC emission requirements. The achieved data rate accounts for 20 kbps which corresponds to the supported rate in the LIN specification 2.2. The idea of redundancy in PLC transmission systems is already known from the HomePlug ROBO (Robust OFDM) mode [52] which is used to support low rate and high reliability data transmission by transmitting the information redundantly on multiple subcarriers. Another OFDM-based solution is presented in [17] which proposes an LDPC coded OFDM relying on index modulation (OFDM-IM) to combat the frequency selectivity of the PL channel and mitigate the superposing impulsive noise. The measurement results of [53] and [54] are used for modeling the in-vehicle PLC channel for characterizing the background and impulsive noise, respectively. The BER is evaluated to estimate the performance of the suggested scheme for an irregular LDPC code with rate 1/2 and 256 subcarriers using QPSK modulation, operating in the 2-76.8 MHz frequency range. The frequency of the impulsive noise is chosen to be 25 MHz with a constant IAT between subsequent pulses of 30 ms and a pulse duration of 10 µs. The BER simulation was performed for a single direct transmission link between the right front light and the left front light from the measurements of [53] and evaluated for a system with and without impulsive noise. The multivariate Gaussian distribution is chosen to model the effect of impulsive noise. Another recent work on the performance evaluation of an in-vehicle PLC transmission system, [18], also proposes an OFDM-based scheme using QPSK modulation for the subcarriers and a forward error correction (FEC) realized by a convolutional code with rate 1/2, 2/3 or 3/4. The suggested scheme proposes the use of contact-less PLC based on magnetic field resonant technique. The PLC network topology considered in the BER evaluation consists of a single ECU, a 5 m long unshielded twisted pair cable and 8 couplers/sensors. The channel model used for the simulations is based on the measurement results of 1 m cable. In the performed simulations, the distance from the ECU to the first sensor and between two subsequent sensors is randomly chosen from 0.1 m to 0.6 m. The used frequency band is 200-300 MHz and the achieved data rate is 12 Mbps for a code rate 1/2.

This chapter aims at summarizing the efforts put on evaluating the performance of a complete in-vehicle PLC transmission system. The goal is to generate a close as possible to reality simulation scenario based on the extensive channel and noise measurements discussed in Chapter 2 and 3. The theory of the applied channel and noise models is given in Section 2.1 and 3.3, respectively. Compared to the above mentioned related works, the network topology used in the simulations presented in

this chapter consists not only of a single link or an isolated part of a PL network but represents a complete automotive power line network including PLs, ECUs and the car battery. Further, the comprised noise implies all characteristics and dynamic behavior observed in the measurements presented in Section 3.1. The consideration of many automotive power line network components as well as a broad spectrum of noise parameters allows for a more realistic estimate of an in-vehicle PLC system performance. Different modulation and noise mitigation schemes are applied and compared to each other. The bit error rate (BER) is used as a system performance indicator. The main goal was to build a system which is as simple as possible and still meets the requirements for high data rates and transmission quality in terms of a low BER. The existing automotive data transmission concept is mostly determined by low cost communication solutions like LIN and CAN. Regarding PLC as their replacement, it is important to still satisfy this high priority requirement which is a main driving factor in the automobile industry. Thus, the main motivation behind the simple design of the investigated system presented in this chapter, is preserving the low cost and easy implementation of the in-vehicle communication system.

5.1. Simulation Setup

The main building blocks, present in each simulation setup, are illustrated in Fig. 5.1 (a full list of abbreviations is given in Appendix B). The modulation schemes used for comparison of the BER system performance are BPSK, QPSK, 8-PSK, 16-PSK and 16-QAM. A matched filter is used to maximize the SNR at the receiver. The implementation is done with a Root Raised Cosine (RRC) filter with a roll-off factor of 0.5 at the transmitter and receiver. The underlying in-vehicle PL network used for the data transmission is depicted in Fig. 5.2. It has a source impedance of 50 Ω. 36 ECUs, including transmitter and receiver ECU, are connected by power lines with a cross section of 0.35mm^2. The ECUs are represented by 50 Ω (cf. 2.3.3). The line lengths are random and logarithmically distributed between 0.5 m and 10 m. The modeled PLs are partitioned into small sections of 0.1 m and each section is applied a random distance to the car body. The minimum distance of a cable to the car body (ground) accounts for 0.01 m. The varying distance and cable cross section are included by the characteristic impedance Z_C in the calculation of the chain matrix.

The 36 ECUs are connected to either the front or rear power distribution (FPD or RPD). The exact allocation of an ECU to a power distribution is negligible for the simulation results due to the cascading of matrices (see Section 2.1.1). The transmitter

From	To	Length (m)	Cross section (mm^2)
ECU	all	random	0.35
FPD	BPD	5.6	25
Battery	BPD	0.5	25
RPD	BPD	1.8	16

Table 5.1.: Power lines lengths and cross sections used in the simulated automotive PLC system

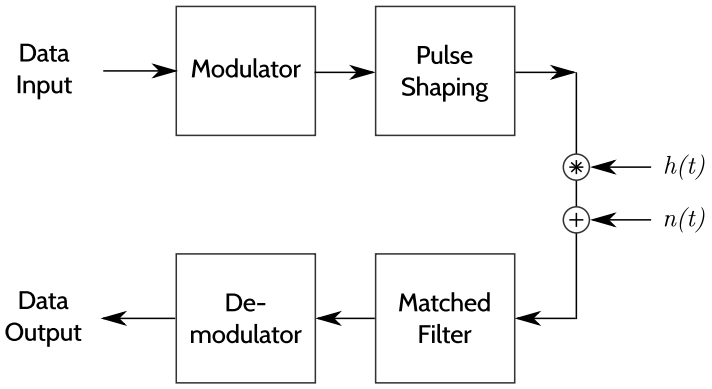

Figure 5.1.: Main building blocks of the simulated automotive PLC system

and receiver ECUs are on purpose chosen to be in the rear and front of the vehicle. This way, the transmission path includes the highly attenuating and distorting network domain including the car battery and power distributions. The length and cross section data of all power lines is given in Table 5.1. The parameters ε, μ and σ used in Eq. 2.29–2.32, for calculating the per-unit line parameters, hold the values 3.5 [F/m], 0.9999936 [H/m] and $59.1 \cdot 10^6$ [S/m], respectively and represent a typical copper cable. The relative permittivity ε is chosen for a typical low voltage cable with PVC insulation, μ is the permeability of copper and σ corresponds to the specific conductance of copper.

A baseband modulation at a carrier frequency of 25 MHz is performed which has been chosen based on the characteristics of the transmission channel. As discussed in

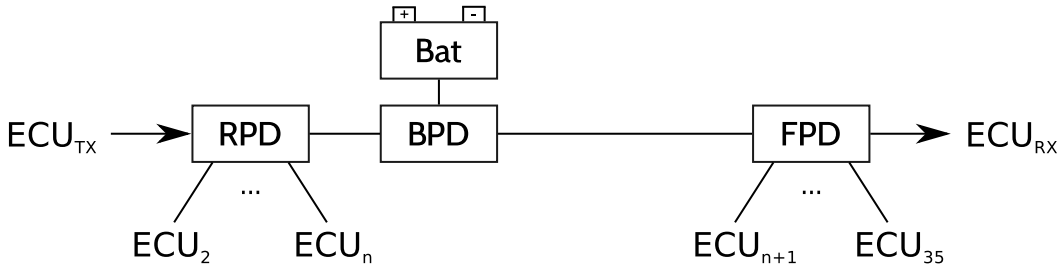

Figure 5.2.: Simulated power line topology

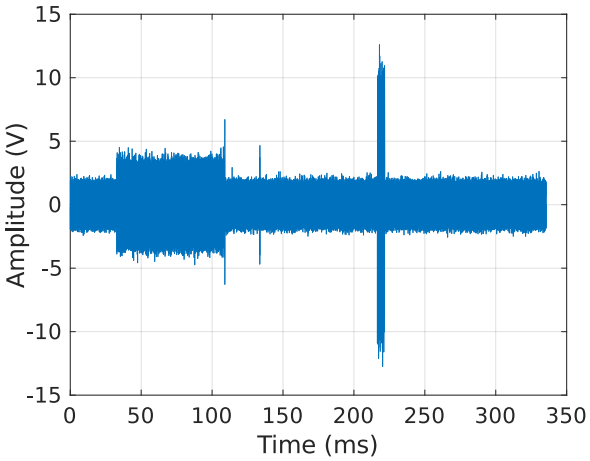

Figure 5.3.: Exemplary noise sequence used in the performance evaluation simulations

Section 2.2, the in-vehicle PLC channel offers on average the lowest attenuation in the frequency range around 25 MHz. For obtaining the numerical results, it is assumed that phase distortion can be perfectly compensated.

In Chapter 3 different models for non-Gaussian noise are presented and discussed. The simulation results given in the following sections are obtained by applying the Poisson Gaussian Burst model, described in Sec. 3.3.3. It allows for a flexible definition of an impulse amplitude, a mean occurrence rate of events (i.e. impulses) per unit time and a pulse duration. Hence, it provides the possibility for customizing the major noise parameters impulse amplitude, impulse duration, IAT of impulses and their occurrence distribution in time, as observed by the measurement results discussed in Sec. 3.1 and 3.2. Unless noted otherwise, following parameter values were used for

- the mean occurrence rate $\lambda = 15$,
- the minimum impulse duration $\hat{a} = 8$ µs,
- the maximum impulse duration $\hat{b} = 400$ ms and
- the range of standard deviation for the single impulses $\sigma = [1; 10]$.

Background noise is considered in every simulation scenario. An example of the applied noise is given in Fig. 5.3.

5.2. Simulation results

The ongoing numerical results represent the Bit Error Rate (BER) over the Signal-To-Noise (SNR) ratio. The SNR is given as E_b/N_0. The reference simulation results are obtained for the setup shown in Fig. 5.1. The BER is evaluated for data rates of 6.25 Mbps, 10 Mbps and 20 Mbps, and depicted in Fig. 5.4. The ideal BER for the corresponding modulation schemes can be found in Fig. 4.8. As expected, the performance results for higher data rates is slightly worse than for lower data rates. For 20 Mbps, BPSK, QPSK and 8-PSK experience a BER saturation for SNR values above 20 dB. This behavior mirrors the effect of the impulsive noise.

5.2.1. Performance Evaluation with Convolutional Coding

In this section, the effect of convolutional coding is presented. Convolutional codes are relatively easy to implement and have a rather good correcting capability which reasons the wide field of their application. The extended simulation setup is shown in Fig. 5.5. In the first scenario, Fig. 5.6a, 5.6c, 5.6e, the source data sequence is processed by the encoder which applies a binary convolutional code with constraint length 3, feedback taps located at the octal numbers 7 (binary 111) and 5 (binary 101) and traceback length of 15. Consequently, the coding rate is 1/2. The constraint length indicates the number of bits stored in each shift register, including the current input bits. In the second scenario, Fig. 5.6b, 5.6d, 5.6f, a rate 2/3 convolutional code is applied with constraint lengths 5 and 4. The generator polynomials in octal form given as a matrix are (23, 35, 0; 0, 5, 13). The matrix elements are to be interpreted in such a way that the element in the ith row and jth column indicates how the ith input contributes to the jth output. On the receiver side, the Viterbi algorithm is used as a well known maximum-likelihood algorithm for decoding convolutional codes. For decoding, a soft decision is used.

Although, a convolutional code has relatively good correcting capabilities, it does not perform very well in the presence of burst errors. This explains the results depicted in Fig. 5.6. One would expect significantly better results for the coded scenario compared to the uncoded. A slight improvement can be recognized in the case of 8-PSK and 16-PSK for convolutional coding with rate 1/2. However, the results for coded QPSK and 16-QAM are even slightly worse than uncoded. This can be explained by the strongly varying amplitude of the impulsive, non-Gaussian noise. The positive effect of coding can be indeed observed for higher data rates. For 20 Mbps, Fig. 5.6e, an improvement is given for all modulation formats except for 16-QAM. This might be

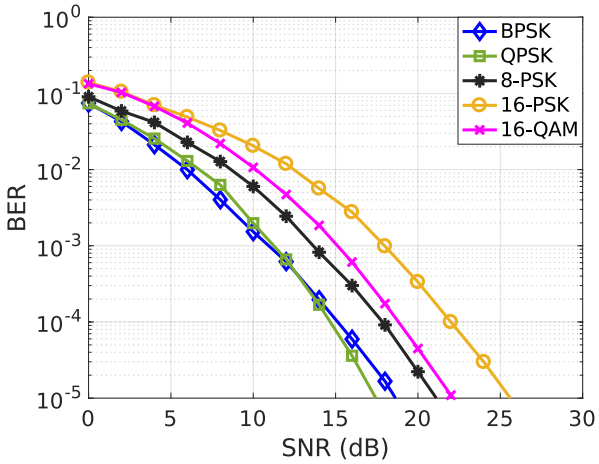

(a) BER for 6.25 Mbps

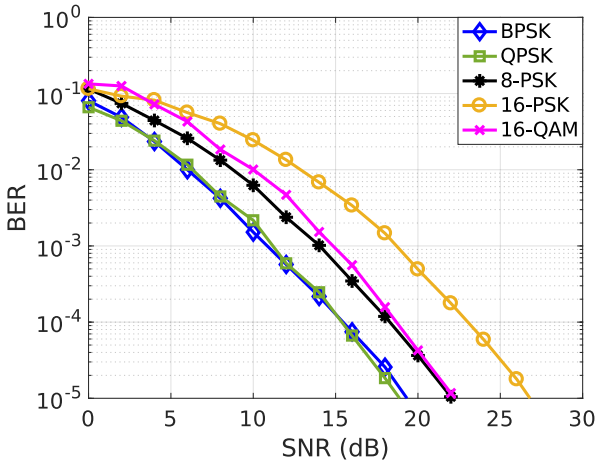

(b) BER for 10 Mbps

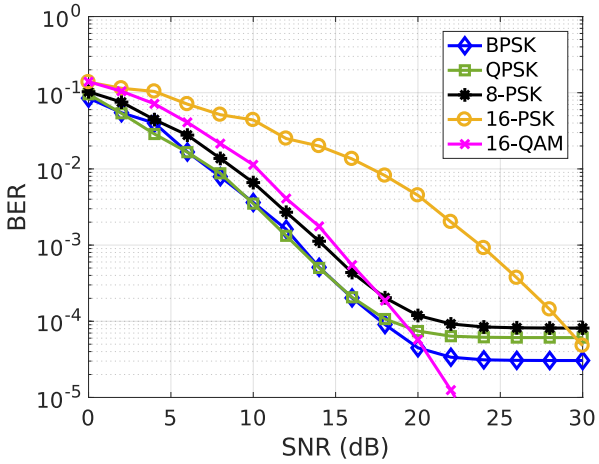

(c) BER for 20 Mbps

Figure 5.4.: Numerical results for the setup shown in Fig. 5.1

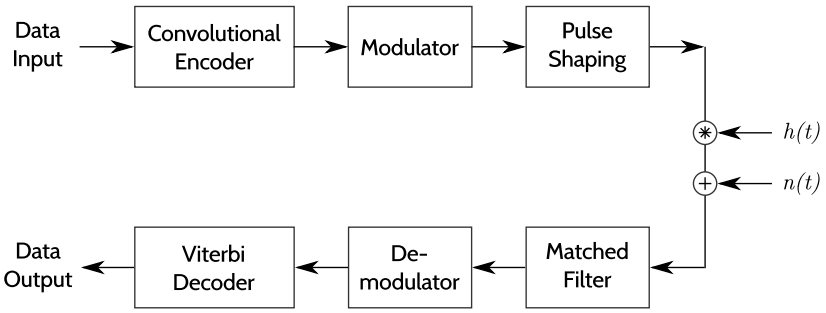

Figure 5.5.: Extended simulation setup by convolutional coding

a consequence of its higher amplitude sensitivity compared to the other modulation schemes. A particularly positive effect of convolutional coding at higher data rates is the elimination of the BER floor for BPSK, QPSK and 8-PSK. It further needs to be noted that the results are only given up to BER of 10^{-5}. It can be concluded that by using a 16-QAM modulation, the application of a convolutional coding with rate 1/2 is not necessary for SNR below 25 dB.

As expected, the rate 2/3 code does not give as much improvement as the rate 1/2 code. However, for data rate of 20 Mbps again the BER floor could be removed. Further it can be observed, that the corresponding SNR values for which the uncoded curves cross the coded ones is notably higher than for the 1/2 rate code. The SNR penalty becomes greater with increasing data rate. However, by applying a higher rate code, the effective data rate can be reduced. In this scenario, the use of coding is only useful for high SNR beyond 20-25 dB. As later discussed in Chap. 6 a usual SNR value of operation in an automotive environment is around 7-10 dB. In this case, the use of convolutional coding does not improve the system performance.

5.2.2. Performance Evaluation with Interleaving

Interleaving is a well known and approved burst error avoiding method. By its application, codes, correcting independent errors, can be converted to burst error correcting codes. Interleaving itself, causes bit sequences to be shuffled. This way, long sequences of '0's and '1's can be avoided as well as long error sequences, i.e. bursts, can be spread over a longer interval. Thus, originally adjacent bits become non-adjacent. The simulation setup including the interleaver is shown in Fig. 5.7. The encoded data sequence is processed by a block interleaver which performs two permutation steps described by [55]

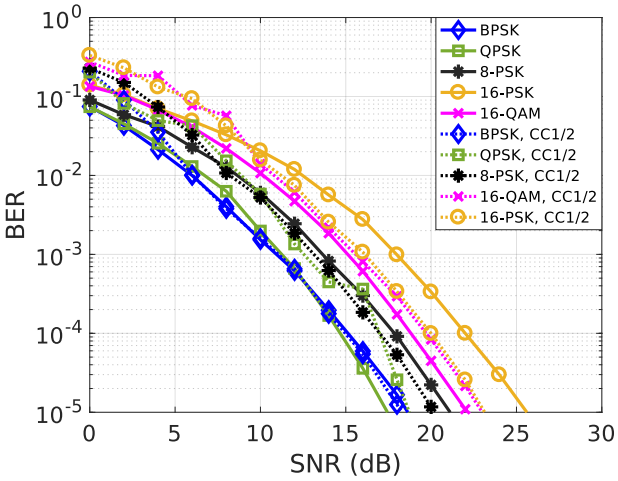

(a) BER for 6.25 Mbps

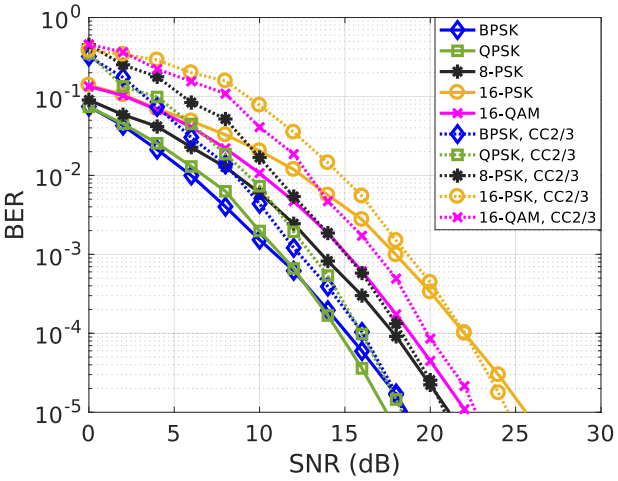

(b) BER for 6.25 Mbps

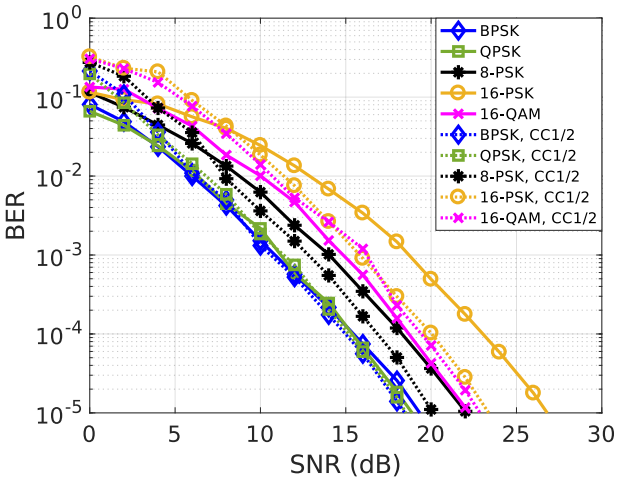

(c) BER for 10 Mbps

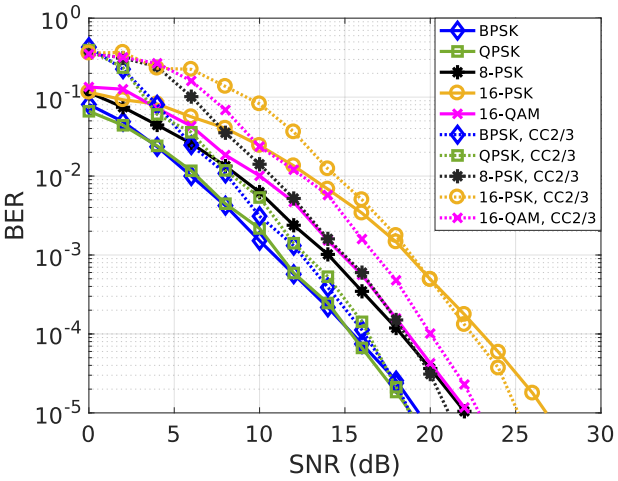

(d) BER for 10 Mbps

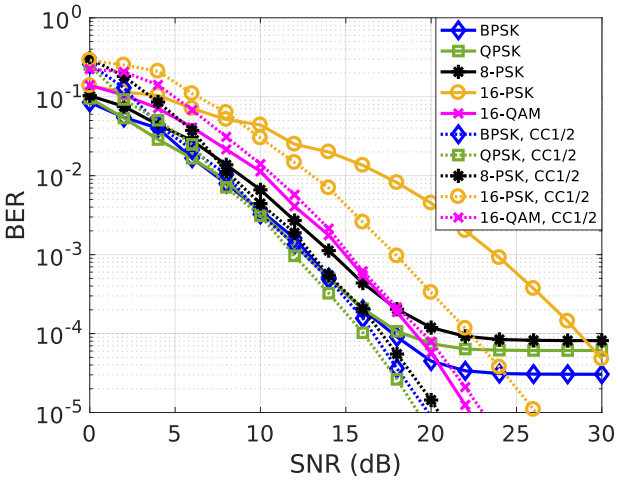

(e) BER for 20 Mbps

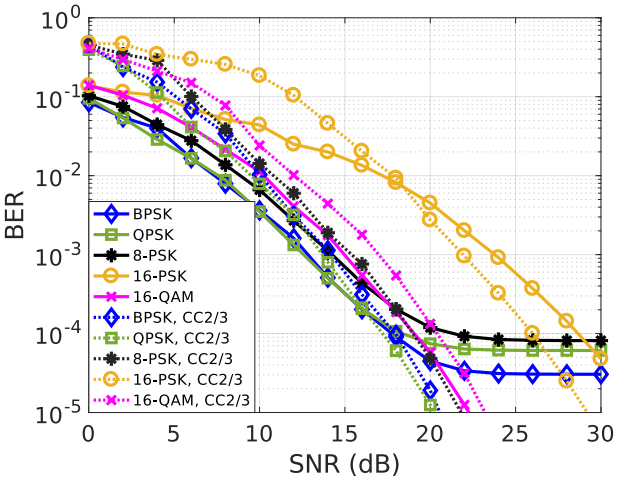

(f) BER for 20 Mbps

Figure 5.6.: Numerical results obtained for the setup from Fig. 5.5

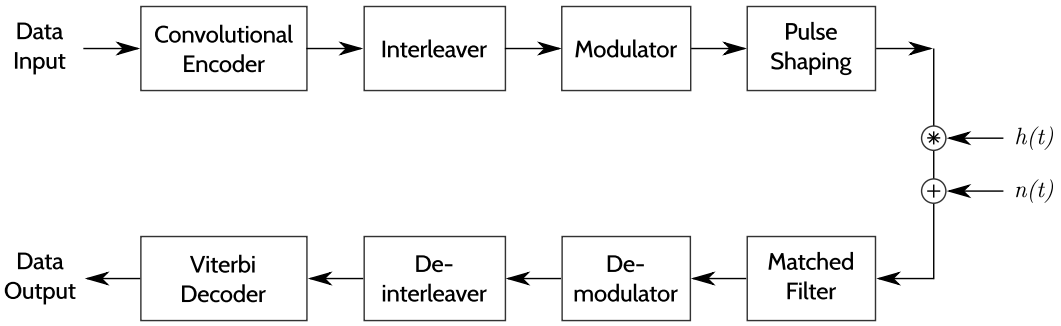

Figure 5.7.: Extended simulation setup by an interleaver

$$
\begin{aligned}
a_i &= (i \bmod l)\,\frac{N_b}{l} + \left\lfloor \frac{i}{l} \right\rfloor \\
b_i &= k \left\lfloor \frac{a_i}{k} \right\rfloor + \left[\left(a_i + N_b - \left\lfloor \frac{l a_i}{N_b} \right\rfloor \right) \mod k \right],
\end{aligned}
\tag{5.1}
$$

where

$$
\begin{aligned}
a_i &- \text{output of first permutation step} \\
b_i &- \text{output of second permutation step} \\
N_b &- \text{number of bits} \\
l &= 16, \text{number of columns} \\
i &= 1, ..., N_b - 1 \\
k &= \left\lceil \frac{bits/Symbol}{2} \right\rceil .
\end{aligned}
$$

By closer examination of the above permutation steps, it can be identified that the first step ensures that adjacent coded bits are reordered into different rows. The second permutation step rearranges adjacent coded bits in such a way that they are mapped alternately onto less or more significant bits of the constellation. This way, long runs of unreliable bits can be avoided.

At the receiver, the shuffled data needs to be de-shuffled in order to obtain the original, unaltered data. As noted in [55], following two permutations perform the inverse operations to Eq. 5.1

$$
\begin{aligned}
d_j &= k \left\lfloor \frac{j}{k} \right\rfloor + \left(j + \left\lfloor \frac{l j}{N_b} \right\rfloor \bmod k \right) \\
g_j &= l d_j - (N_b - 1) \left\lfloor \frac{l d_j}{N_b} \right\rfloor
\end{aligned}
\tag{5.2}
$$

with $j = 1, ..., N_b - 1$.

Observing the results shown in Fig. 5.8, it can be seen that introducing an interleaver to the transmission system, notably improves the system performance for all data rates and both coding rates. In most of the rate 1/2 coded scenarios, a gain of 7 dB can be obtained by using an interleaver. The gain is even larger for rate 2/3 convolutional coding. In many of the simulated scenarios the gain on SNR reaches 9 dB. Lower gain is observed for 16-QAM with 7 dB for all data rates. The least gain is experienced for 16-PSK and 20 Mbps. By closer examination of the BER outcome, it can be further noted that the results for the rate 1/2 and 2/3 codes are very similar. The significant difference being for low SNR. From an SNR above 10 dB, the results for rate 1/2 and 2/3 are amazingly close and the curves for both rates converge.

5.2.3. Performance Evaluation with Concatenated Coding

The setup in Fig. 5.9 shows an extension of the previous simulation setup by a serial concatenation of an outer Reed-Solomon (RS) code with rate 3/4 and an inner convolutional code with rate 2/3. Thus, the global coding rate is 1/2. The implemented RS encoder uses a Galois field GF(2^8). Following polynomials are used for the code and field generators:

$$\begin{aligned} \text{Primitive Polynomial:} \quad & p(x) = X^8 + X^4 + X^3 + X^2 + 1 \\ \text{Generator Polynomial:} \quad & g(x) = (X - \alpha^1)(X - \alpha^2)\dots(X - \alpha^{n-k}), \end{aligned} \tag{5.3}$$

where α is a root of the primitive polynomial for the field GF(2^{n+1}). Table 5.2 summarizes the used n, k values in the simulations.

Since the overall coding rate in this simulation setup is 1/2, the comparison in Fig. 5.10 is given for convolutional coding also with rate 1/2. Interestingly, the setup with concatenated coding needs longer to produce good results. Analyzing the results for 6.25 and 10 Mbps, it can be concluded that for lower SNR it is better to use only convolutional coding with interleaving. However, for higher SNR and modulation order, a system with concatenated coding and interleaver would give better results. For 6.25 Mbps, in the case of 16-PSK, a benefit is observed from an SNR of above 13 dB. However, the improvement for 8-PSK and 16-QAM can be seen from 14 and 16 dB, respectively. The figure looks slightly different for 10 Mbps. While 8-PSK experiences better results with concatenated coding for SNR above 11 dB, 16-PSK and 16-QAM benefit from the more complex coding structure above 13 dB. For 20 Mbps, the use of Reed-Solomon does not provide any improvement within the SNR range of interest.

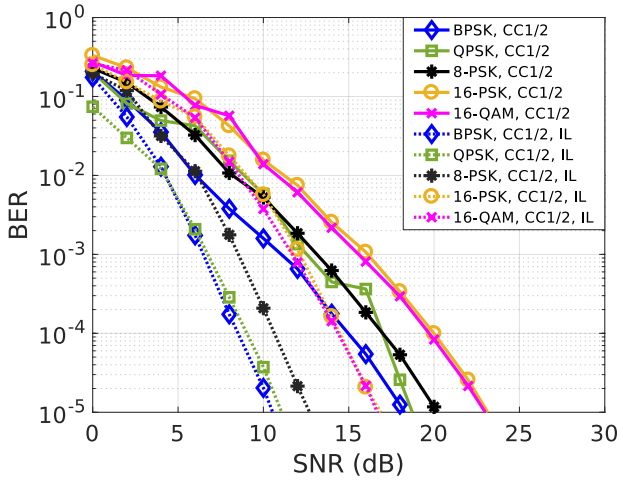

(a) BER for 6.25 Mbps

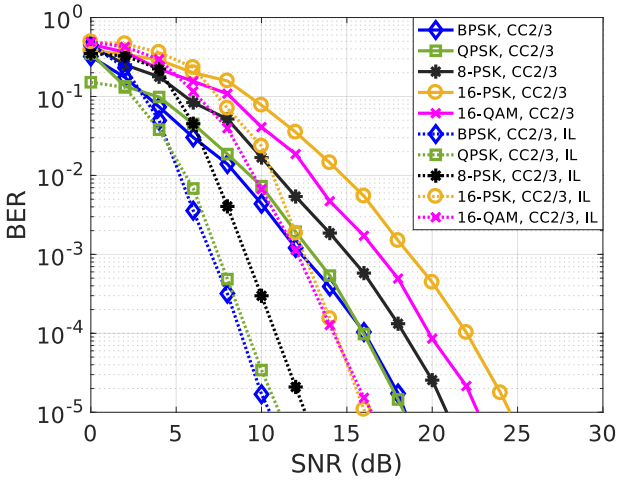

(b) BER for 6.25 Mbps

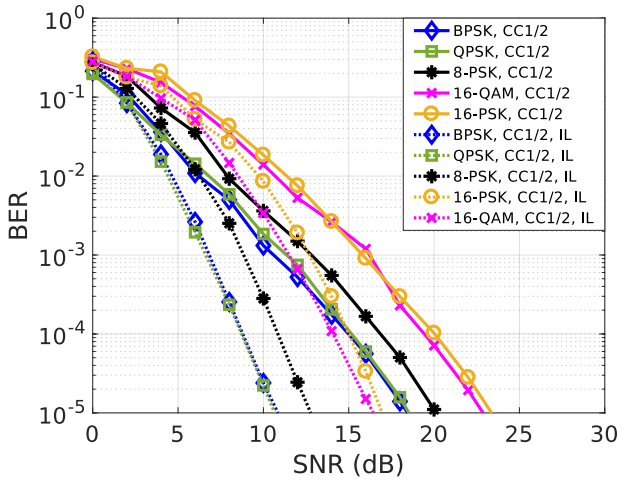

(c) BER for 10 Mbps

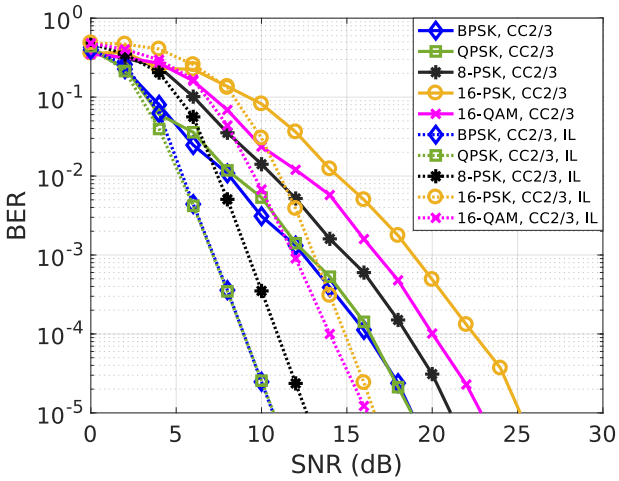

(d) BER for 10 Mbps

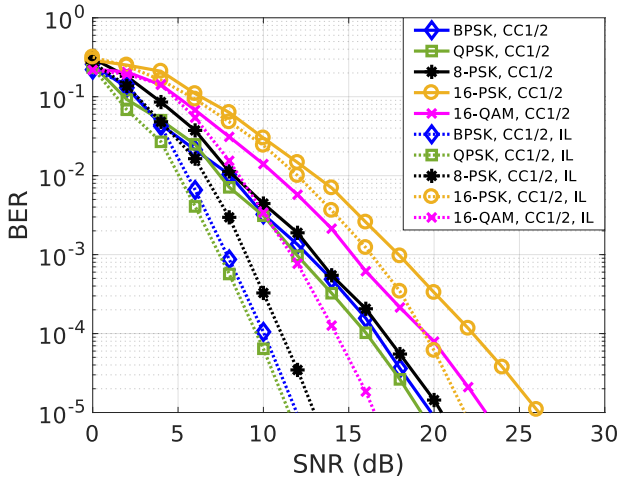

(e) BER for 20 Mbps

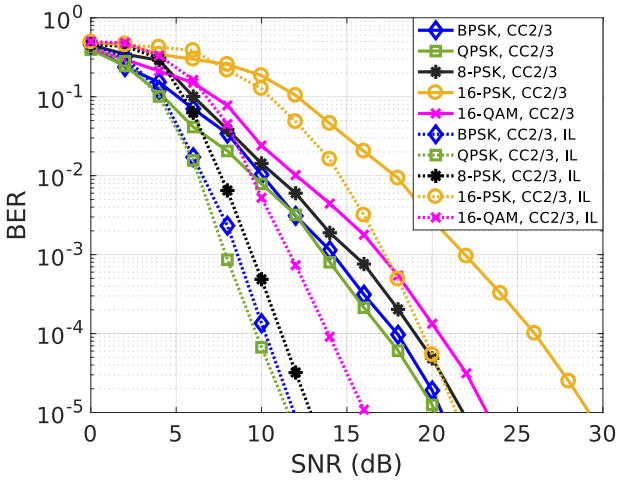

(f) BER for 20 Mbps

Figure 5.8.: Numerical results for the setup illustrated in Fig. 5.7

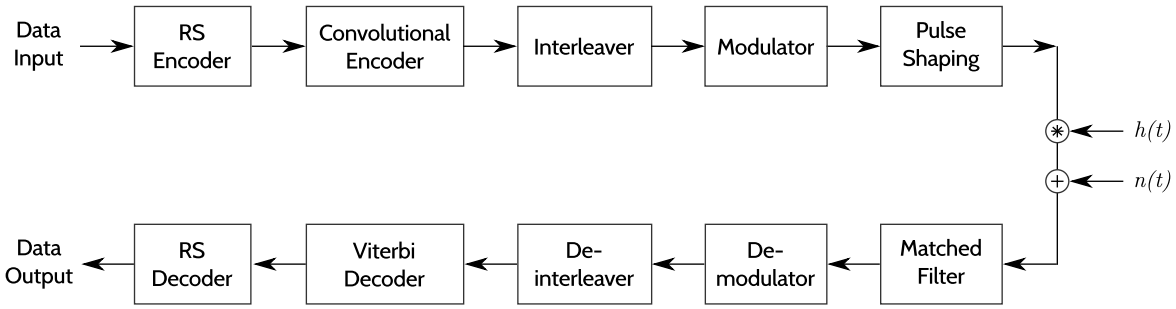

Figure 5.9.: Extended simulation setup by a Reed-Solomon Code

Modulation	RS Code (n,k,d)	CC code rate	Global code rate
QPSK	(32, 24, 9)	2/3	1/2
8-PSK	(64, 48, 17)	2/3	1/2
16-PSK	(96, 72, 25)	2/3	1/2
16-QAM	(64, 48,17)	2/3	1/2

Table 5.2.: Summary of the code parameters used in the concatenated coding scenario

5.3. Summary

Comparing of all investigated error mitigating methods, it can be concluded that convolutional coding, even with high rate, in combination with interleaving already gives very good results. By applying this method, a reasonable data rate of 20 Mbps can be achieved which is way beyond the transmission rate supported by Flexray and is close to the one used with the MOST bus over Polymer-Optical fibres. Due to the bursty nature of errors on the car power line channel, an application of standalone convolutional coding, regardless of its rate, does not give sufficient improvement. A more complex coding system, by applying an outer Reed-Solomon code and an inner convolutional code, followed by an interleaver, only improves the system performance for high SNR values above approx 11 dB.

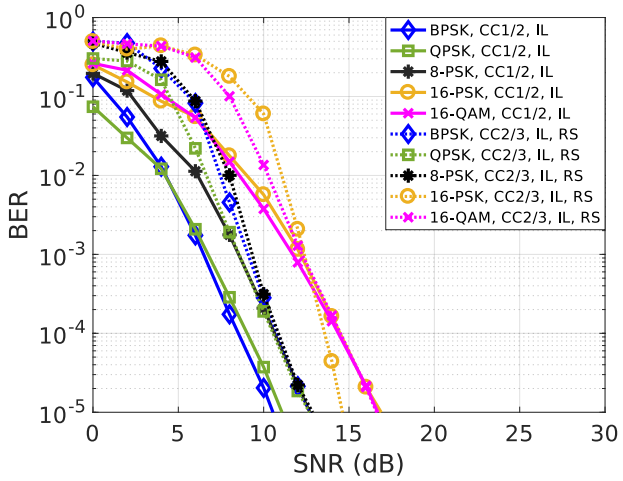

(a) BER for 6.25 Mbps

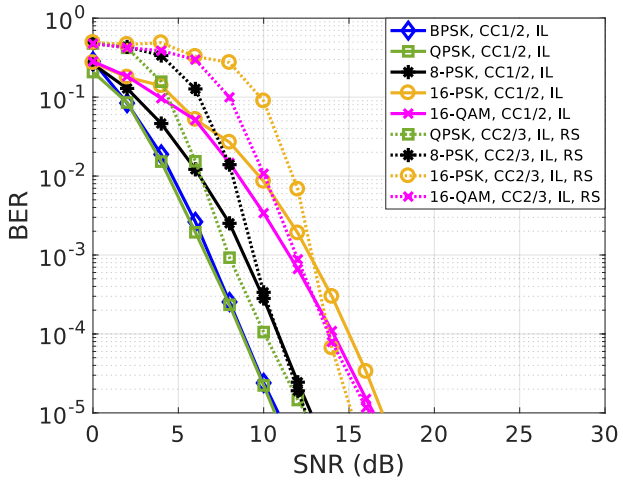

(b) BER for 10 Mbps

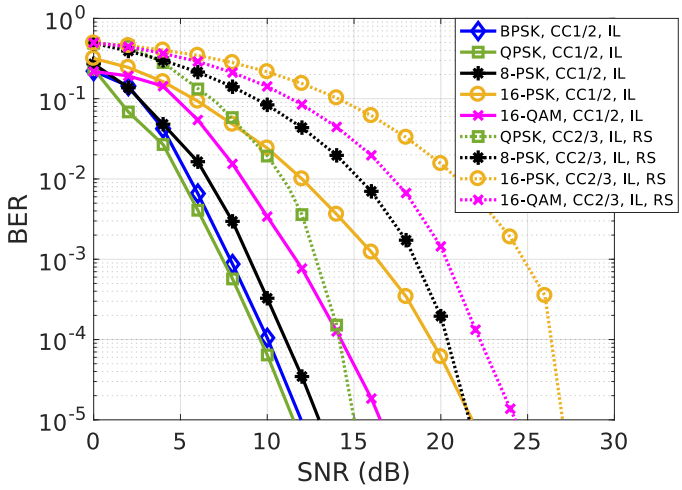

(c) BER for 20 Mbps

Figure 5.10.: Numerical results for the system setup from Fig. 5.9

6

Automotive PLC System Implementation

The foregoing chapters describe the transmission characteristics of the automotive power line channels and give a theoretical analysis of an in-car PLC system. To prove the concept and applicability of PLC in an in-vehicle environment, a basic demonstrator was developed and extensively tested. First, a laboratory environment emulating a car scenario was setup and used. Upon successful performance measurements, the demonstrator was deployed and tested in a car experimental setup. In this chapter a Field-Programmable Gate Array (FPGA)-based implementation of an automotive PLC transmission system is presented and discussed. The demonstrator's main parts are an FPGA platform used for the digital signal processing and an appropriate analog front-end. With this, sample data was sent and received at different access points in the vehicle and offline data processing was applied. This chapter summarizes the efforts of developing and evaluating a low-complexity, robust automotive power line communication system that performs in strict accordance with the limitations and restrictions set by industry and the International Telecommunication Union (ITU).

This chapter is organized as follows. First, all hardware components used in either experimental setup are described. The implementation and analysis of the digital signal processing on the FPGA is then explained as well as the offline data processing. Afterwards, some aspects of the analog domain, such as signal power, noise level and signal attenuation, are elaborated. Here, some of the challenges and proposed solutions are reviewed. Finally, the measurement results in both lab and vehicle environment

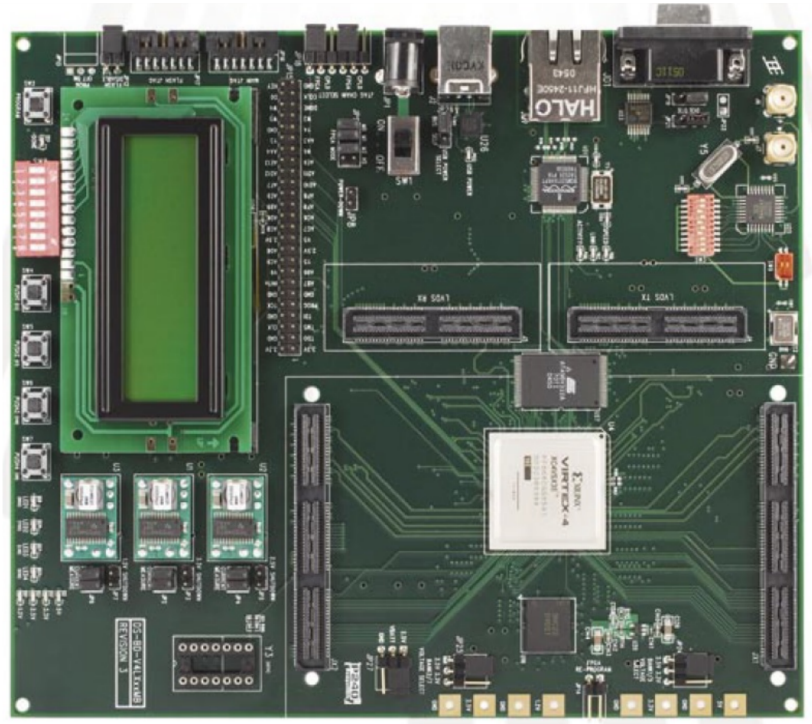

Figure 6.1.: Virtex-4 FPGA Development Board

are presented and discussed.

6.1. Hardware

In this sub-chapter the hardware components used in both laboratory and automotive experimental setups are introduced.

6.1.1. Transmitter and Receiver

The main units of the experimental in-car PLC transmission system implementation are two Virtex-4 MB development boards from Memec [56] and the appropriate analog front-ends from Avnet Electronics [57] shown in Fig. 6.1 and 6.2, respectively.

A block diagram of the main components on the FPGA development board is illustrated in Fig. 6.3. The heart of the development board is a Virtex-4 SX35 FPGA from Xilinx (Xilinx XC4VSX35-10ff668). It is connected to diverse peripheral elements enabling the board with different features, such as memory (e.g. DDR SDRAM, Flash), connectivity (e.g. 10/100PHY, RS232), clock signals (Clock Sources). For instance the

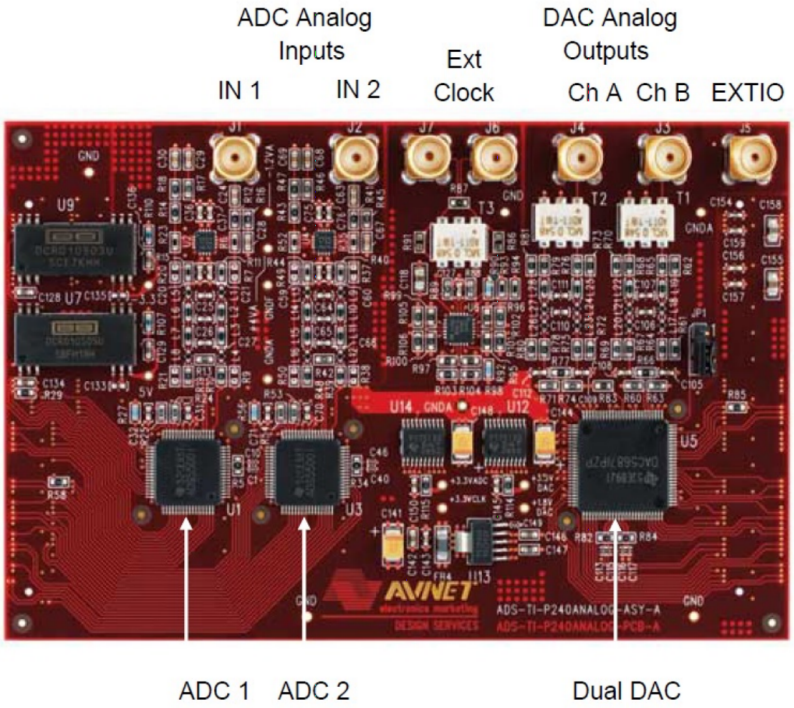

Figure 6.2.: P240 Analog Board Module from Avnet

10/100 PHY block is used in the receiver to transmit the received data to a computer for later offline processing. Some of the User LEDs are used to signal the successful accomplishment of some critical processing stages or could be also used for debugging. The programming of the FPGA is done through the JTAG Port. The Programmable LVDS Clock Source as well as the LVTTL Clock@100 Mhz are both used in the system implementation described in this Chapter. Details to each implemented module is given in Section 6.2.

The P240 Analog Module provides an advanced analog interface to the FPGA development boards. It is plugged as a daughter board onto the FPGA board using its FMC (FPGA Mezzanine Card) connectors for expansion modules, depicted as the two 132-Pin Connectors in Fig. 6.3. Fig. 6.4 shows a picture of the FPGA-based demonstrator consisting of a transmitter and a receiver FPGA baseboard with plugged-in analog daughter boards. The P240 Analog Module comes with an external differential LVDS clock input. Since clock recovery was out of scope of this implementation, the synchronization between transmitter and receiver board was enabled by feeding the clock source from the transmitter baseboard to the external clock input of the receiver's analog daughter board. The SMA Clock Output in Fig. 6.3 on the transmitter FPGA board is used for this purpose. This feature is discussed in more detail

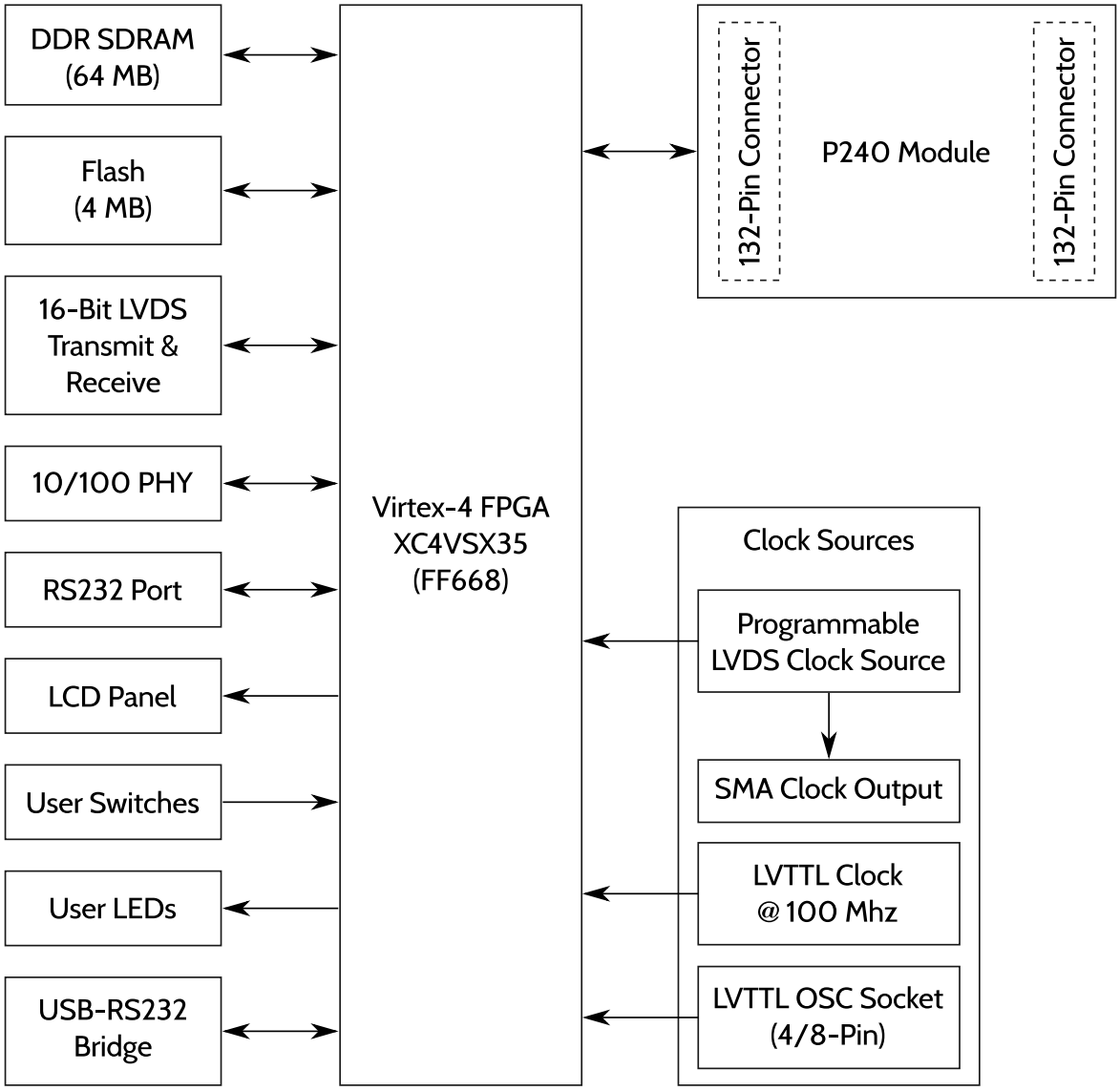

Figure 6.3.: Virtex-4 FPGA Development Board Block Diagram

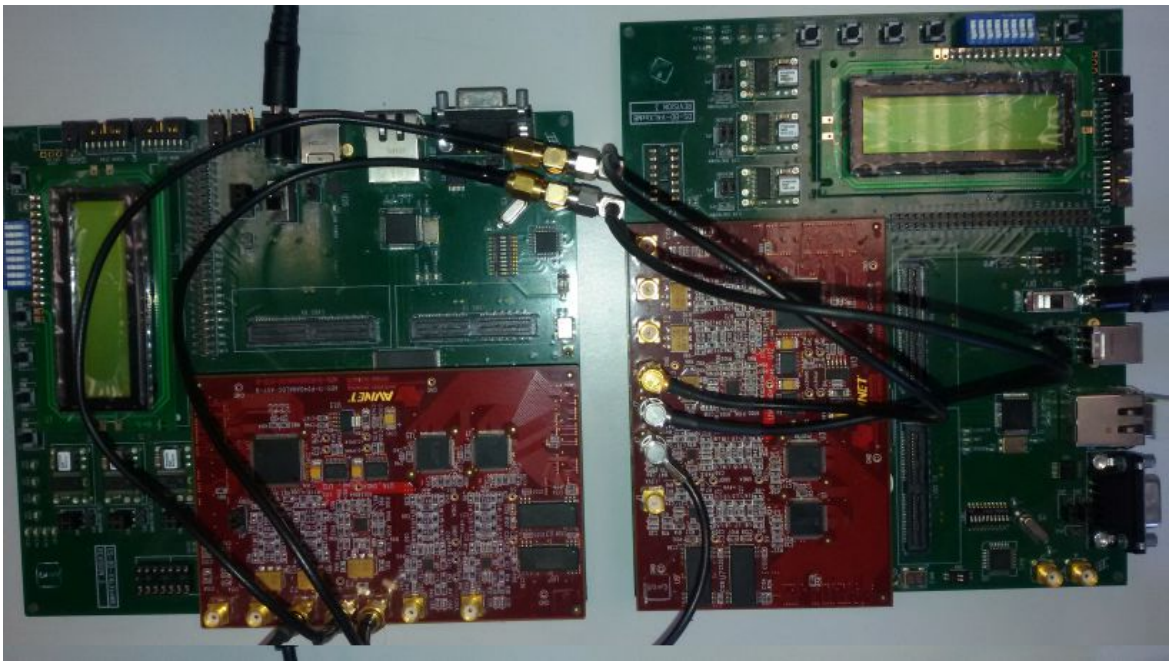

Figure 6.4.: Transmitter (left) and receiver (right) FPGA boards

in Section 6.2.6.

A high-level block diagram of the basic implementation components of the FPGA and analog boards used in the demonstrator is shown in Fig. 6.5. The demonstrator was tested by generating predefined and random data in the transmitter FPGA and transmitting it over the car power network to the receiver board. In the transmitter, mainly signal processing in the FPGA takes place. The transmitter FPGA finally feeds the transmission data to a dual-channel Digital-to-Analog Converter (DAC5687) from Texas Instruments [58] with a vertical resolution of 16 bits and a sampling rate of 400 MHz. It is used to generate the analog bipolar modulation signal. On the receiver side, an Analog-to-Digital Converter (ADS5500) also from Texas Instruments [59] is used, with a vertical resolution of 14 bits and a sampling rate of 100 MHz, to capture and transform the incoming analog signal. Once the data is captured at the receiver and the digital signal processing is performed in the Virtex-4 FPGA, the data is packed in a 4-bit wide data stream. This data stream in turn is received by an Ethernet port (ETH PHY) - a physical layer chip from Broadcom (BCM5221 10/100 PHY) [60]. Finally, the Ethernet packets are sent through the RJ-45 connector to a computer.

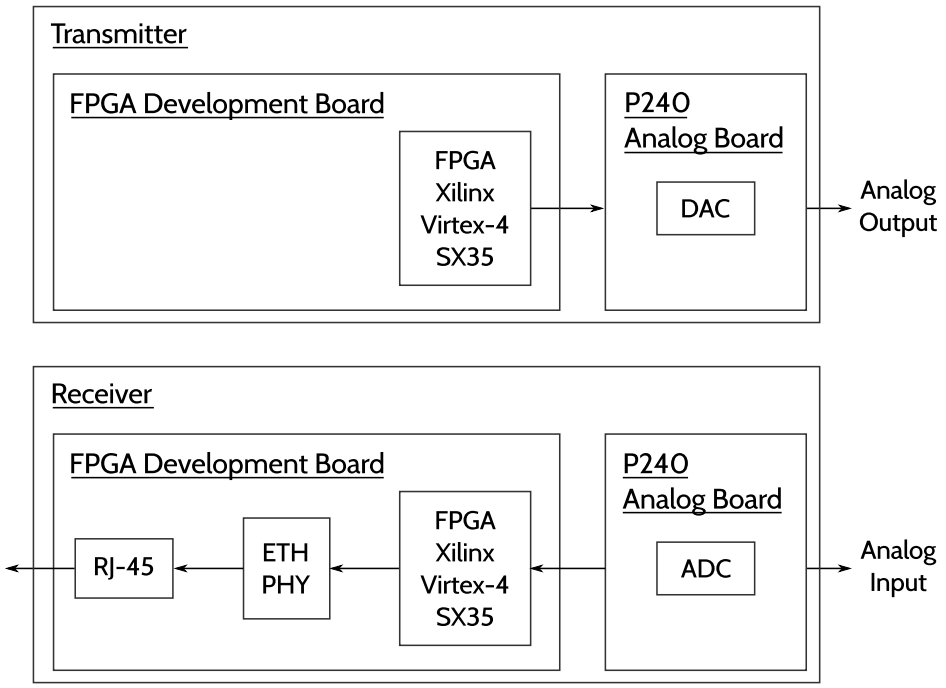

Figure 6.5.: High-level block diagram of the FPGA board and the analog module

6.1.2. Amplifiers

As discussed in Section 2.2, automotive power lines, when used for data transmission, introduce a significant attenuation to the data signal of up to 60 dB. When the attenuated transmitted signal is then being coupled with the high power noise within the vehicle, no successful reception can be guaranteed. For that reason, in order to compensate for the attenuation, two amplification stages were integrated in the PLC system, each including one amplifier (HF-Amplifier RFA 403) from ELV. The inverting manner of the amplifiers is compensated by using a two-stage amplification and hence preserving the original signal. The frequency band of the amplifiers is defined between 10 MHz and 2 GHz. At the frequency of interest of 25 MHz, the measured amplification and the maximum output power amounts to 23 dB and 20 dBm, respectively.

6.1.3. Balancer

The DC offset of the amplifier output and that of the FPGA board are different from the automotive supply voltage. For that reason, transformers with DC blockers called balancers were used to isolate the DC voltage of the transmitter from the power line of the car. A balancer uses a transformer to conduct only varying signals while isolating the DC voltage. For the experimental implementation, a wide-band 0.2 – 500 MHz

Figure 6.6.: Measured frequency response of the low-pass filter

coaxial RF transformer with 50 Ω impedance, RF power of 250 mW and DC current of 30 mA was used. The insertion loss at the carrier frequency 25 MHz accounts for 3 dB.

6.1.4. Low-Pass Filter

The presence of a strong impulsive noise in an automotive environment has been discussed in Chapter 3.1. Considering that the PLC demonstrator applies Binary Phase-Shift Keying (BPSK) as a digital modulation scheme, high level of noise can affect the detected phase shift points by the receiver and corrupt the data. To reduce the effect of noise, a low-pass filter with sharp frequency response was used. A 7th-order Chebysheff low-pass filter with 50 Ω impedance in T structure was designed and developed. The passband ripple was chosen to be rather high because the channel itself already has a much higher ripple. In addition, a sharp decay of the passband is necessary to use the full bandwidth of the ADC (Analog-to-Digital Converter) which is about 50 MHz. The passband ripple in the final design is slightly lower than 3 dB. Fig. 6.6 shows the measured frequency response, while Fig. 6.7 and Fig. 6.8 depict the design and implementation of the filter, respectively.

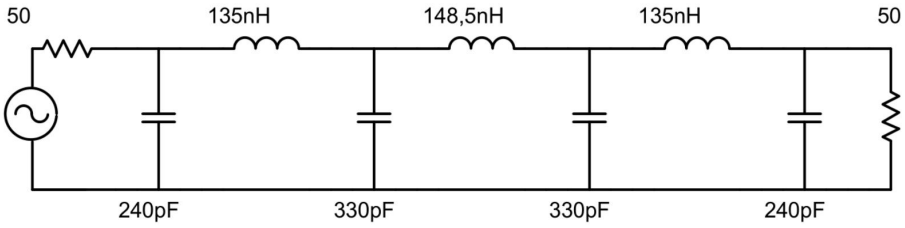

Figure 6.7.: Circuit of the low-pass filter

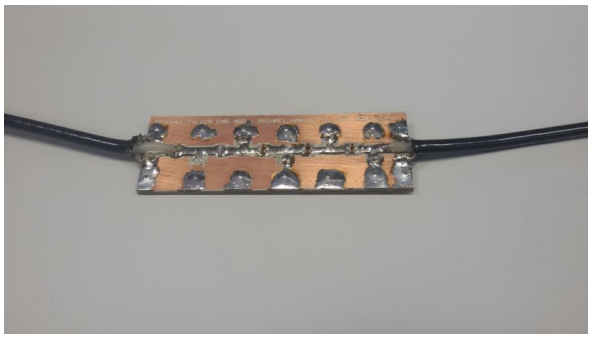

Figure 6.8.: Assembled PCB of the low-pass filter

6.1.5. Noise Generator

A programmable noise generator UFX PRG-7107 from Noisecom was used to generate the additive noise in the lab experimental setup. The added noise is controlled by a parameter called noise attenuation. It is inversely proportional to the magnitude of the noise added to the signal. The maximum noise attenuation level, where in fact no noise is added, is at 63.75 dB. By decreasing the noise attenuation the emulated noise power at the bandwidth of interest is being increased.

6.2. Implementation

The following sections cover the realization of the FPGA-based transmitter and receiver of an automotive PLC transmission system demonstrator. All software modules are implemented in VHSIC Hardware Description Language (VHDL). Each design block as well as the DAC and ADC configurations are explained in detail within the ongoing sections. Fig. 6.9 illustrates a high-level block diagram of the demonstrator and the developed software modules.

In the transmission chain first sample data is generated by a data frame generator module which is then being encoded and modulated. Leaving the digital processing

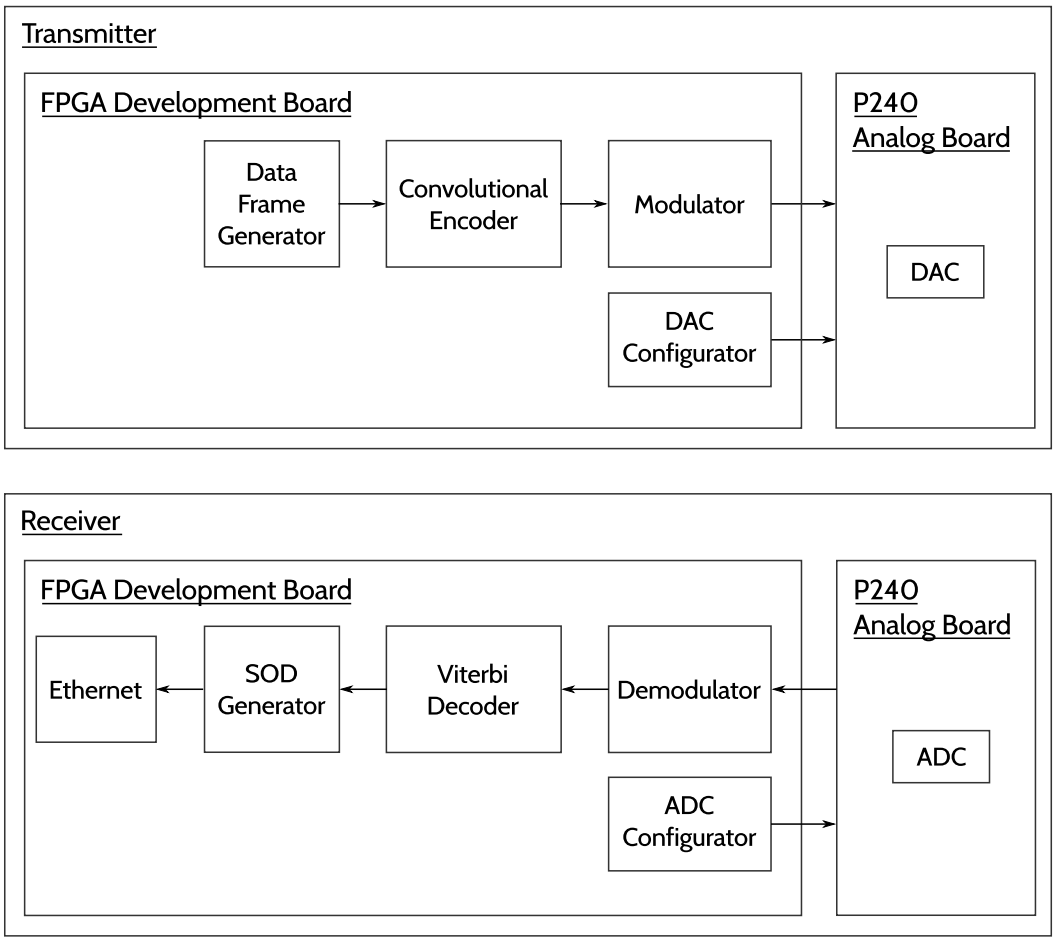

Figure 6.9.: Block diagram of transmitter and receiver software modules

domain and herewith the FPGA development board, the signal is passed to the analog daughter board for further processing to finally output an analog signal. The analog boards at the transmitter and receiver are identical. In Fig. 6.9 only the DAC and accordingly ADC are included to identify which path the signal will be processed by. Sec. 6.2.4 gives a detailed description of the analog board and its components. At the receiver side the counterpart is present. A separate VHDL module configures the D/A and A/D processing paths on the analog board to ensure the desired functionality.

6.2.1. Data Frame Generator and Start of Data Generator

The data frame generator module can produces a PRBS (Pseudo-Random Binary Sequence) or a fixed pattern of sample data. After successful verification of a PRBS transmission a fixed pattern sample data was used to ease later data analysis. This module generates 48-byte long frames. Each frame includes 46 bytes of payload data,

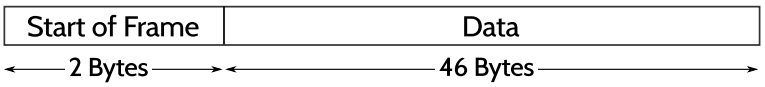

Figure 6.10.: Frame structure at the output of data frame generator

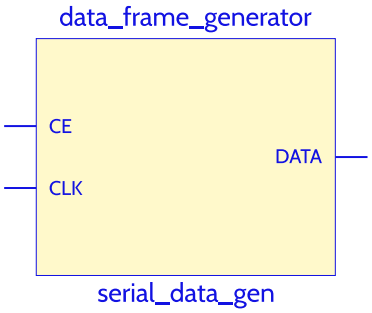

Figure 6.11.: Data Frame Generator

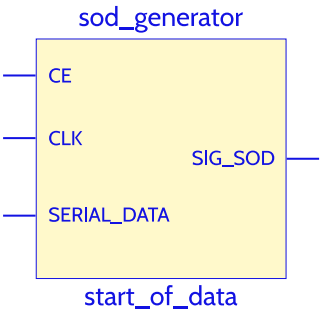

Figure 6.12.: Start of Data Generator

resulting out of the minimum payload size for an Ethernet packet, and two bytes Start of Frame (SOF) delimiter as depicted in Fig. 6.10. Each byte of the payload data contains incrementing values from 00_{16} to $2E_{16}$. The SOF indicates to the receiver the beginning of a new Ethernet packet and hence the start of data buffering. Between two frame generation loops, six cycles of inter-frame delay are skipped to better distinguish the start of frames. This unit is clocked at 6.25 MHz and outputs a continuous single-bit sequence `DATA` as shown in Fig. 6.11. This results in a data rate of 6.25 Mb/s and a frame duration T_{frame} of 61.44 µs. These values are key parameters for optimizing the system performance and e.g. designing an impulsive noise mitigation scheme.

The counterpart of the data frame generator is the start of data generator (SOD generator) at the receiver. A high level block diagram is illustrated in Fig. 6.12. This module analyzes the received data and triggers an activation signal to the Ethernet MAC unit to mark the start of each data payload. Once the received data is successfully demodulated and decoded, the original frames generated by the transmitter are obtained as a bit sequence. As the decoded data is fed to this unit, it is saved in a shift register with the size of a frame header (two bytes). Upon successful detection of the SOF delimiter in the shift register, one clock cycle later the `SIG_SOD` trigger signal is set to '0' which activates the Ethernet MAC module to start buffering the payload data. In other words, start of data generator analyzes the frame headers and triggers an activation signal to the Ethernet MAC unit to mark the start of each data payload.

6.2.2. Coding and Decoding

A convolutional encoder is a simple, relatively efficient and fast method of encoding data and is used in this experimental implementation to improve the transmission robustness. A block diagram of the implemented encoder unit is shown in Fig. 6.13. The module includes three input ports - two clock inputs at 6.25 MHZ and 12.5 MHz, and one data port connected to the continuous single-bit output of the data frame generator. The encoding itself is done by the `convolutional_cod` submodule which is a Convolutional Encoder v7.0 IP core from Xilinx. Its basic architecture is depicted in Fig. 6.14. The incoming data is brought into a shift register, called the constraint register, a bit at a time. The output bits are generated by modulo-2 addition (XOR) of the required bits from the constraint register. The bits to be XOR'd are selected by the convolutional codes. Further, a constraint length of 7 and convolutional codes $conv_{code1} = 1001111$ and $conv_{code2} = 1101101$ are used. The coding rate of the implemented encoder unit is 1/2 and indicates the ratio of input to output rate (bits). Hence, the output of this module is the encoded data as a vector of width two, equal to the output rate. This results in a doubled data rate at the encoder's output. The implemented PLC demonstrator is a single-channel transmission system which requires a serializer at the encoder's output. The serializer unit is clocked at 12.5 MHz and it outputs with no delay cycles as shown in Fig. 6.15.

The receiver counterpart to the convolutional encoder is a Viterbi decoder which uses the Viterbi algorithm to calculate the original hidden state of the input. To ensure the compatibility with the encoder, the decoder parameter values were matched with those of the encoder. In addition, a traceback length of 42 was chosen. Analog to the encoder, the decoder has two clock inputs at 6.25 MHz and 12.5 MHz respectively, and one data input port at 12.5 MHz. However, the Viterbi algorithm expects two data streams each at 6.25 MHz. Consequently, a parallelizer clocked at 12.5 MHz is developed and used at the decoder's input. Due to the complex structure of the Viterbi decoder the latency of the output data is rather significant and depends on the traceback length (l_{tb}), constraint length (l_c) and the encoder's output rate (r_{out_enc}). Using Eq. 6.1, the latency can be roughly estimated as follows

$$\delta(t) = 4l_{tb} + l_c + r_{out\_enc} \tag{6.1}$$

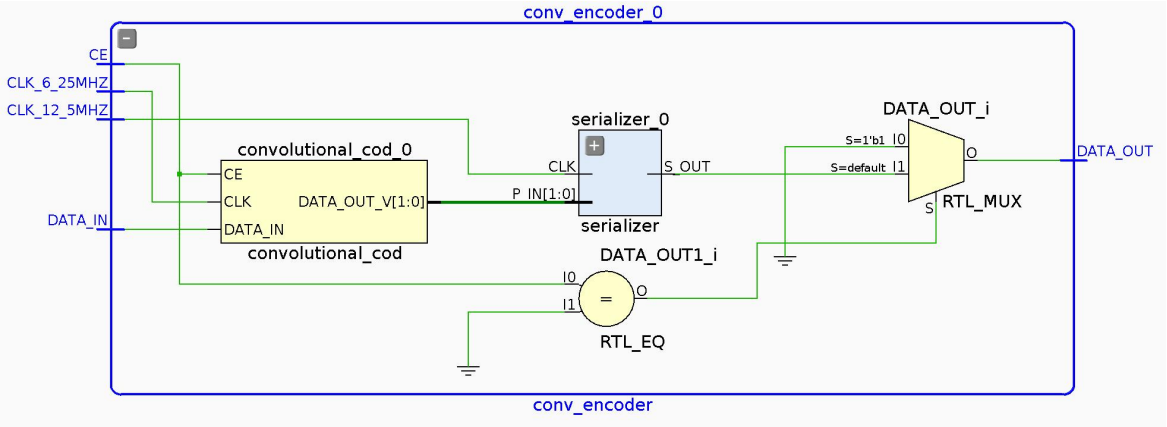

Figure 6.13.: Block diagram of convolutional encoder

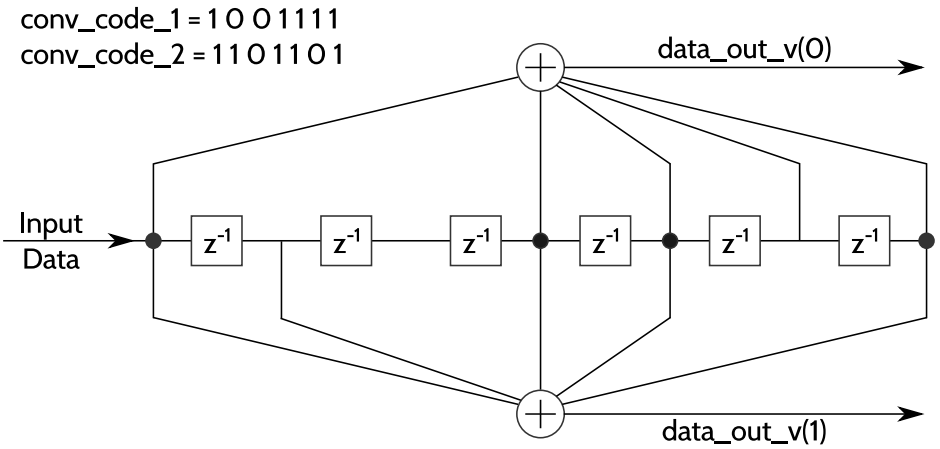

Figure 6.14.: Convolutional Encoder Constraint Length 7

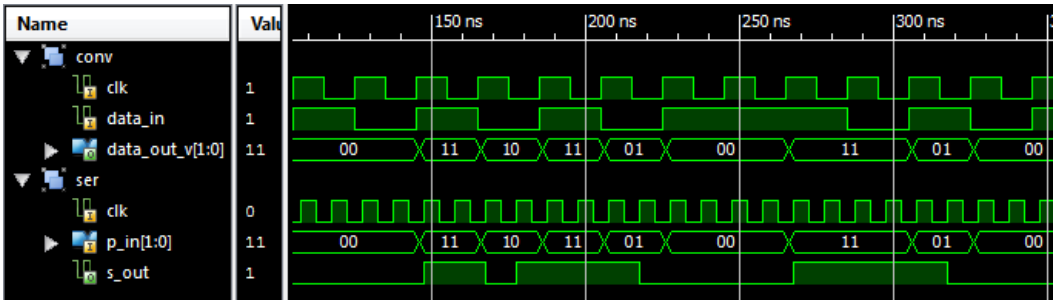

Figure 6.15.: Testbench simulation for convolutional encoder and serializer

6.2.3. Modulator and Demodulator

A modulator and a demodulator are realized within a common VHDL module for the purpose of deployment convenience and to enable bidirectional functionality of both transmitter and receiver. In case of a unidirectional transmission only one processing path, transmitting or capturing, is active. As previously mentioned, the automotive PLC demonstrator applies BPSK source modulation. It is the simplest form of Phase Shift Keying (PSK) and uses two phases, separated by 180°, to convey data. The simplicity of this scheme and the resultant low implementation and development cost correlate with the requirements applying to this demonstrator. Further, it provides the most robust performance to channel impairments compared to other PSK forms which is an indispensable quality of an in-vehicle PLC transmission system considering the high level of impulsive and bursty noise present on the channel (see Chapter 3.1). A detailed description of BPSK can be found in Chapter 4.

A block diagram of the VHDL module is depicted in Fig. 6.16. At input port `pn_input_bit` the modulator unit receives the encoded data with rate 12.5 Mb/s. The source modulation is implemented at a carrier frequency f_c of 25 MHz which has been chosen based on the characteristics of the transmission channel. As discussed in Chapter 2.2 the in-vehicle PLC channel offers on average the lowest attenuation in the frequency range around 25 MHz. Although, some measurements on the noise present on the in-vehicle power line channel, show a clustering of power peaks at 25 MHz, their power level barely exceeds -60 dBm. This noise level is anyways considered while establishing the demonstrator and setting up the lab environment. Performing carrier modulation in the digital domain saves additional analog equipment and introduces less noise to the system. For realizing a BPSK modulation at a given carrier frequency a carrier signal and its invertible (separated by 180°) are first generated. The carrier signal is implemented by filtering a digital clock signal (`clk_in_sinus`) which is a unipolar rectangular signal. Hence, it is composed of infinite number of sine waves and its spectrum consists of the fundamental wave frequency, here 25 MHz, and its odd multiples, i.e. 75 MHz, 125 MHz and so on. The filtering is done by a Finite Impulse Response (FIR) filter configured as a low-pass filter with a cut-off frequency at 35 MHz and a sampling rate of 100 MHz (`clk`). The inverted carrier signal is generated by taking the negative FIR output. Having this, the modulation is done by switching between the positive and negative carrier signals. That is, depending on the logical state of the data signal the modulator data output port (`bpsk_mod_sig`) is either connected to the positive signal to represent a logical '1' or to the negative one

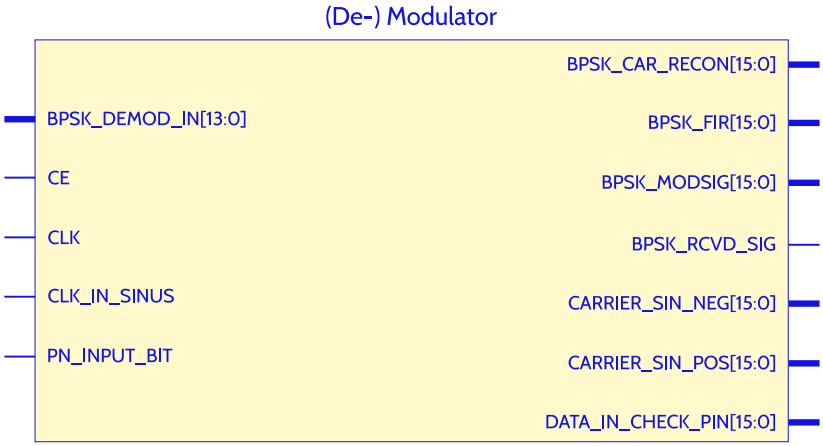

Figure 6.16.: Block diagram of (de)modulator unit

for a logical '0' and consequently, contains the typical BPSK 180° phase shifts. The output vector has a width of 16 bits to match the DAC resolution.

The demodulator unit receives a digital vector signal with a 14-bit width, generated by the ADC. To reconstruct the original signal, this vector is multiplied with a 25 MHz carrier signal sampled at 100 MHz. Since both, transmitter and receiver, boards are driven by the same clock source, a nearly identical carrier signal can be generated in both modulator and demodulator. This enables a successful operation without the need of a clock recovery mechanism which was out of scope of this work. In the following processing step, the received signal is filtered by a low-pass filter and finally passed through a decision unit. The demodulator's output (`bpsk_rcvd_sig`) is a continuous single-bit sequence with rate 12.5 Mb/s connected to the decoder's input.

6.2.4. D/A and A/D Converters

A block diagram showing the main components of the P240 analog board module is given in Fig. 6.17. It can be clearly distinguished between a D/A and an A/D processing path. The D/A path consists of a DAC followed by a low pass filter and a transformer. The A/D path includes an amplifier, a low pass filter and an ADC which outputs the digital signal. The P240 analog board comes with a dual-channel DAC (DAC5687) and two single-channel ADCs (ADS5500) from Texas Instruments. However, only one channel from the DAC and one ADC are used by the implementation. The operating mode of the DAC and ADC is determined by the configuration of their control registers. For each converter path, a VHDL module was developed to allocate the registers with desired values. These modules are connected to the relevant FPGA

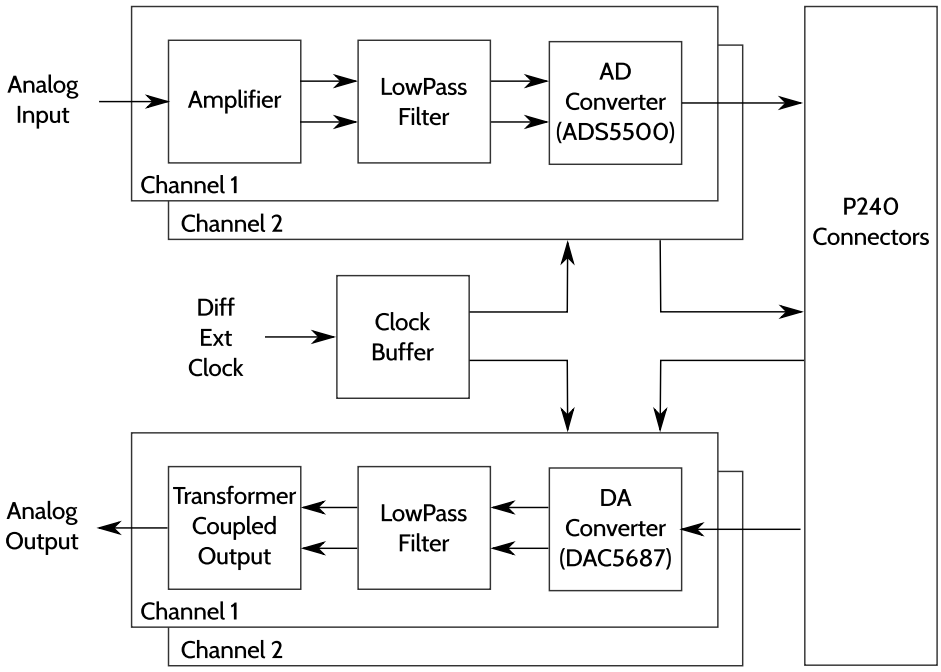

Figure 6.17.: Block Diagram of P240 Analog Board Module

pins which are linked through an FMC (FPGA Mezzanine Card) connector to the appropriate register control pins. Both configuration modules, for the D/A and A/D processing paths, include a state machine and an internal counter to ensure the FPGA processing will start upon complete and successful configuration of the analog devices. They are clocked by a dedicated clock source (derived from LVTTL Clock @ 100 MHz in Fig. 6.3) running at 6.25 MHz, see subsection 6.2.6.

Fig. 6.18 gives a short overview of some relevant DAC registers and the assigned values. A complete listing can be found in [58]. Based on the assigned values the DAC input data is interpreted as two's complement. Further, it is set to operate in the X4 mode which activates a FIR filter with a cutoff frequency $f_{cutoff} \approx 0.5 \cdot f_{IN}$, with f_{IN} being the DAC input data rate, at the DAC's input. The filter input is the encoded and modulated data at a carrier frequency $f_c = 25$ MHz and the input sample rate equals 100 MHz. This results in a cutoff frequency $f_{cutoff} = 50$ MHz which is ideal considering the spectrum of the input signal. Further, the DAC is configured to use an inverse sinc filter to flatten the frequency response of the sample-and-hold output that runs at 100 MHz. By allocating the gain registers the full-scale DAC output current is set.

The ADC is set to operate in the normal mode with the internal DLL turned on. Further details can be found in [59]. The sampling rate is 100 MHz which fulfills the

Name	Address	Default	Bit 7 (MSB)	Bit 6	Bit 5	Bit 4	Bit 3	Bit 2	Bit 1	Bit 0 (LSB)
CONFIG0	0x01	0x00	0 pll_div(1:0) 0		pll_freq 0	pll_kv 0	0 interp(1:0) 1		invpllllock	1 fifo_bypass
CONFIG1	0x02	0x00	0 qflag	interl	1 dual_clk	1 twos	0 rev_abus		revobbus	firobypass 0 full_bypass
CONFIG2	0x03	0x80	0 nco	0 nco_gain	0 qmc	0	0 cm_mode(3:0) 0		0	1 invsinc
CONFIG3	0x04	0x00	0 sif_4pin	dac_ser_data 0	half_rate 0	unused 0	usb 0	0	counter_mode(2:0) 0	0
SYNC_CNTL	0x05	0x00	sync_phstr 0	sync_nco 0	sync_cm 0	0	sync 0 fifo(2:0)	0	unused 0	0 unused
DACA_GAIN_0	0x17	0x00	daca_gain(7:0) 11111111							
DACB_GAIN_0	0x18	0x00	dacb_gain(7:0) 11111111							
DACA_DACB_GAIN_1	0x19	0xFF	daca_gain(11:8) 1111				dacb_gain(11:8) 1111			

Figure 6.18.: Excerpt from the DAC register map with allocations

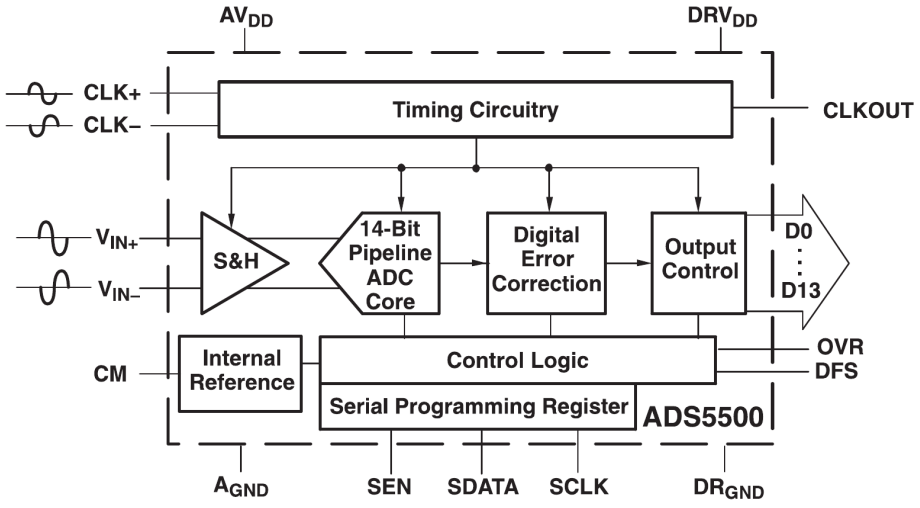

Figure 6.19.: Functional Block Diagram of ADC

Nyquist theorem where $f_s > 2(f_c + f_{data})$, with f_s being the sampling rate, $f_c = 25$ MHz the carrier frequency and $f_{data} = 12.5$ MHz the occupied data bandwidth. The ADC has a resolution of 14 bits. Its block diagram is shown in Fig. 6.19. The first stage consists of sample and hold (S/H) circuit, which holds the value of the signal during its conversion time. When the sample value is converted, it takes a new value and holds it for the next conversion time. The second stage is a 14 bit pipelined structure of 1-bit ADC that takes 14 analog samples from the S/H circuit in a pipeline. The Digital error correction block removes the errors due to the noise in the signal. Finally, the output control logic outputs the 14 bit digital representation of the analog signal. The serial programming registers set the modes of operation of the ADC and are configured through the FPGA.

6.2.5. Ethernet

To analyze and evaluate the performance of the PLC demonstrator, the Ethernet protocol was implemented and used to transmit the received data from the receiver board to a computer for later offline processing. Since the transmitted data is generated within the FPGA on the transmitter board (see Fig. 6.5), the Ethernet module is used only in the receiver board. However, the implemented module supports transmission and reception of data. The implementation was realized as an extension of the Xilinx Tri-Mode Ethernet MAC IP Core [61]. The MAC core supports transmission rates of 10, 100 and 1000 Mbps. The demonstrator runs this module at a rate of 100 Mbps, i.e. it supports a maximum data rate of 100 Mbps. Fig. 6.20 illustrates a high level functional block diagram of the Ethernet unit and the integrated MAC IP Core. The frame generator on the left side uses the continuous bit sequence output of the Start of Data (SOD) unit to generate valid Ethernet packets. First, the frame generator input data, which is the output of SOD, is saved bitwise with a rate of 6.25 Mbps in a buffer until the full length of 46 bytes is reached. The following two bytes SOF delimiter are removed from the data stream. Afterwards, the destination and source MAC addresses are inserted and the Length/Type field is appended. The resulting frames are then fed in one-byte steps, clocked at 25 MHz, to the TX Client FIFO. Here, TX refers to the operational mode of the Ethernet unit. On the receiver board, the module operates in a transmission mode. The transmission and receiving FIFOs (`Tx Client FIFO` and `RX Client FIFO`) are implemented as 4 KB Block RAMs (BRAMs) and hence, can be used for all supported transmission rates. The client interface is used to initiate frame transmission to the Ethernet MAC core. The transmit engine within the Ethernet MAC Core accepts Ethernet frame data from the client interface, adds the preamble field to the start of the frame and appends the Frame Check Sequence (FCS). Consequently, the length of an Ethernet packet equals 72 bytes and yields from the partitioning as illustrated in Fig. 6.21. It further ensures the interpacket gap (IPG) between successive frames meets the specifications of 96 bit times. The physical interface connects the Ethernet module to the in- and outputs of the FPGA board.

6.2.6. Clock Management

The FPGA board comes with three clock sources, two fixed and a programmable one. The crystal clock marked with a red square in Fig. 6.22 generates oscillations at 100 MHz carried by the CLK_CONFIG signal. A derivative of it is used as a configuration clock for the analog board. The green square in Fig. 6.22 indicates a 25 MHz

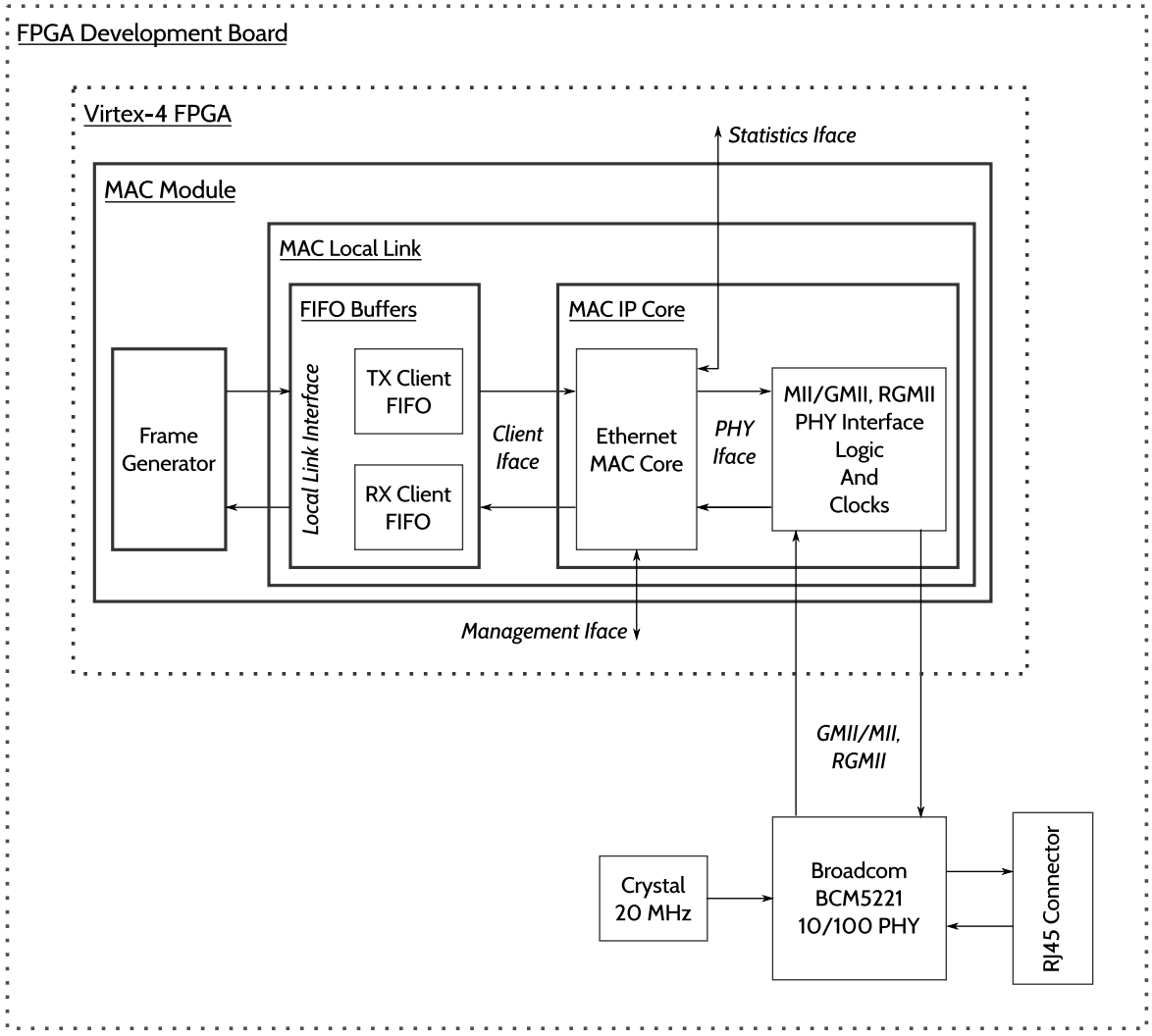

Figure 6.20.: Ethernet MAC design

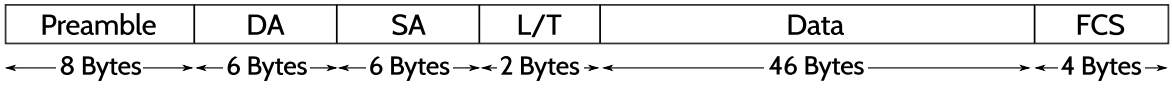

Figure 6.21.: Ethernet packet structure

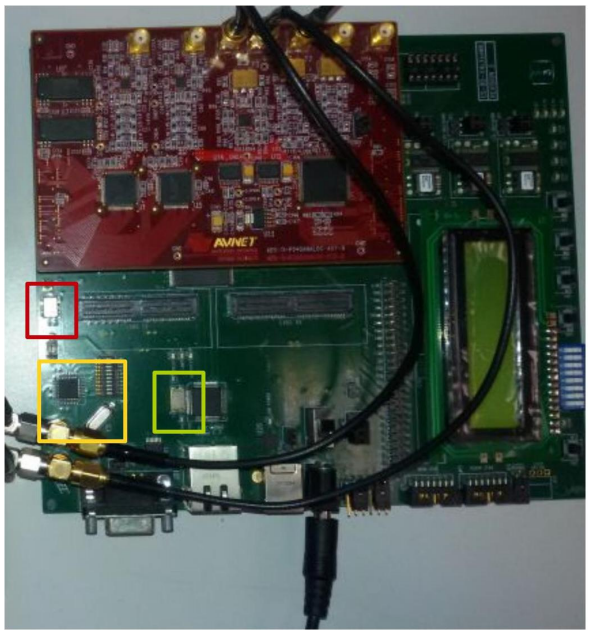

Figure 6.22.: Location of crystal oscillators on the FPGA board

oscillator used by the Ethernet PHY chip. The yellow square marks a configurable clock which uses the ICS8442 crystal oscillator-to-differential LVDS synthesizer. This clock source can be configured to minimum 25 MHz and maximum 700 MHz in irregular steps. The clock management realized for the experimental setup is depicted in Fig. 6.23. The programmable clock source is set to 400 MHz and is carried in the FPGA by the CLK_DATA_IN signal. A derivative of it is used as the main clock source for the FPGA processing and for driving the analog daughter board. The clock signal connected to the differential LVDS clock source is first fed from the FPGA board to a clock buffer (CDCP1803) on the analog module which synchronizes the input clock to the ADC and the DAC to a common clock source. The clock buffer is hardwired to supply a 4X divided clock to the ADC and a 1X clock to the DAC. Each ADC generates and forwards to the FPGA its own clock synchronized to the converted output data. The ADC output clock signal has a frequency of 100 MHz and corresponds to the main clock on the FPGA.

The Digital Clock Manager (DCM) primitive in Xilinx FPGA parts is used to implement a delay locked loop, digital frequency synthesizer, digital phase shifter, or a digital spread spectrum. The FPGA used in this demonstrator comes with four such DCMs which are all used in different stages of the FPGA processing as digital phase shifters and clock multipliers. Tab. 6.1 gives an overview of the used DCMs, their usage and configuration. All DCM units except for DCM_CONFIG are clocked by the

DCM unit	Clock Source	DCM Input	f_{in} (MHz)	f_{out} (MHz)
DCM_CONFIG	LVTTL @100MHz	CLK	100	6.25
DCM_DV16	Programm. LVDS @400MHz	CLK_DATA_IN	100	6.25
DCM_ETH	Programm. LVDS @400MHz	CLK_DATA_IN	100	25; 100 with ψ =0°,180°
DCM_CONVIT	Programm. LVDS @400MHz	CLK_DATA_IN	100	12.5

Table 6.1.: DCM configuration

CLK_DATA_IN clock signal. Hence, the output of DCM_CONFIG and the other DCMs are not necessarily synchronous. DCM_CONFIG provides a 6.25 MHz clock signal, used for configuring the analog board. During the period of configuration the signal processing in the FPGA is paused. Upon complete and successful configuration, the signal processing in the FPGA is started. Thus, the asynchronism of the clocks does not affect the FPGA operation. The output of DCM_DV16 is used for the data frame generator in the transmitter as well as for encoding and generating the MAC frames in the receiver. DCM_ETH's output is used besides for clocking the Ethernet MAC module also for the modulator and demodulator units. It further provides the analog board and in particular the dual-channel DAC with two 100 MHz clock signals with a phase shift of 0° and 180°, respectively. The clock signal output of DCM_CONVIT is applied to the serializer and parallelizer blocks used with the encoder and decoder, respectively. All DCMs have a locking mechanism available which is an important aspect of clocking. When a DCM is locked, its output is in-phase with the input clock signal. Thus, phase delays and hence errors can be avoided. Fig. 6.23 shows a high-level block diagram of the clock sources on the FPGA board and the clocking distribution in the FPGA and analog board. For convenience, only one DCM block is illustrated as an abstraction of all DCM instantiations. Therefore, the signal representation is highly simplified. The illustrated SMA connectors on the diagram are corresponding to those visible in Fig. 6.4 and connected by short, black cables,

which feed the clock signals from the oscillations on the FPGA board into the analog board.

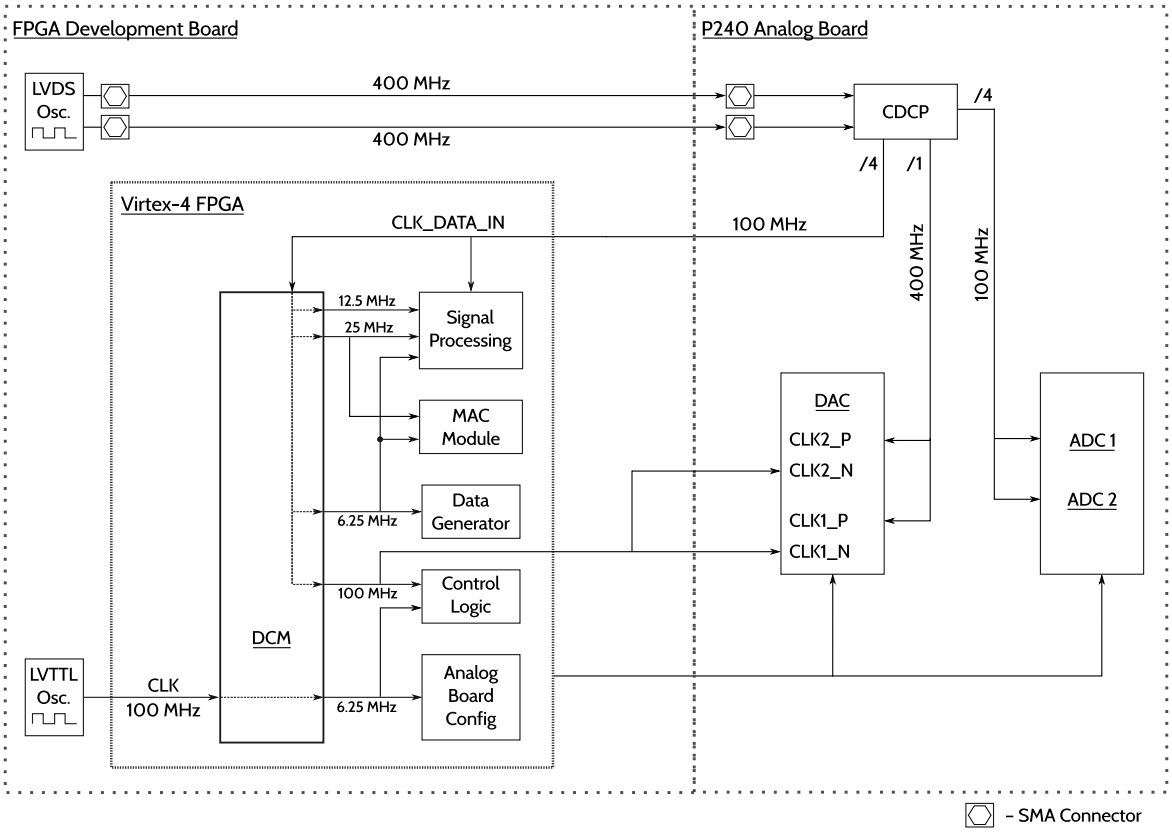

Figure 6.23.: Clocking realization

6.3. Performance Evaluation

Extensive tests and measurements were carried out in both a controlled lab and a test vehicle environment in order to evaluate the performance of the experimental implementation. Both setups and the corresponding results are presented and discussed in the subsequent sections.

6.3.1. Lab Environment

Upon making comprehensive measurements of the signal attenuation and noise level present on the automotive power line channel (cf. Sec. 2.2 and Sec. 3.1), a lab environment was set to emulate a power line transmission within a vehicle. Fig. 6.24

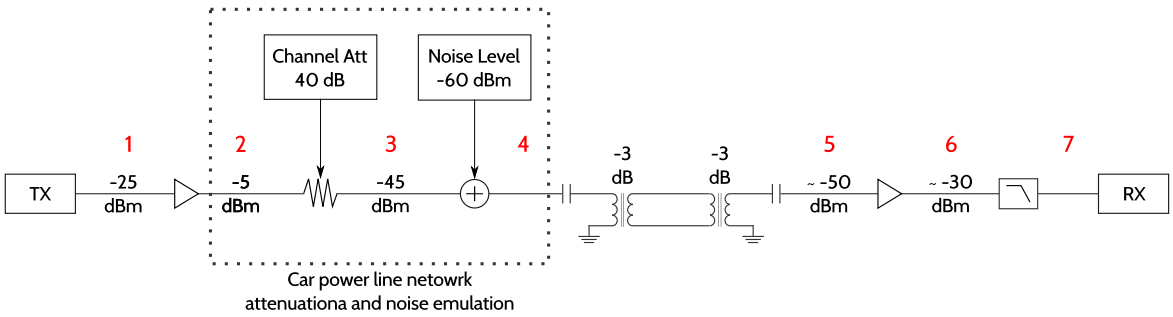

Figure 6.24.: Lab experimental setup of an automotive power line transmission system

illustrates the lab setup used to emulate a rather worst case scenario, compared to the measurement results, of an automotive power line communication channel. The components and equipment used in this setup are described in Sec. 6.1. Signal power spectrum and waveform measurements have been performed to analyze the performance in each stage of the setup. The single stages are marked with red numbers in Fig. 6.24.

In the first stage of the lab experimental setup, the transmitter's output is given. It is a BPSK modulated signal with an effective data rate of 6.25 Mb/s at a carrier frequency of 25 MHz. Hence, the signal bandwidth spans from 12.5 MHz to 37.5 MHz. The signal power level at the DAC's output is around -25 dBm. As discussed in Chapter 2, high level of signal attenuation and noise is present on the power lines of a vehicle. To overcome the lossy channel, the transmitted signal is amplified by approx. 20 dB in the second stage of the setup. The vehicle emulation stages 3 and 4 consist of attenuating the signal by ca. 40 dB and adding a white Gaussian noise source with a power level of roughly -60 dBm. In fact, the vehicle emulation stage should be placed in between the two balancer transformers as it is the case in an automotive scenario. However, in the lab setup both balancers were placed after the car emulation stage which makes no difference in terms of signal attenuation and noise addition, and does not affect the obtained results. To provide a high enough signal power to the receiver, another amplification is performed, again by approx. 20 dB, to reach a final signal power level of roughly -30 dBm. A final filtering by a low-pass filter with a sharp decline after the cutoff frequency of 45 MHz is performed in stage 7 and its output is fed into the receiver board. Each of the above described operations can be identified in the result figures Fig. A.2 - Fig. A.7 in Appendix A. The overall performance was evaluated by analyzing the received data. For this purpose, the receiver board sends the captured data packed in Ethernet packets to a computer. Since the payload data is known (cf. Section 6.2.5), it is possible to verify it by scanning it for bit failures.

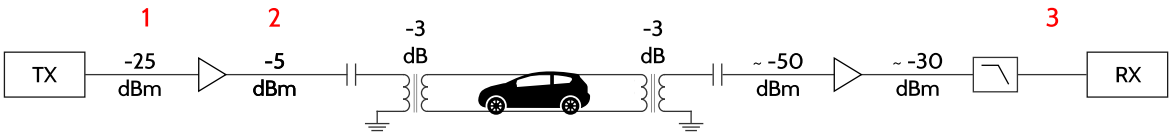

Figure 6.25.: Automotive power line transmission system experimental setup

There were 46 bytes in each frame detected with each byte containing incrementing values as it reaches the end of the frame. This matches with the generated data in the transmitter and an error-free transmission was achieved.

6.3.2. Automotive Environment

For the performance evaluation in an automotive environment a BMW X5 (F15) was used as a test vehicle. Predefined access points were identified and equipped throughout the car as shown in Fig. B.1 in Appendix B. It is important to note that, in order to isolate the DC voltage levels between the FPGA boards and the car, a single balancer (a transformer with a DC blocker) was attached to each vehicle access point. This is done to protect the amplifiers and the boards from voltage peaks by the vehicle power distributions. The evaluation of the system was performed at different access points and electric terminal states. Following seven access points RPD, FPD, 12V rear, LL, HEA, DDL and RDL (cf. Fig. B.1) were used in terminal states 30 (battery powered) and 15 (ignition powered). These were chosen based on their location in the car and the measurement results from Chapter 2. Throughout all measurements, the power line connecting the front and rear power distributions, RPD – FPD, featured high level of noise and attenuation. Hence, to better represent a worst case scenario, RPD was used as a transmitting access point with varying receivers – the remaining six access points.

The setup of the power line communication system deployed in the test vehicle is depicted in Fig. 6.25. First, again the BPSK modulated transmission signal at a carrier frequency of 25 MHz is given which is then amplified by approx. 20 dB. In the next stage the signal passes a balancer and is supplied into the test vehicle followed by another balancer and amplification of again approx. 20 dB. The outcoming signal is filtered by a low-pass filter which characteristics are described in Chapter 6.1.4. Upon capturing the data at the receiver, it is packed in Ethernet packets and sent to a computer for later offline processing.

The performance of the PLC demonstrator in an automotive environment was evaluated by analyzing the payload of the captured Ethernet packets for bit failures and

calculating the bit error rate (BER). In total $3.31 \cdot 10^6$ received bits were used for determining a BER of $1.4 \cdot 10^{-3}$. Using above described setup the signal power before passing the balancer and being supplied into the vehicle accounts for between -10 and -5 dBm (cf. Fig. A.2). Considering the 3 dB insertion loss of the balancer and a mean channel attenuation present on the car power lines of -40 dB, the power of the transmission signal approximates to -53 dBm. Assuming a mean noise power level of -60 dBm, which covers well with the observed measurements (see Sec. 3.2), would result in an estimated mean SNR present on an automotive PLC transmission channel of 7 dB. Even though noise power and channel attenuation measurements were performed at the same time while capturing data at the receiver, it is not possible to determine the exact range of values they cover at that same moment. Hence, only estimated mean values can be used for deriving an SNR approximation. Details on the noise power level and channel attenuation present on a car power line can be found in Chapter 2.2 and 3.1. To obtain reference BER values for the transmission scenario shown in Fig. 6.25, a simulation was developed to compute the BER of an in-vehicle PLC transmission system. The simulation considers all signal processing components of the demonstrator, though uses a matched filter, as well as the automotive transmission environment. However, the results are only a theoretical and close representation of the hardware implementation and hence to be treated as a rather lower bound. Fig. 6.26 illustrates a theoretical BER curve for an uncoded BPSK modulation scheme in an AWGN channel in red and the simulation results in blue. The lower data pin matches an SNR value of 7 dB and corresponds to a BER of $0.09796 \cdot 10^{-3}$. The BER obtained from the captured data by the demonstrator is marked on the same curve with an arrow and correlate with a simulated SNR of 5.5 dB. As expected, the performance of the implemented hardware demonstrator in a car environment is not as good as its simulated counterpart. Though, the above calculations on the SNR present on the in-vehicle PLC transmission channel are only a vage approximation by taking an estimated mean for the noise and channel attenuation. Further, a simulation provides a far more ideal transmission environment compared to a deployed hardware implementation.

Considering the setup in Fig. 6.25 the fastest and simplest way to improve the performance and hence, reduce the bit failures is to introduce an additional amplification stage before the car. This would increase the signal power being supplied into the vehicle with another 15 to 20 dB which results in a higher SNR and thus, a lower BER. In this scenario, in total $14.5 \cdot 10^7$ received bits were analyzed for determining the measured BER of $6.8736 \cdot 10^{-8}$ which corresponds to a single bit error in all used

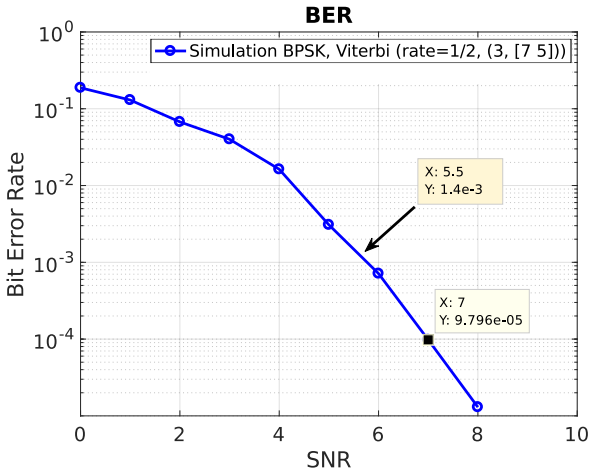

Figure 6.26.: BER simulation of the PLC demonstrator in an automotive environment

bits.

6.4. Summary

The in-vehicle PLC demonstrator described in this chapter was developed to prove the use of low complexity and low cost techniques to enable power line communication in an automotive environment given specific, restrictive requirements. The results both in a lab and a vehicle environment showed that a successful transmission can be established even in the presence of high noise and attenuation on the channel. The performance measurements in the vehicle were carried out between seven access points. One of them, RPD, was set as a transmitter while the remaining six were receivers. The access points were chosen such that a large share of the car is implied as well as power lines with different transmission characteristics. The transmitter and receiver units are implemented on a Xilinx Virtex-4 FPGA board equipped with an analog daughter board. The demonstrator uses BPSK modulation and convolutional encoding with a Viterbi decoder for a simple, fast and robust data processing. The use of low-noise amplifiers along with a sharp low-pass filter improves the reliability of the system. The demonstrator performance in an automotive environment was evaluated by analyzing the received data which is sent by the receiver board within Ethernet frames to a computer and calculating a BER. Tha data processing was done offline and yielded a BER of $1.4 \cdot 10^{-3}$ for an estimated SNR of 7 dB. In order to improve the system performance an additional amplification stage was introduced. As expected, the BER drops down and reaches a value of $6.8736 \cdot 10^{-8}$, which corresponds to a

single bit failure in $14.55 \cdot 10^7$ analyzed bits. The data transmission was carried out at a carrier frequency of 25 MHz and the provided data rate was 6.25 Mbit/s.

7

Conclusions

This thesis evaluates the applicability of PLC as an in-vehicle transmission technology. Thereby, it addresses several theoretical topics, as modeling the car power line network and the noise present on it, as well as a setup of an experimental demonstrator.

Chapter 2 presents some of the efforts done on characterizing the transmission properties of an automotive PLC channel. The introduced channel model, based on the two-port network theory, allows for a systematic and component-wise assembling, and analysis of the channel. Results of extensive measurements in a test vehicle are provided and used for comparison and investigation of the car power line network. It is observed, that different transmission paths in the car power line network vary strongly in their transmission quality. Especially, paths including any of the power distributions (FPD, BPD and RPD) experience a very poor transmission quality due to high attenuation on the channels, introduced by the power distributions. By a detailed analysis of the main components of a car power line network, it can be concluded, that car power lines themselves have only a negligible impact on the overall PLC channel transmission characteristics. One of the main outcomes of this work, is that the load impedances introduced by the internal termination of the ECUs are strongly impacting the channel characteristic. Further, an extensive study on the impact of the wiring dimension and load impedance on the PLC channel characteristics was performed. Thereby, three different load impedances were examined. It can be summarized, that while a pure resistive termination introduces additional overall attenuation, it allows for a smoother transmission loss over the observed frequency range of 0 - 600 MHz and hence, less frequency selective behavior of the channel.

In the following chapter, measurements, analysis and modeling of the noise present on an automotive PLC transmission channel are discussed. The results obtained from comprehensive noise captures, performed in a test vehicle, were systematically analyzed. It is shown that the noise has a non-Gaussian nature and is highly impulsive and partly bursty. A notable observation is, that by evaluating the power spectrum of the captured noise sequences, three obvious peak clusters, at the frequencies 33 MHz, 25 MHz and 16.7 MHz, can be clearly distinguished. Further analysis allows to conclude that the power peaks experienced at 33 MHz are most likely to be caused by impulses. Whereas the peaks at 25 and 16.7 MHz, are with high probability originated by the background noise. Within the measurements, impulses with amplitude with up to 1.3 V were experiences on the power lines. However, already 90% of the impulses keep an amplitude below 96 mV.

Based on the measurement results and their evaluation, this work proposes a new classification of the non-Gaussian noise present on an automotive PLC channel. Four classes of background, periodic, random and predictable impulsive noise are suggested. The Gaussian background noise is determined with a maximum peak amplitude of 309.4 mV. However, the 90th percentile is at already 123.8 mV and the 50th, at 22 mV. Pulses, classified as periodic noise, have rather short duration and IAT compared to non-periodic pulses. Their amplitude spans within the complete measured range. Random impulsive noise is as its name says, randomly occurring in time, the time of arrival is unpredictable as well as the amplitude. In contrast, predictable impulsive noise pulses have a much longer duration and predictable start and end points in time. Predictable impulsive noise has a complex structure, compound by multiple pulses and bursts. The knowledge of its pattern and frequency of occurrence may be used to optimize an in-vehicle PLC system performance. Chapter 3 is finalized by introducing several statistical models for modeling noise of impulsive, non-Gaussian nature. Thereby, a new noise model, the Poisson-Gaussian Burst Model, is proposed to better represent the noise characteristics, observed on an automotive power line network. The model enables the adjustment of the key noise characteristics, such as number of impulses occurring per unit time, impulse amplitude distribution as well as the impulse duration.

Chapter 5 compares the system performance in terms of bit error rate (BER) over the signal to noise (SNR) ration for different modulation formants and error mitigation methods. It compares the results for three simulation setups which build upon one another. In the first scenario, convolutional codes with rate 1/2 and 2/3 are evaluated. Although, a convolutional code has a relatively good correcting property, it does not

perform well in the presence of burst errors. This behavior is also reflected by the presented results. In single cases, as e.g. for 8-PSK and 16-PSK, the 1/2 rate code does give a slight improvement though. A more notable correction is shown with the rate 1/2 code for high SNR values and almost all modulation schemes. A standalone use of a rate 2/3 convolutional code is not beneficial unless used for high SNR above 18-20 dB. In contrast to the moderate results obtained with convolutional coding, by introducing an interleaver to the system, the BER results can be notably improved. Even with the rate 2/3 code, it gives very satisfying results and an SNR gain of up to 9 dB can be observed. It is worth mentioning that, the interleaved results for all data rates are surprisingly similar. That is, higher transmission rates can be achieved with comparably low error rate. In the last third simulation setup, a concatenated coding is used in which an outer 3/4 rate Reed-Solomon code and an inner 2/3 convolutional code are placed before the interleaver. Comparing all results, it can be concluded that this more complex system setup is reasonable only for high SNR values above approx. 11 dB and data rates up to 10 Mbps. In all other scenarios, a straightforward high rate convolutional code with interleaver provides already better results.

Finally, this thesis is completed by presenting an FPGA-based implementation of an automotive PLC transmission system. The described demonstrator was developed to prove the use of low complexity and low cost techniques to enable PLC in an automotive environment given specific, restrictive requirements. The demonstrator was tested in a lab and a vehicle environment. The data transmission was carried out at a carrier frequency of 25 MHz. The provided data rate was 6.25 Mbps which already beyond the supported data rate by CAN. The results showed, that a successful transmission can be established in both environments even in the presence of high noise and attenuation on the channel. The demonstrator uses BPSK modulation and convolutional encoding with a Viterbi decoder for a simple, fast and robust data processing. The use of low-noise amplifiers along with a sharp low-pass filter improves the reliability of the system. The performance of the FPGA-based system in the car environment was evaluated by calculating the BER. The first obtained results are for a setup with a single amplification stage at the transmitter and receiver side with each approx. 20 dB. A calculation of the BER for this scenario yielded $1.4 \cdot 10^{-3}$ for an estimated SNR of 7 dB. By introducing an additional amplification stage, the BER could be reduced to $6.8736 \cdot 10^{-8}$, which corresponds to a single bit failure in $14.55 \cdot 10^{7}$ analyzed bits. By applying the insights from Ch. 5, the performance can significantly improved for even much higher data rates.

Certainly, there are many open issues, which could be a subject to future work.

By improving the impulse recognition algorithm, the complex structure of predictable impulsive noise could be better caught. In general, by improving the algorithm by an adaptive moving window, the recognition could be done faster, since no manual adaptation in extreme scenarios needs to be done. Further, when having a better database on the characteristics of predictable impulsive noise, the data could be used to improve the system performance. By knowing the structure, duration and amplitude development in time of a predictable impulse, transmission techniques capable of handling this type of noise could be targeted. In the same context, a more extended study could be done on noise mitigation methods. A Wiener filter is known to perform well in compensating non-Gaussian noise. Also, the application of coded modulation would be an interesting investigation. Herewith, low complexity modulation schemes could be combined with more sophisticated coding methods for better overall performance. Also, an interesting investigation could be done on applying larger Reed-Solomon codes. This could improve the performance of the concatenated coding scenario. Another topic worth mentioning is, evaluating the effect of an additional interleaver stage between the Reed-Solomon Code and the convolutional code. This could lead to improvement especially when longer RS-codes are used. Further, it would be interesting to investigate on the data transmission limits supported by simple convolutional coding with interleaving. Alternatively, the upper boundary on the convolutional code rate could be evaluated.

A

Measurements

Measurements of signal spectrum and waveform in a lab environment at the debugging points depicted in Fig. 6.24.

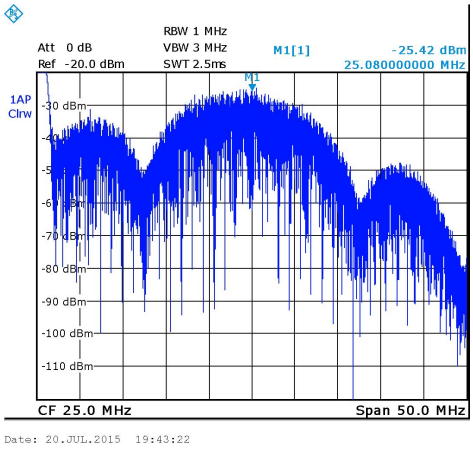

Figure A.1.: Signal spectrum at point 1 in Fig.6.24

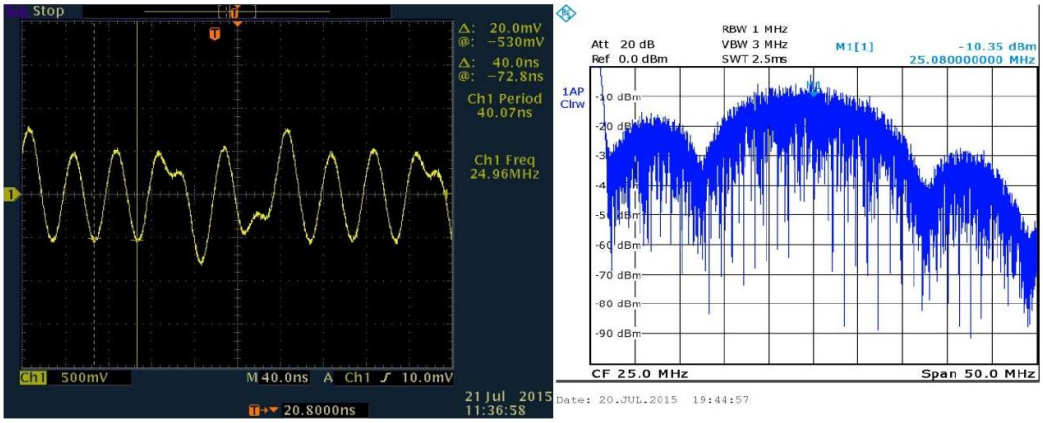

Figure A.2.: Signal spectrum and waveform at point 2 in Fig.6.24

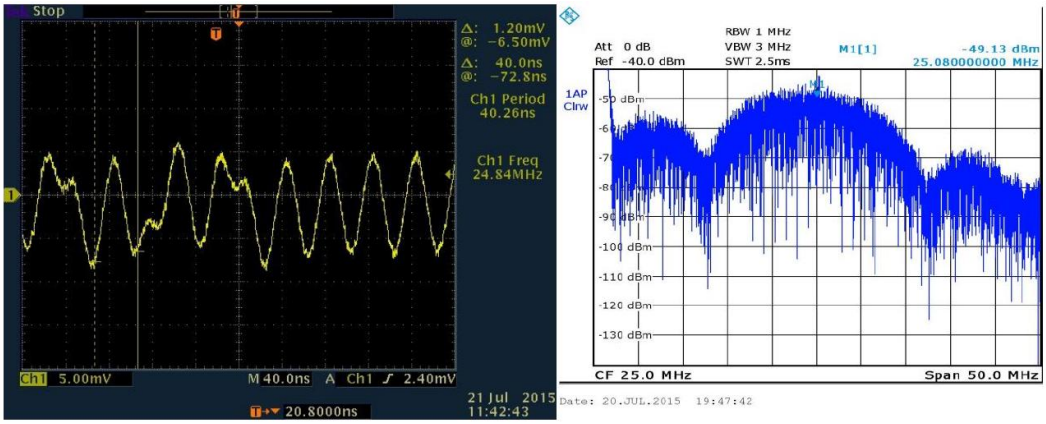

Figure A.3.: Signal spectrum and waveform at point 3 in Fig.6.24

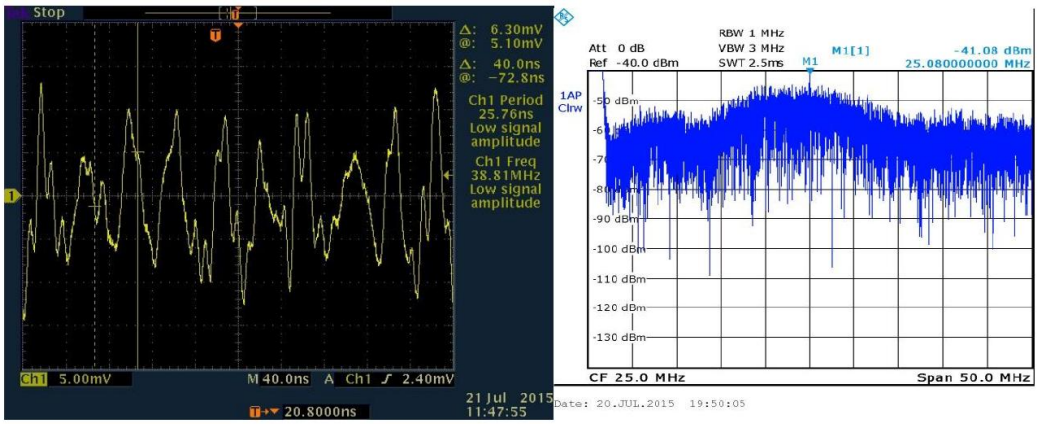

Figure A.4.: Signal spectrum and waveform at point 4 in Fig.6.24

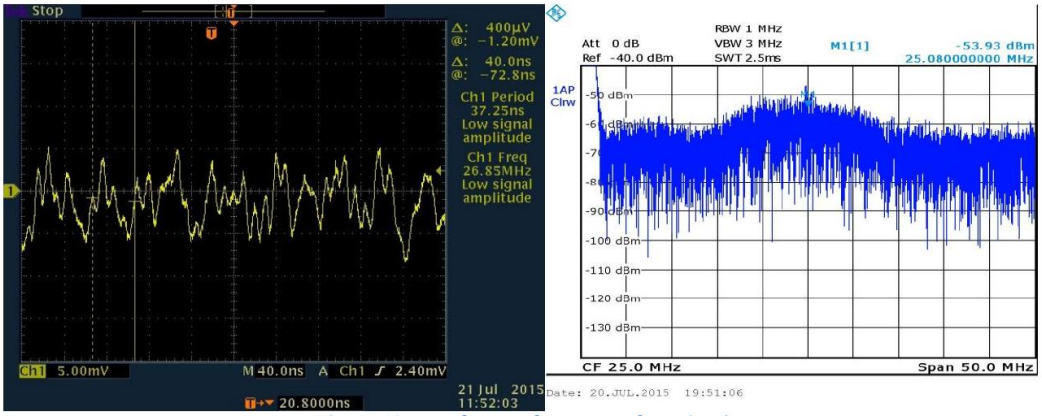

Figure A.5.: Signal spectrum and waveform at point 5 in Fig.6.24

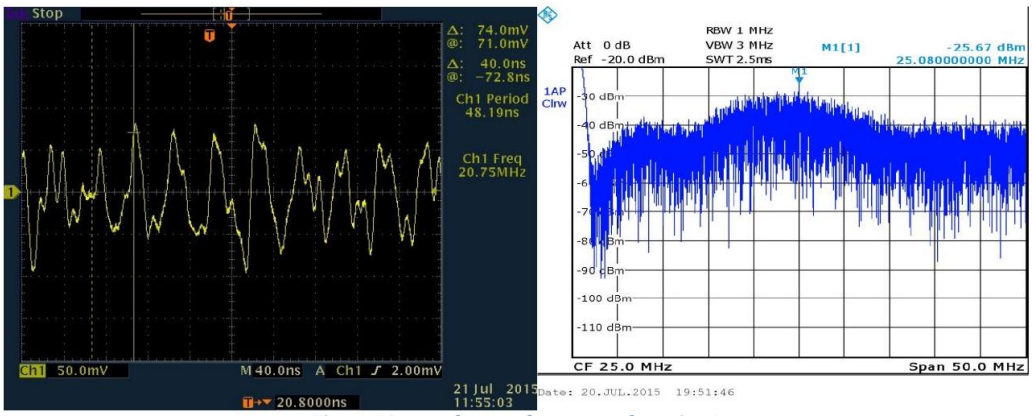

Figure A.6.: Signal spectrum and waveform at point 6 in Fig.6.24

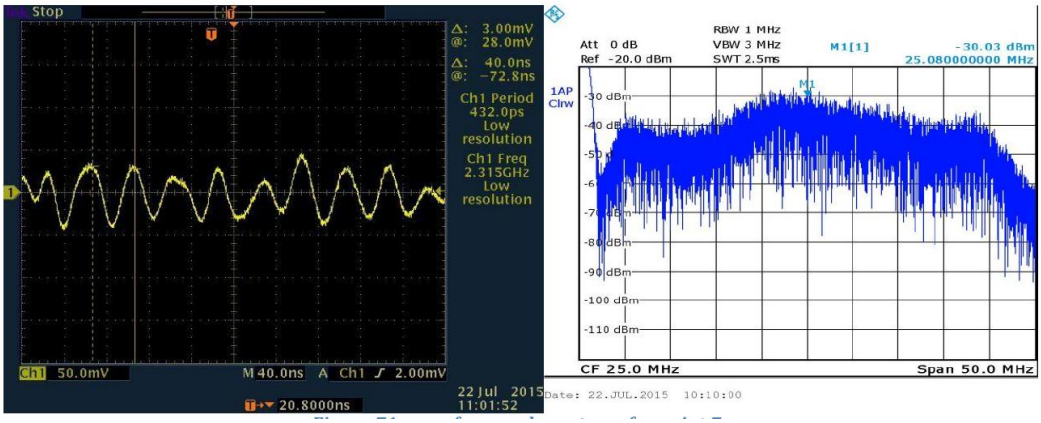

Figure A.7.: Signal spectrum and waveform at point 7 in Fig.6.24

B

Test Vehicle

Fig. B.1 shows all access points in the test vehicle used for performing channel and noise measurements. The results are presented and discussed in Chapter 2 and 3. The abbreviations are given as follwos

- 12V rear - 12 Volt supply at the rear seats
- BPD - Battery Power Distribution
- CDDL - Co-Driver Door Long line
- C-Pillar - Car' C-Pillar
- DDL - Driver Door Long line
- DDS - Driver Door Short line
- FPD - Front Power Distribution
- HEA - High End Audio
- LL - Left Light
- RCU - Roof Control Unit
- RDL - Rear Door Long line
- RPD - Rear Power Distribution
- SCA - Soft-Close Automatic

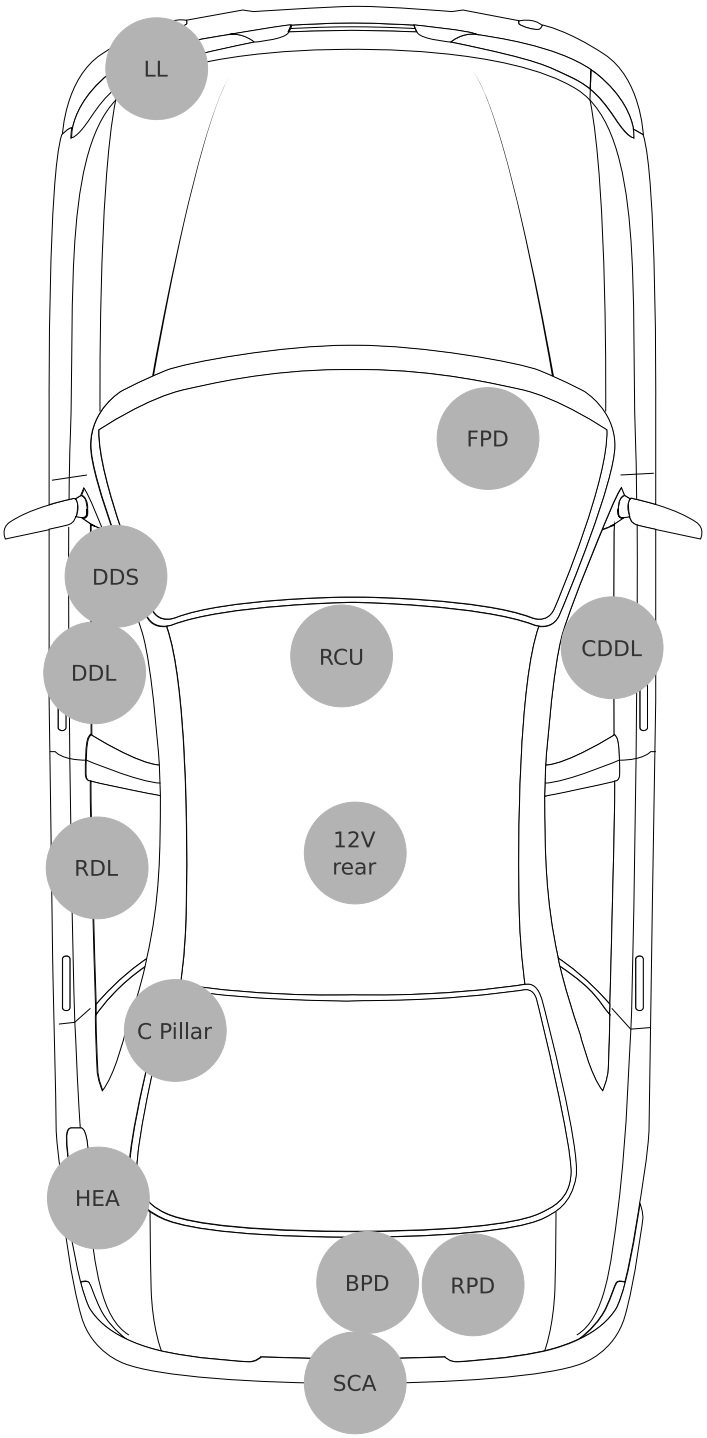

Figure B.1.: Test vehicle with all available access points

C

Pulse Recognition Algorithm

The source data, used as input of the algorithm, is the raw data delivered by the LeCroy waverunner 6100A 1 GHz oscilloscope. In this Appendix, a description of the algorithm is given in a mixed form of pseudocode and textual explanation.

Require: Let *data* be a vector holding the sample values recorded by the oscilloscope.

Step 1

1. `data = abs(data);`.
2. Calculate the root mean square (RMS) envelope of *data* and apply a sliding window of size $slid_{wdw}$,

   `env_up = rms_envelope(data, slid_wdw);`.

Step 2

1. Determine the amplitude range

   `amp_range = max(env_up) - min(env_up)`.

2. For a predefined number of histogram bins, depending on the total number of samples of env_{up}, determine

   `bin_width = amp_range / num_bins`.

3. Sort data into the histogram bins.
4. Identify the lowest-indexed histogram bin, i_{low}, and highest-indexed histogram bin, i_{high}, with nonzero counts.

5. Divide the histogram such that:

   The indices of the lower histogram bins are $i_{low} <= i <= 1/2(i_{high}{}^{-}i_{low})$.

   The indices of the upper histogram bins are $i_{low}+1/2(i_{high}{}^{\smile}i_{low}) <= i <= i_{high}$.

6. Get the low state S_l and high state S_h by computing the mode or mean of the lower and upper histograms.

7. **return** `histog, bin_centers, S_l, S_h`.

Step 3

1. It is assumed that pulses occur rather seldom compared to background noise. More precisely, it is assumed that, in general, in 90% of the time only a background noise is present on the channel. Hence,

   ```
   gaussian_share = 0.9*total_samples(env_up);
   ```

2. Withing the histogram, find bin_i, such that $\sum_{j=1}^{i} cnt_j > gaussian\_share$, where cnt_j is the counts in bin_j.

3. Set an impulse threshold

   `amp_thres = bin_center(i) * pulse_thres`,

   where $pulse_{thres}$ is a predefined threshold value. For instance, for $pulse_{thres} = 1.3$ it is assumed, that whenever the signal (env_{up}) reaches amplitudes up to 30% above the amplitude of 90% of the signal's samples, it can be handled by the transmission system and it is not regarded as an impulse. Amplitudes above this threshold are treated as an impulse.

4. Set the threshold for measuring the pulse duration

   ```
   noise_total_amp = S_h - S_l;
   ```

   ```
   S_h = amp_thres;
   ```

5. Set a mid-reference measurement level mid_{ref} for the pulses. Since pulses build up in time, set mid_{ref} as close as possible to S_l, but not too close to avoid wrong decision due to slight fluctuations.

   ```
   mid_ref = S_l + 0.05*(S_h - S_l)
   ```

6. Measure the time differences between the mid-reference level instants of the initial and final transitions of each pulse.

Bibliography

[1] T. Esmailian, F. R. Kschischang, and P. G. Gulak, "An In-building Power Line Channel Simulator," *Intl. Simposium ISPLC'04*, pp. 31–35, Mar. 2002.

[2] S. Khan, A. F. Salami, W. A. Lawal, A. H. M. Zahirul Alam, A. S. Hameed, and M. J. E. Salami, "Characterization of Indoor Power Line as Data Communication Channels Experimental Details and Results," *Intl. Journal of Electrical and Computer Engineering*, vol. 4, pp. 647–651, 2009.

[3] S. Galli, "A simplified model for the indoor power line channel ," *IEEE Intl. Symposium on Power Line Communications and Its Applications, ISPLC'09*, pp. 13–19, 2009.

[4] T. Berger and G. Moreno-Rodríguez, "Power Line Communication Channel Modelling through Concatenated IIR-Filter Elements," *Journal of Communications*, vol. 4, pp. 41–51, 2009.

[5] G. Leen and D. Heffernan, "Expanding automotive electronic systems," *IEEE Computer*, pp. 88–93, Jan. 2002.

[6] F. Nouvel, G. Zein, and J. Citerne, "Code division multiple access for an automotive area network over power-lines," *IEEE 44th Vehicular Technology Conference, VTC'94*, vol. 1, pp. 525–529, 1994.

[7] H. Beikirch and M. Voss, "Can-transceiver for field bus power-line communications," *IEEE ISPLC'00*, pp. 257–264, 2000.

[8] A. Schiffer, "Statistical channel and noise modeling of vehicular dc-lines for data communication," *IEEE 44th Vehicular Technology Conference, VTC'00*, vol. 1, pp. 158–162, 2000.

[9] M. Lienard, M. Carrion, V. Degardin, and P. Degauque, "Modeling and analysis of in-vehicle power line communication channels," *IEEE Trans. on Vehicular Technology*, vol. 57, pp. 670–679, 2008.

[10] M. Mohammadi, L. Lampe, M. Lok, S. Mirabbasi, M. Mirvakili, R. Rosales, and P. van Veen, "Measurement study and transmission for in-vehicle power line communication," *IEEE ISPLC'09*, pp. 73–78, Mar 2009.

[11] P. Tanguy and F. Nouvel, "In-vehicle plc simulator based on channel measurements," *Int. Conf. On Intelligent Transport System Telecommunicatinos, ITST*, 2010.

[12] V. Degardin, M. Carrion, M. Lienard, and P. Degauque, "In-vehicle powerline communication: Impulsive noise characteristics," 2005.

[13] V. Degardin, M. Lienard, and P. Degauque, "Impulsive noise characterization of in-vehicle power line," *IEEE Transactions on Electromagnetic Compatibility*, vol. 50, no. 4, pp. 861–868, November 2008.

[14] Y. Yabuuchi, D. Umehara, M. Morikura, T. Hisada, S. Ishiko, and S. Horihata, "Measurement and analysis of impulsive noise on in-vehicle power lines," *IEEE International Symposium on Power Line Communications and Its Applications*, 2010.

[15] A. Pittolo, M. D. Piante, F. Versolatto, and A. M. Tonello, "In-vehicle plc: in-car and in-ship channel characterization," *IEEE Vehicular Technology Magazine*, 2015.

[16] G. A. Lodi, A. Ott, S. Cheema, M. Haardt, and T. Freitag, "Power line communication in automotive harness on the example of local interconnect network," *International Symposium on Power Line Communications and its Applicability (ISPLC)*, pp. 212–217, 2016.

[17] H. Zhang, L. Yang, and L. Hanzo, "Ldpc-coded index-modulation aided ofdm for in-vehicle power line communications," *Vehicular Technology Conference (VTC Spring)*, 2016.

[18] Y. Kobayashi, Y. Furuta, and S. Cha, "A wide-range frequency offset tolerant ofdm for in-vehicle plc system," *International Symposium on Power Line Communications and its Applications (ISPLC)*, 2017.

[19] E. Oberleithner and N. Hanik, "Impact of system components on an automotive plc channel," *IEEE 80th Vehicular Technology Conference (VTC2014-Fall)*, pp. 1–5, Sept 2014.

[20] G. Ulbricht, *Netzwerkanalyse, Netzwerksynthese und Leitungstheorie*. Teubner Studienskripten, 1986.

[21] M. Steer, *Microwave & RF Design: A Systems Approach*, D. R. Kay, Ed. Scitech Publishing, 2010.

[22] D. A. Frickey, "Conversions between s, z, y, h, abcd, and t parameters which are valid for complex source and load impedances," in *IEEE Transactions on Microwave Theory and Techniques*, ser. 2, vol. 42, Feb 1994, pp. 205–211.

[23] P. C. Magnusson, A. Weisshaar, V. K. Tripathi, and G. C. Alexander, *Transmission Lines and Wave Propagation*. CRC Press, 1991.

[24] M. Grigoriu, "Simulation of stationary non-gaussian translation processes," *Journal of Engineering Mechanics*, vol. 124, no. 2, pp. 121–127, 1998.

[25] L. Lampe, "Database of in-vehicle plc channel measurements," 2008. [Online]. Available: http://ivplc.ece.ubc.ca/index.php/measurements

[26] E. Surewaard, E. Karden, , and M. Tiller, "Advanced electric storage system modeling in modelica," *Proc. of 3rd Intl. Modelica Conference*, p. 95–102, Nov 2003.

[27] F. Kremer and S. Frei, "Simulation of emissions of power electronic devices in electrical and hybrid electrical vehicles," *Asia-Pacific Symposium on Electromagnetic Compatibility, APEMC'10*, pp. 691–694, 2010.

[28] F. Andre, D. Winkler, and C. Guehmann, "Modellierung einer li-ionen batterie fuer hybridfahrzeug-simulationen," Master's thesis, TU Berlin, 2008.

[29] R. Jahn, D. Lemmens, W. Foubert, and S. Uytterhoeven, "Plc noise and impedance measurements on loads and in the distribution grid," *International Conference and Exhibition on Electricity Distribution*, 2013.

[30] P. Lopes, "Plc noise measurements," May 2010. [Online]. Available: http://sips.inesc-id.pt/~pacl/PLCNoise/index.html

[31] T. H. Tran, D. D. Do, and T. H. Huynh, "Plc impulsive noise in industrial zone: Measurement and characterization," *International Journal of Computer and Electrical Engineering*, vol. 5, no. 1, pp. 48–51, 2013.

[32] R. Hashmat, "Characterization and modeling of the channel and noise for indoor mimo plc networks," PhD Thesis, Université de Rennes 1, 2012.

[33] D. Sabolić and V. Varda, "Indoor distribution network noise in the plc frequency range, from 10 mhz to 30 mhz," *International Conference on Power and Energy Systems*, pp. 249–254, 2004.

[34] G. Avril, M. Tlich, F. Moulin, A. Zeddam, and F. Nouvel, "Time/frequency analysis of impulsive noise on powerline channels," *International Federation for Information Processing Digital Library; Home Networking*, 2008.

[35] H. C. N. Gauthier, A. Zeddam, M. Tlich, and M. Machmoum, "Time domain modeling of powerline impulsive noise at its source," *Journal of Electromagnetic Analysis and Applications*, vol. 3, pp. 359–367, 2011.

[36] S. V. Vaseghi, *Advanced digital signal processing and noise reduction*, 2nd ed. John Wiley & Sons, 2000.

[37] D. Middleton, "Statistical-physical models of urban radio-noise environments part i: Foundations," *IEEE Transactions on Electromagnetic Compatibility*, vol. 14, no. 2, pp. 38–56, 1972.

[38] ——, "Statistical-physical models of electromagnetic interference," *IEEE Transactions on Electromagnetic Compatibility*, vol. 19, no. 3, pp. 106–127, 1977.

[39] ——, "Canonical non-gaussian noise models: Their implication for measurements and for prediction of receiver performance," *IEEE Transactions on Electromagnetic Compatibility*, vol. 21, no. 3, pp. 209–220, 1979.

[40] L. A. Berry, "Understanding middleton's canonical formula for class a noise," *IEEE Transactions on Electromagnetic Compatibility*, vol. 23, no. 4, pp. 337–344, 1981.

[41] K. Vastola, "Threshold detection in narrow-band nongaussian noise," *IEEE Transactions on Communications*, vol. 32, no. 2, pp. 134–139, 1984.

[42] S. Miyamoto, M. Katayama, and N. Morinaga, "Performance analysis of qam systems under class a impulsive noise environment," *IEEE Transactions on Electromagnetic Compatibility*, vol. 37, no. 2, pp. 260–267, 1995.

[43] J. Häring and A. J. H. Vinck, "Performance bounds for optimum and suboptimum reception under class-a impulsive noise," *IEEE Transactions on Communications*, vol. 50, no. 7, pp. 1130–1136, 2002.

[44] ——, "Iterative decoding of codes over complex numbers for impulsive noise channels," *IEEE Transactions on Information Theory*, vol. 49, no. 5, pp. 1251–1260, 2003.

[45] K. C. Wiklundh, P. F. Stenumgaard, and H. M. Tullberg, "Channel capacity of middleton's class a interference channel," *Electronics letters*, vol. 45, no. 24, pp. 1227–1229, 2009.

[46] G. Ndo, F. Labeau, and M. Kassouf, "A markov-middleton model for bursty impulsive noise: Modeling and receiver design," *IEEE Transactions on Power Delivery*, vol. 28, no. 4, pp. 2317–2325, 2013.

[47] D. Middleton, "Canonical and quasi-canonical probability models of class a interference," *IEEE Transactions on Electromagnetic Compatibility*, vol. 25, no. 2, pp. 76–106, 1983.

[48] A. B. Shahzad, "Impulsive noise modeling and prediction of its impact on the performance of wlan receiver," 2009, glasgow, Scotland.

[49] J. G. Proakis, *Digital Communications*, 2nd ed. McGraw-Hill Book Company, 1989.

[50] P. P. Vaidyanathan, S.-M. Phoong, and Y.-P. Lin, *Signal Processing and Optimization for Transceiver Systems*. Vaidyanathan, 2010.

[51] I. HomePlug Powerline Alliance, "Homeplug™ av2 technology," 2013, http://www.homeplug.org/media/filer_public/2c/32/2c327fc8-25bb-409e-abf7-c398534c24dc/homeplug_av2_whitepaper_130909.pdf.

[52] ——, "Homeplug green phy™ 1.1," 2012, http://www.homeplug.org/media/filer_public/92/3f/923f0eb3-3d17-4b10-ac75-03c3c2855879/homeplug_green_phy_whitepaper_121003.pdf.

[53] M. Mohammadi, L. Lampe, M. Lok, S. Mirabbasi, M. Mirvakili, R. Rosales, and P. van Veen, "Measurement study and transmission for in-vehicle power line communication," *International Symposium on Power Line Communications and its Applicability (ISPLC)*, pp. 73–78, 2009.

[54] A. B. Vallejo-Mora, J. J. Sánchez-Martínez, F. J. Cañete, J. A. Cortés, and L. Díez, "Characterization and evaluation of in-vehicle power line channels," *IEEE Global Telecommunications Conference*, 2010.

[55] *IEEE Standard for Local and Metropolitan Area Networks, IEEE Std. 802.16e-2005*, Std.

[56] *Virtex-4 MB Development Board User's Guide*, 3rd ed., Memec, December 2005.

[57] *P240 Analog Module User Guide*, 1st ed., Avnet Electronics, 2005.

[58] *16-Bit, 500Msps 2x-8x Interpolating Dual-Channel Digital-to-Analog Converter (DAC)*, Texas Instruments, September 2006. [Online]. Available: www.ti.com

[59] *14-Bit, 125Msps Analog-to-Digital Converter*, Texas Instruments, February 2007. [Online]. Available: www.ti.com

[60] *10/100BASE-TX/FX Mini Transceiver*, Broadcom, February 2002.

[61] *LogiCore IP Tri-Mode Ethernet MAC*, v4.4 ed. ed., Xilinx, April 2010.